January 2015

The Determination of the Half-Life of Si-32 and Time Varying Nuclear Decay

Jordan Heim
Purdue University

Graduate School Form 30
Updated 1/15/2015

PURDUE UNIVERSITY
GRADUATE SCHOOL
Thesis/Dissertation Acceptance

This is to certify that the thesis/dissertation prepared

By Jordan M. Heim

Entitled

THE DETERMINATION OF THE HALF-LIFE OF Si-32 AND TIME VARYING NUCLEAR DECAY

For the degree of Doctor of Philosophy

Is approved by the final examining committee:

Ephraim Fischbach
Chair

Andrew S. Hirsch

Mark Haugan

Fuqiang Wang

To the best of my knowledge and as understood by the student in the Thesis/Dissertation Agreement, Publication Delay, and Certification Disclaimer (Graduate School Form 32), this thesis/dissertation adheres to the provisions of Purdue University's "Policy of Integrity in Research" and the use of copyright material.

Approved by Major Professor(s): Ephraim Fischbach

Approved by: Ken Ritchie 11/23/2015

Head of the Departmental Graduate Program Date

THE DETERMINATION OF THE HALF-LIFE OF ^{32}SI AND TIME VARYING NUCLEAR DECAY

A Dissertation

Submitted to the Faculty

of

Purdue University

by

Jordan M. Heim

In Partial Fulfillment of the

Requirements for the Degree

of

Doctor of Philosophy

December 2015

Purdue University

West Lafayette, Indiana

This work is dedicated to my parents for their endless support.

ACKNOWLEDGMENTS

I would like to thank my advisor, Ephraim Fischbach, for his continued support over the years; he has provided both academic and personal mentorship that far exceed an advisor's responsibilities. I would also like to thank Virgil Barnes for his considerable involvement with my experimental work at Purdue. In addition, I want to express gratitude to my committee members, Andy Hirsch, Mark Haugan, and Fuqiang Wang, not only for their support in completing my thesis, but also for their help throughout my academic career at Purdue. I would also like to acknowledge Dylan Neff for his work in developing and implementing software critical to my analysis. Lastly, I thank Sandy Formica, Carol Buuck, and the other staff members in the physics department for their continual aid.

I wish to express deep appreciation to Jonathan Nistor and Tasneem Mohsinally, close friends and colleagues, who have contributed enormously to my achievements and have greatly shaped my experience at Purdue, and to my family for the vast support they have given me over the years.

TABLE OF CONTENTS

Page

LIST OF TABLES

Table Page

LIST OF FIGURES

Figure Page

ABSTRACT

Heim, Jordan M. Ph.D., Purdue University, December 2015. The Determination of the Half-Life of ^{32}Si and Time Varying Nuclear Decay. Major Professor: Ephraim Fischbach.

The aim of this work is to make an accurate determination of the half-life of ^{32}Si as well as to investigate reported variations in nuclear decay rates. Primarily, we focus on a previous experiment at Brookhaven National Lab (BNL) [1], which measured the ratio of interwoven ^{32}Si and ^{36}Cl decays over a 4 yr period and reported unexplained annual periodicities. Utilizing the very same sources and shuffling apparatus, we have observed the decay of ^{32}Si and ^{36}Cl for more than 6,000 hours each, over the last ~ 2 yr, while recording $\sim 5 \times 10^6$ individual environmental readings. The half-life of ^{32}Si, which has been quoted between 101(18) yr and 330(40) yr, is redetermined by this data to be 159.4 yr $\pm$ 1.9 yr (statistical) $\pm$ 3.7 yr (systematic) with $\chi^2_{DOF} = 1.01$. We have also observed a periodic signal in the ^{32}Si/^{36}Cl ratio decay data, similar to that in the original experiment at BNL, which we analyze at length. Finally, a related topic concerning self-induced decay and its relationship to systematic dead-time corrections is presented.

1. Introduction

The behavior of radioactive isotopes is generally thought to be well-understood, and the practice of determining half-lives is seemingly straightforward. Yet many reported values are discrepant far beyond the collective uncertainties. Half-life determinations of ^{32}Si, studied in this work, have ranged from ∼100 yr to more than 300 yr. Further, a number of nuclear decay experiments have observed persistent and unexplained temporal features in the data. Across a multitude of geographical locations, experimental designs, implemented technologies, and isotopes studied, one commonality appears to be small periodic modulations in the observed decay rates (see Table 1.1). The frequencies reported suggest a possible connection to the Sun, which is further bolstered by evidence of a positive relationship between solar indices data and anomalous behavior of nuclear decay [24].

Irrespective of the source of these anomalies, they deserve to be resolved; implications to the field of metrology notwithstanding, the importance of nuclear decay across a multitude of scientific and medical applications merits further study. In the following chapters, we discuss our work in attempting to address the issue by constructing an experiment designed to redetermine the half-life of ^{32}Si, while recording a large set of environmental and systematic data with which any potential decay rate modulation can be compared. We also discuss a related topic concerning self-induced decay and its relationship to rate-related losses and systematic dead-time corrections. In order to provide additional perspective, an overview of relevant historical events is provided in the next chapter, which will follow the events as presented in [25], [26], and [27].

Isotope	Decay Type	Detector Type	Radiation Measured	Effect/Periodicity Observed	Reference
^{3}H	β^-	Photodiodes	β^-	1 yr^{-1}	[2]
^{3}H	β^-	Liquid Scintillator	β^-	1 d^{-1}, 12.1 yr^{-1}, 1 yr^{-1}	[3]
^{3}H	β^-	Liquid Scintillator	β^-	$\sim$ 12.5 yr^{-1}	[4]
^{3}H	β^-	Solid State (Si)	β^-	$\sim$ 2 yr^{-1}	[5]
^{22}Na/^{44}Ti	β^+, κ	Solid State (Ge)	γ	1 yr^{-1}	[6]
^{36}Cl	β^-	Proportional	β^-	1 yr^{-1}, 11.7 yr^{-1}, 2.1 yr^{-1}	[7,8,9]
^{36}Cl	β^-	Geiger–Müller	β^-	1 yr^{-1}	[10]
^{54}Mn	κ	Scintillation	γ	Solar flare	[11]
^{54}Mn	κ	Scintillation	γ	1 yr^{-1}	[12]
^{54}Mn	β^-	Scintillation	γ	1 yr^{-1}	[13]
^{60}Co	β^-	Geiger–Müller	β^-, γ	1 yr^{-1}	[14,15]
^{60}Co	β^-	Scintillation	γ	1 d^{-1}, 12.1 yr^{-1}	[16]
^{85}Kr	β^-	Ion Chamber	γ	1 yr^{-1}	[17]
^{90}Sr/^{90}Y	β^-	Geiger–Müller	β^-	1 yr^{-1}, 11.7 yr^{-1}	[14,15,18]
^{108m}Ag	κ	Ion Chamber	γ	1 yr^{-1}	[17]
^{133}Ba	β^-	Ion Chamber	γ	1 yr^{-1}	[19]
^{137}Cs	β^-	Scintillation	γ	1 d^{-1}, 12.1 yr^{-1}	[16]
^{152}Eu	β^-, κ	Solid State (Ge)	γ	1 yr^{-1}	[20]
^{152}Eu	β^-, κ	Ion Chamber	γ	1 yr^{-1}	[17]
^{154}Eu	β^-, κ	Ion Chamber	γ	1 yr^{-1}	[17]
^{222}Rn	α, β^-	Scintillation	γ	1 yr^{-1}, 11.7 yr^{-1}, 2.1 yr^{-1}	[21,22]
^{226}Ra	α, β^-	Ion Chamber	γ	1 yr^{-1}, 11.7 yr^{-1}, 2.1 yr^{-1}	[7,23,9]
^{239}Pu	β^-	Solid State	α	1 d^{-1}, 13.5 yr^{-1}, 1 yr^{-1}	[3]

Table 1.1

Various experiments in which time-dependent nuclear decay rates have been observed [6]. For each entry the observed nuclides and their dominant decay modes are exhibited. Observed periodicities in the decay rates are noted.

2. Historical Considerations

2.1 X-rays

The history of radioactivity begins with Roentgen's 1895 discovery of what would become known as x-rays, since further investigation into this new phenomenon quickly led to the discovery of radioactivity, itself. Roentgen was in the midst of repeating an experiment on cathode rays (electrons) originally carried out by Heinrich Hertz and his student Phillipp Lenard. While recreating a specific experimental design of Lenard's, Roentgen found "...if one covers the [cathode ray] tube with a fairly close-fitting mantle of thin black cardboard, one observes in the completely darkened room that a paper screen painted with barium platinocyanide placed near the apparatus glows brightly or becomes fluorescent with each discharge, regardless of whether the coated surface or the other side is turned toward the discharge tube. This fluorescence is still visible at a distance of two meters from the apparatus" [25]. Roentgen was reportedly so astounded by his findings that he had to convince himself repeatedly of what he observed. Indeed, he mentioned to his wife only that he was working on something which would make people say he had probably gone crazy. After publishing his results complete with several x-ray images (including the now famous image of his wife's hand) on Jan 1, 1896, the news quickly traversed the western world. The scientific community was electrified; shortly after, it was said by a young Ernest Rutherford that "...the great object is to find the theory of matter before anyone else, for nearly every professor in Europe is now on the warpath" [25].

2.2 Uranic Rays

The aforementioned connection between x-rays and radioactivity lies with Henri Becquerel. It was briefly believed that these x-rays might be connected with phosphorescence, so Becquerel's study of uranic salts was a natural progression. His method of experimentation was thus described in his own words: "One wraps a photographic plate...in two sheets of very thick black paper...so that the plate does not fog during a day's exposure to sunlight. A plate of the phosphorescent substance is laid above the paper on the outside and the whole is exposed to the sun for several hours [to excite the phosphorescent substance]. When the photographic plate is subsequently developed, one observes the silhouette of the phosphorescent substance, appearing in black on the negative. If a coin or a sheet of metal...is placed between the phosphorescent material and the paper, then the image of these objects can be seen to appear on the negative" [25]. It is understandable, then, that these phosphorescent phenomena were thought to be producing x-rays. A week later, Becquerel was again experimenting with a photographic plate, when he found the sky to be overcast. He returned his plate and uranic salts to a dark cabinet to be used another day. After several days of cloud cover, Becquerel decided to develop the photographic plate and was amazed to find that the plate was not blank but darkened just as if the uranium had been exposed to sunlight. Thus began a series of experiments which led to the discovery of radioactivity.

2.3 Rutherford, Curies, et al.

Becquerel's discovery did not gain the immediate notoriety that Roentgen's had. Indeed, in the next year only a few short papers on the subject were published. What would later be seen as an important development, however, was the new interest in uranic rays by two young scientists: Ernest Rutherford and Marie Curie. Curie decided to study these uranic rays in 1897, and in April 1898, she submitted her first paper on radioactivity. In this paper, she made a few important new observations.

Firstly, she had found a new radioactive substance - thorium - showing that the phenomenon was not unique to uranium (this had also been discovered, unbeknownst to her, by Schmidt a couple of months earlier). Secondly, she concluded that the activity of uranium increased as the amount of uranium increased - a more quantitative description than Becquerel had given. Thirdly, she suggested that "radioactive properties are a diagnostic for the discovery of new substances" [25].

Pierre Curie, now very interested in this research, joined his wife in the endeavour to test this new idea. They had observed that a sample of pitchblende exhibited an activity about 4 times the level expected for uranium. Since previous observations of uranium had shown the activity to be "...proportional to the amount of uranium present and independent of its combinations with other inactive elements" [27], i.e. radioactivity was an atomic property, it was thought the relatively high levels of radiation might be due to the presence of another radioactive element. The two proceeded to analyze the chemical separation of pitchblende, and by December 1898, they had found two new radioactive elements - polonium and radium.

Around this same time, Ernest Rutherford was beginning his research on radioactivity at the Cavendish Laboratory in Cambridge, which led to several important discoveries. His experiments had shown that certain refraction and polarization properties, which Becquerel had claimed to observe, were not present, and that electrical currents in gaseous media were indicative of ionization of the gas by radiation; this provided a more direct means of measurement of radioactivity. He also found that uranium emitted "at least two distinct types of radiation - one that is very readily absorbed, which will be termed for convenience the α-radiation, and the other of a more penetrative character, which will be termed the β-radiation" [25]. He quantified this phenomenon by observing the effects of intervening materials on the intensity of the radiation detected. He showed that radiation from thorium was diminished significantly by a thin sheet of paper, but subsequent sheets did not continue to produce such a large effect (See Table 2.1) [28]. This indicates the presence of two differing types of radiation - one easily absorbed and the other more penetrating. Furthermore,

Number of Layers of Paper	Rate of Discharge
0	1
1	0.74
2	0.74
5	0.72
10	0.67
20	0.55

Table 2.1
Rate of electric discharge from a thorium sample as a function of thickness of intervening paper. Each layer was 0.008 cm thick. It can be seen that the rate of discharge is immediately affected to a large extent by the first sheet of paper and affected to a much smaller degree by subsequent sheets. This indicates one type of radiation is easily stopped by the paper, while the other is much more penetrative in nature [28].

Rutherford found that thorium emitted an additional radioactive substance, whose constituents "retain their radioactive powers for several minutes" [28]. In addition to having directly observed part of a decay chain, he had essentially discovered that different elements exhibit different half-lives. Rutherford also noticed that the radiation produced by thorium was affected greatly by small currents of air from opening and closing a door across the room from the experimental apparatus. This led him to experiment with controlled air currents while monitoring the decay rate of the thorium sample (Figure 2.1). He found, by isolating the newly produced emanation, that the intensity of radiation fell off rather quickly compared to that of uranium and thorium. Specifically, he showed that it dropped to half its original value in approximately one minute and decayed according to a geometrical progression in time (see Table 2.2 and Figure 2.2). He went on to show [28] that the intensity of radiation as a function of

Time (s)	Current (A)
0	1
28	0.69
62	0.51
118	0.23
155	0.14
210	0.067
272	0.041
360	0.018

Table 2.2
Rutherford's measurements of the decay of 'emanation' (^{228}Ra) from thorium in time [28]. Potential Difference noted to be 100 V.

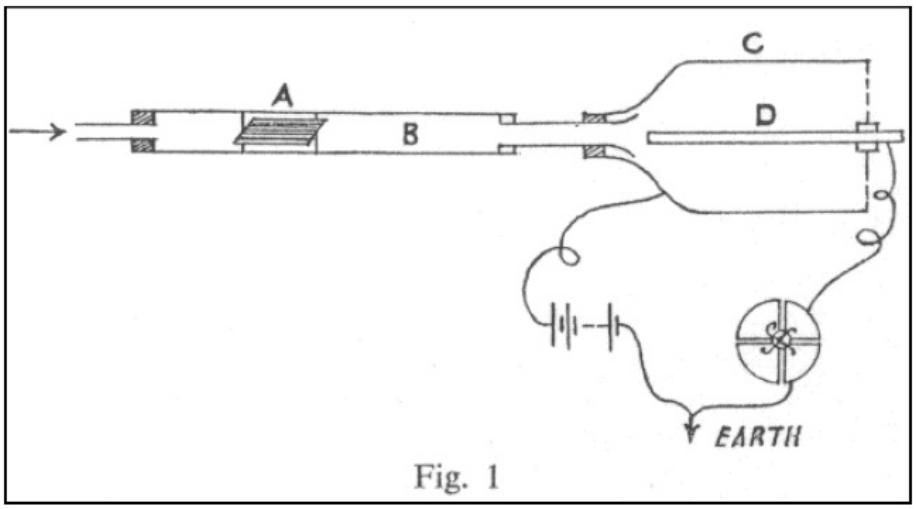

Figure 2.1. Schematic of the apparatus used by Rutherford to isolate the 'emanation', or new radioactive substance produced by thorium oxide at location A. The emanation was carried by a current of air through the metal tube, B, into C, where it ionized a gas and produced current [28].

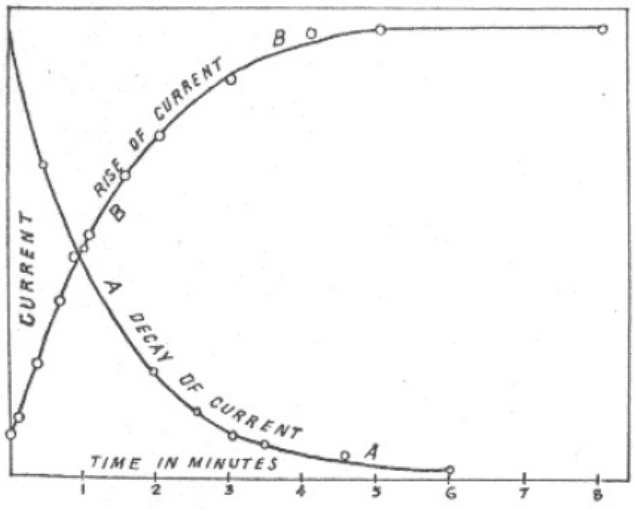

Figure 2.2. Current through Rutherford's gas detector as a function of time [28].

time follows:

$$I(t) = I_o e^{-\lambda t} \tag{2.1}$$

F. Soddy became a colleague of Rutherford when he gained employment at McGill University in 1900. The two began collaborating on experiments in radioactivity, and over the next few years, they constructed a general theory of radioactivity, which was published in several papers between September 1902 and May 1903. The theory contains six important claims. Written in a more modern terminology, they read:

i: The elements uranium, thorium, and radium continuously decay to new elements, which are also radioactive.

ii: Multiple decays through the decay chain are successive rather than simultaneous.

iii: The changes to an atom due to radioactivity are different from those seen in chemistry since the phenomenon is intra-atomic in nature.

iv: The number of atoms which decay in some time is proportional to the number of atoms that have not yet decayed, and this proportion is characteristic of and constant for the substance. This leads to the exponential decay law: $n = n_o e^{-\lambda t}$, where the average life of an atom is $1/\lambda$

v: α -particles are positively charged with a mass to charge ratio over 1000 times that of an electron. If α -particles and electrons have the same charge, this implies the α -particle has a mass similar to that of a hydrogen atom.

vi: The radiation emitted from atoms undergoing radioactive decay may not simply accompany the change of one substance into another, but actually embody the change itself.

In these early days, scientists tried to probe the nature of radioactive decay by all manner of interesting and clever experiments involving large changes in temperature and pressure, strong magnetic fields, and other such environmental parameters. One of the more dramatic experiments, conducted by Rutherford and Petavel, observed the γ-ray activity of a radium sample, which was placed inside a steel-encased cordite bomb. During the explosion, a temperature of 2500 °C and a pressure of roughly 1000 atm was estimated to have occurred, but no change in the γ-ray activity was observed. Many such experiments led early scientists to conclude that the decay constant of a radioactive substance was independent of the extranuclear environment [29], [30].

2.4 K-capture

It is now well-known that certain processes, such as electron-capture, are sensitive to their environment insofar as it affects the orbital electrons' wave function. For example, the probability of electron-capture occurring in a given atom depends on the K-orbital electrons' wave function multiplied by the spin wave function [31]:

$$\psi_e = \sqrt{Z^3/\pi a_0^3}\, e^{-Zr/a_0} \quad \begin{pmatrix} 1 \\ 0 \end{pmatrix} \text{ or } \begin{pmatrix} 0 \\ 1 \end{pmatrix} \tag{2.2}$$

By subjecting substances which undergo electron-capture to large electromagnetic fields, for example, one can affect the wave function of an orbital electron enough to change the decay rate slightly. This phenomenon is well-understood and is separate from our research interests.

2.5 Emery

G.T. Emery's paper, "Perturbation of Nuclear Decay Rates" [30], published in 1972, provides insight into the development of our understanding of decay rate considerations. He notes that, "One of the paradigms of nuclear science since the very early days of its study has been the general understanding that the half-life, or decay constant, of a radioactive substance is independent of extranuclear considerations." He goes on to detail how scientists arrived at this conclusion; "Early workers tried to change the decay constants of various members of the natural radioactive series by varying the temperature between 24 °K and 1280 °K, by applying pressure of up to 2000 atm, by taking sources down into mines and up to the Jungfraujoch [a mountain pass in the Alps], by applying magnetic fields of up to 83,000 Gauss, by whirling sources in centrifuges, and by many other ingenious techniques...Especially dramatic was an experiment of Rutherford and Petavel, who put a sample of radium emanation inside a steel-encased cordite bomb. Even though temperatures of 2500 °C and pressures of 1000 atm were estimated to have occurred during the explosion, no discontinuity in the activity of the sample was observed."

3. Modern Experiments

Oscillations in decay rates, the subject of the present work, have been documented in modern experiments but have typically been attributed to conventional environmental parameters such as temperature, humidity, and pressure changes, which may affect the detection apparatus. Certainly, these, along with other similar considerations, deserve scrutiny. However, analysis has also been presented which maintains that these factors cannot fully account for the effects seen in some experiments.

3.1 BNL

We became aware of the reported decay rate variations while investigating the possibility of using radioactive sources as random number generators. In the course of our research, we encountered a paper published by Alburger, et al. [1] regarding a half-life experiment performed at Brookhaven National Laboratory (BNL), which appeared to show some time dependence in the decay rate of their samples. Their experiment measured the half-life of ^{32}Si through the use of an automatic sample changer, which compared the counts collected for the silicon source to a long-lived reference, ^{36}Cl ($T_{1/2} = 301,000yr$), so as to allow for corrections due to systematic effects. Data were collected monthly between 1982 and 1986, totaling 53 data points, each of which consisted of the sum of twenty 30-minute counting periods for ^{32}Si interwoven with 20 30-minutes counting periods for the reference source. When the ratios of ^{32}Si to ^{36}Cl were plotted against time, a clear oscillatory behavior was observed with a magnitude approximately three times the statistical uncertainty of the data (see Figure 3.1). In order to compare the data from year to year, the counts were corrected for decay, normalized, and plotted according to the month in which they were collected (Figure 3.2). An annual oscillation is clearly evident.

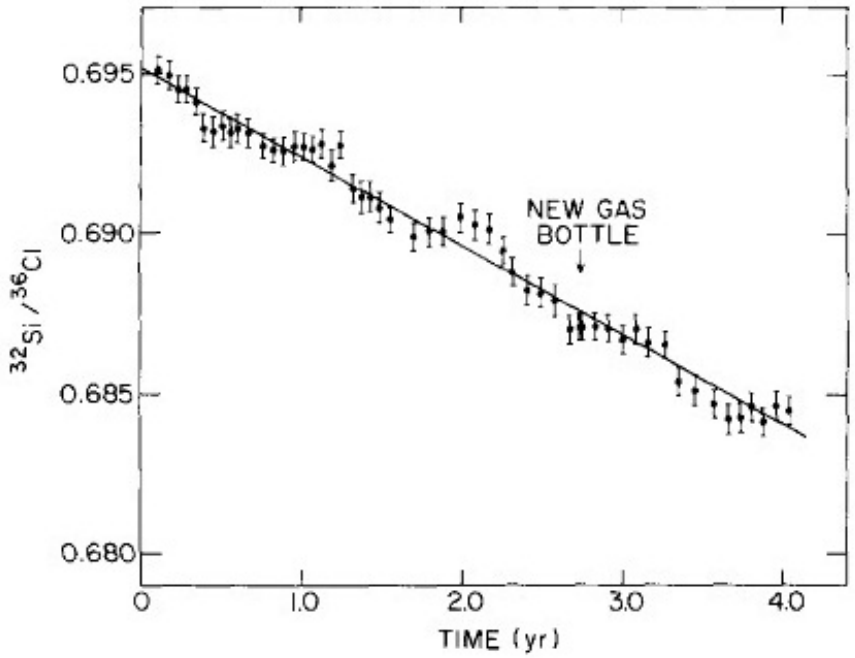

Figure 3.1. Figure 2 of [1] shows the ratio $^{32}Si/^{36}Cl$ counts over 48 months. Each data point is the average of 4 10-hour runs. Error bars were arbitrarily quoted at three times the statistical uncertainties by the researchers.

Characterization of the system suggested that effects due to shifting high voltage, air pressure, gas flow, and discriminator settings were too small to account for the fluctuations seen in the data. Environmental temperature and relative humidity were not recorded until the last several months of the experiment, when it was realized that they might be responsible for the fluctuations. Based on the limited measurements, it was estimated that these may account for fluctuations on the order of one standard deviation but were still not large enough to explain the magnitude of the effect seen in the data. Further analysis by Jenkins et al. [32], supports the claim that these environmental effects cannot fully explain the phenomenon.

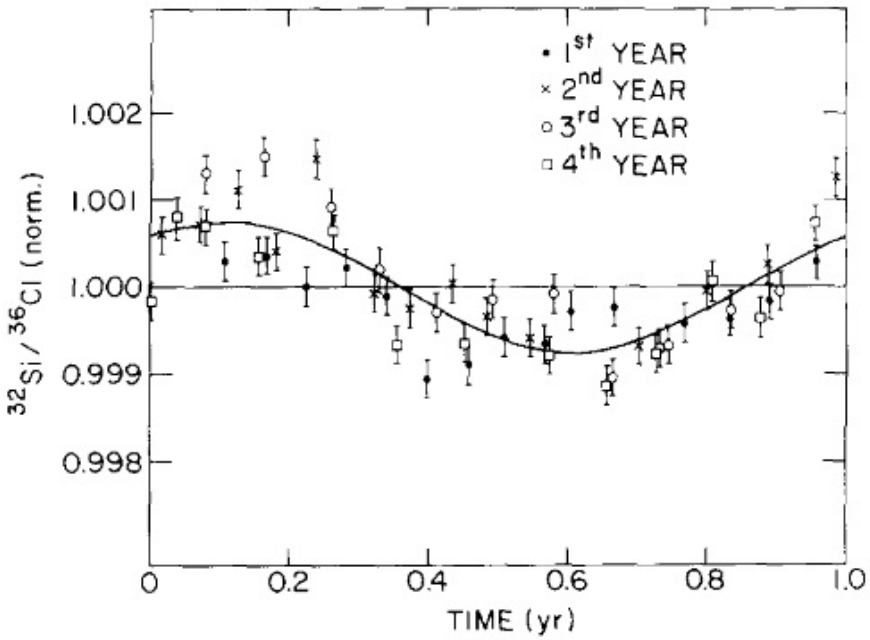

Figure 3.2. Figure 4 of [1] shows the previously presented data plotted, yearly, on top of one another. $T = 0$ is January 1. An arbitrary sine function fit gives an amplitude of 3.4 standard deviations (Error bars are statistical uncertainties).

3.2 PTB

The subsequent search for additional long-term nuclear decay data, yielded a paper regarding an experiment in which decay data were collected at regular time intervals for many years as part of a study on detector stability. The experiment, conducted by Siegert et al. [20], at the Physikalisch-Technische Bundesanstalt (PTB) in Germany, observed the decay of europium isotopes as well as ^{226}Ra for more than twenty years.

The experiment, in part, utilized a pressurized $4\pi\gamma$ ionization chamber for which a long-lived ^{226}Ra ($T_{1/2} = 1600$ yr) source was used as a reference. An automated sample changer cycled through measurements of a ^{154}Eu source, the reference source, and the background at regular intervals. The researchers noted, "The raw data from the ionization chamber measurement show small periodic fluctuations, unless taken

as ratios to the ionization current of the ^{226}Ra reference source...They may be fitted by a superposition of an exponential decay and a periodic function such as a cosine function with a yearly period." It should be noted that a similar signal was also seen in their secondary setup (utilizing a ^{152}Eu source and a Ge(Li) detector) but with a phase shift of about half a year relative to the ionization chamber. Interestingly, the ^{226}Ra signal correlated strongly with the $1/R^2$ Earth-Sun separation ($1/R_{ES}^2$), as did the BNL data. Futhermore, there is an overlap of approximately 2 years in the data sets, allowing us to evaluate the concurrence of this effect in data collected in different parts of the world using completely different equipment (Figure 3.3). Siegert et al.

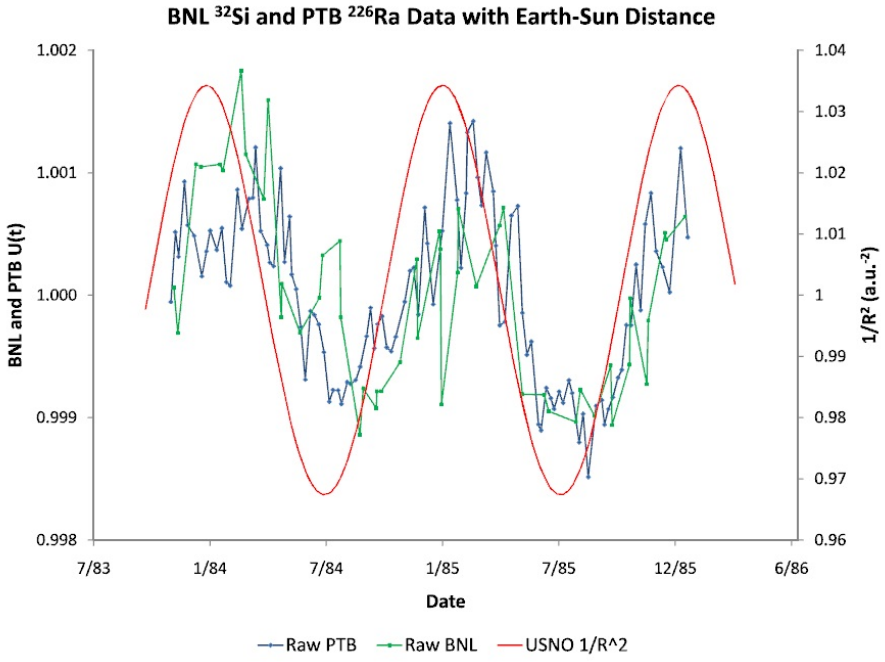

Figure 3.3. Raw BNL (^{32}Si/^{36}Cl ratio) and PTB (^{226}Ra) data plotted against $1/R_{ES}^2$, where R_{ES} is the Earth-Sun separation, show a compelling similarity.

attributed the oscillation to an effect of seasonal variations in background activity due to radon levels. However, Jenkins, Mundy, and Fischbach have argued [32] that

the radon mechanism proposed by Siegert et al. cannot, in fact, explain the periodic signal.

3.3 Ellis

Another instance of a periodic signal in decay rates is seen in a 1990 paper by Kenneth J. Ellis titled "The Effective Half-Life of a Broad Beam ^{238}PuBe Total Body Neutron Irradiator" [13]. In vivo neutron activation analysis is used to ascertain the elemental make-up of the human body or to track changes in one's elemental make up over time, so it is important to know precisely the effective half-life of the PuBe source. Ellis's study centered on determining the changes in the thermal neutron flux provided by the medical irradiator over time.

The irradiator utilized, in total, fourteen 50 Ci PuBe sources aligned above and below the person's body. The activity induced in the body was then observed by 54 NaI detectors positioned in two 9×3 arrays above and below the patient. Two types of standards were used to calibrate and monitor the performance of the detectors: i) nine ^{137}Cs sources placed daily between the upper and lower detectors along the middle row of the array and counted for 60 s. This calibration data showed no periodic signal. ii) a Lucite rod containing nine samples of epoxied manganese powder along its length. The rod was irradiated and placed in the counting apparatus such that the manganese sources lined up with the detectors in the same way as the ^{137}Cs sources. A total of 255 calibrations were made using the rod, and in this data, Ellis noticed a periodic variation.

It was concluded that "a seasonal difference of approximately 0.5% is seen between the winter and summer months" in this ^{56}Mn standard. Ellis also noted that a change in the counting efficiency of the system over time could be ruled out based on ^{137}Cs calibration data, whose half-life measurements, using the same system, were in excellent agreement with the accepted values in existing literature. By calculating

the effects of a build-up of daughter products and the presence of other isotopes of Pu, Ellis determined that the results would be too small to explain the discrepancies.

3.4 ^{54}Mn at Purdue

Jenkins and Fischbach report a perturbation in the decay rate of ^{54}Mn during a solar flare on December 13, 2006 [11], supporting earlier evidence of a correlation between nuclear decay rates and Earth-Sun distance [7]. A 1 μCi sample of ^{54}Mn was used in conjunction with a Bicron 2 $\times$ 2-inch NaI(Tl) crystal detector, Ortec PMT base with preamplifier, spectroscopy amplifier, and Maestro32 MCA software to record the 834.8 keV γ-ray emitted by the de-excitation of ^{54}Cr accompanying K-capture by ^{54}Mn. Attention was given to shielding the detector as well as to maintaining a temperature-stable environment. Although it has been suggested in the past that the solar neutrino flux on Earth may be affected by solar flares, existing experimental evidence is lacking. Jenkins and Fischbach propose that neutrinos from the solar flare were detected via the change in decay rate of ^{54}Mn. The solar flare occurred near the middle of the period of data collection (December 2, 2006 to January 2, 2007), though it was not realized at the time. Data from the Geostationary Operational Environmental Satellites (GOES), show spikes in both the x-ray and the proton flux from the Sun during the event. The ^{54}Mn decay data are shown with the x-ray flux recorded by the GOES-11 satellite in figures 3.4 and 3.5. One can see that some of the x-ray spikes are accompanied by obvious dips in the ^{54}Mn count rate, while others are not. The authors note that this discrepancy may provide clues as to the mechanisms which produce solar flares. Further, they suggest that changes in the ^{54}Mn decay rate which are not coincident with abnormal x-ray fluxes may be due to flares occurring on the far side of the Sun or other types of solar events. They reference one example: "In particular, the dip on 22 December (09:04 EST) was coincident in time with a severe solar storm, but did not have an associated x-ray spike" [11]. A statistical analysis of the time-coincident data yielded a probability on the order of

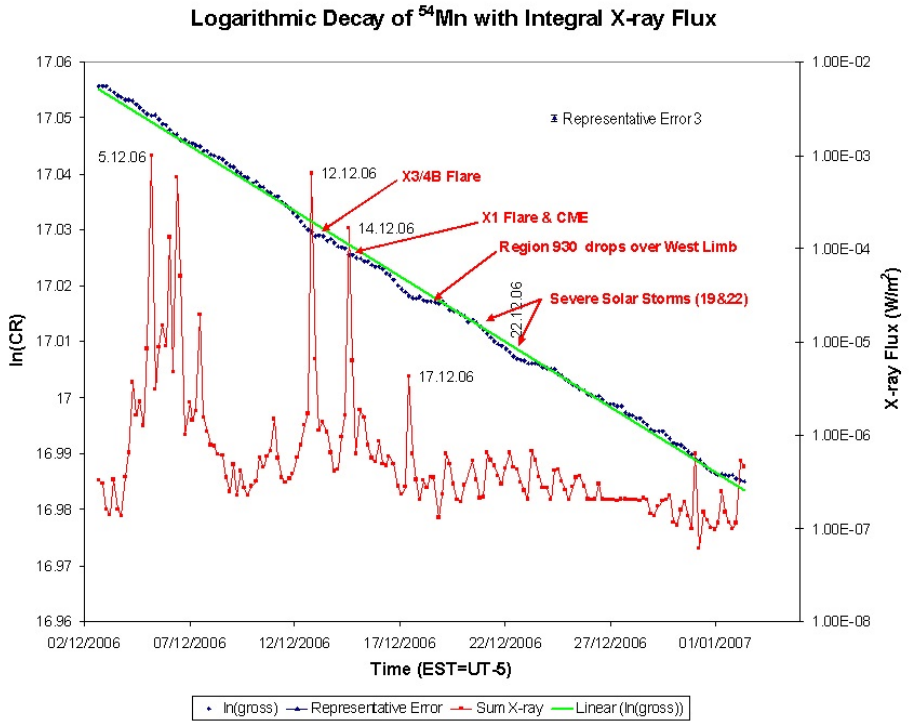

Figure 3.4. ^{54}Mn decay data superimposed on GOES-11 solar x-ray flux. Multiple deviations in the ^{54}Mn count rate are seen to be coincident in time with spikes in the solar x-ray flux [11].

1×10^{-13} of a random coincidence of a solar flare occurring with the large fluctuation in the Mn data. The further occurrence of a second such coincidence several days later indicates an overall probability which is "negligibly small", that this was simply a statistical accident.

Due to known electromagnetic effects produced by solar flares, such as power surges and changing local magnetic fields, the authors investigated the possibility that the changes in count rate originated in the hardware rather than the manganese sample, itself. Neither of the relevant power plants detected unusual properties in the grid, and, furthermore, the absence of any alarm indicates that the line voltage remained between 115 V and 126 V. The effect of varying line voltage would be a slight shift in the peak energy, which was automatically monitored and would be corrected

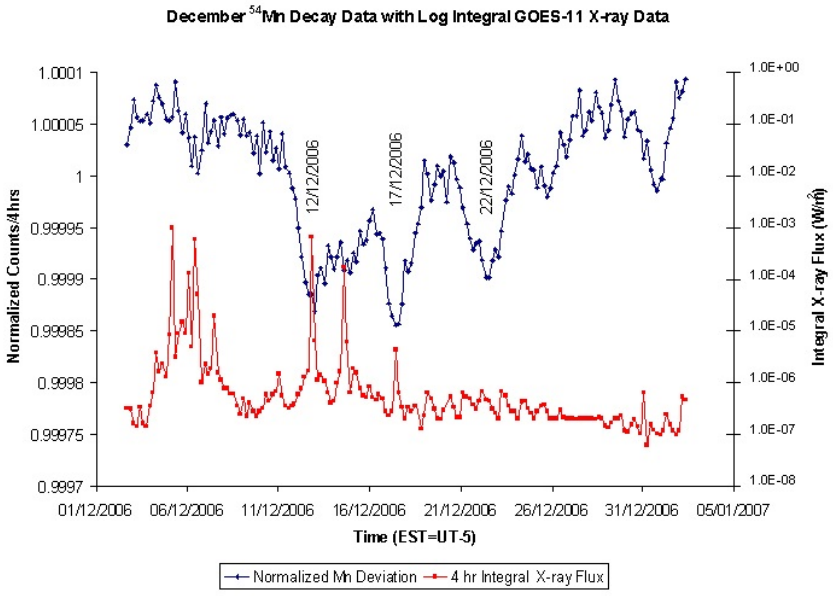

Figure 3.5. Normalized ^{54}Mn counts per 4 hours superimposed with 4-hour integrated x-ray flux [11].

for by the MCA software. There was reportedly no significant change to either the peak shape or location during the relevant period. In order to characterize the effects of changing local magnetic fields, the detector and photomultiplier tube (PMT) were set up within a pair of Helmholtz coils and a similar γ-ray emitter was monitored while varying the magnetic field up to 200 times that of any fluctuation measured in December 2006. The decay data (Figure 3.6) lack any statistically significant fluctuations. However, the most compelling evidence against an apparatus-dependent effect, as described by the authors, lies in the fact that the change in the ^{54}Mn decay rate begins more than a day before any spike in the GOES satellite data is seen. They argue that it is unlikely that other electromagnetic disturbances would reach the Earth before the x-rays, so it is reasonable to exclude the possibility of this effect being due to conventional electromagnetic effects associated with solar flares.

Consideration of the possibility of a changing neutrino flux, due to the solar flare, as the cause of the dip in count rate is given. Due to the orientation of the Earth at

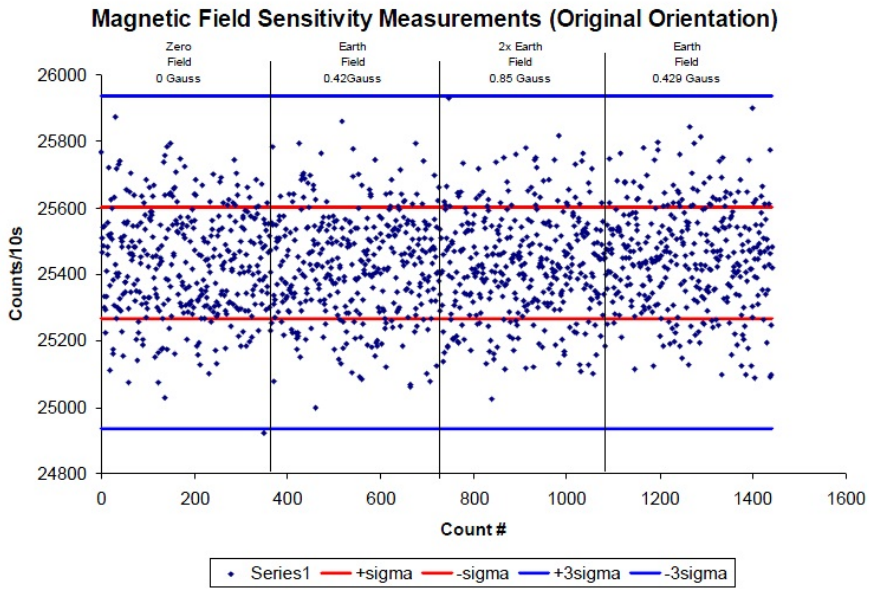

Figure 3.6. Each data point is a 10-second sum of counts of ^{137}Cs collected while varying the local magnetic field. The field strength was varied between 0 and $2B_{Earth}$ [11]

.

the time the x-ray spike was detected, the supposed neutrinos had to pass through roughly 9000 km of Earth before arriving at the ^{54}Mn source. Furthermore, a decline in the count rate preceded the maximum dip for 40 hours, though no diurnal signal is seen in the data as the Earth went through 1.7 revolutions. Hence, conventional electromagnetic effects and charged particles are dismissed as possible explanations. The authors suggest that neutrinos or neutrino-like particles, capable of passing through the Earth, may be responsible for the effect.

3.5 OSU

An additional set of decay data showing periodic oscillations comes from the Ohio State University Research Reactor (OSURR) and is analyzed by Jenkins et al. [10]. At the facility, a ^{36}Cl check source was used for weekly calibrations of a G-M detector,

purposed for collecting data from contamination survey wipes. The weekly data consists of a 120-second collection of gross counts with the ^{36}Cl source in the detector and a 600-second background count. Beginning in 2006, the check source's geometry inside the detector was controlled so that the placement was replicated for each run. A total of 337 data points were collected between January 7, 2005 and June 17, 2011. Each data point was normalized by dividing by the average count rate of all data points and plotted by date along with $1/R^2$ between Earth and Sun (Figure 3.7). The data exhibit an oscillation with a relative phase of the count rate similar to the BNL and PTB data. Analyzing the data by means of a power spectrum yields a clear frequency of 1 year (Figure 3.8).

The OSU data are of special interest, because they were collected using a G-M detector. These detectors are very simple in operation, as they require neither pre-amplifier nor amplifier for recording events. The temperature and pressure stabilities of similar G-M detectors have been well-documented and are not likely to be a contributing factor within the ranges observed at the OSURR facility.

3.6 Parkhomov

A.G. Parkhomov presented analyses of the periodicities found in several long-term radioactivity measurements [15], which showed variations in the activity of β-decays of ^{3}H, ^{56}Mn, ^{32}Si, ^{36}Cl, ^{60}Co, ^{137}Cs, ^{90}Sr-^{90}Y, and the daughter products of ^{226}Ra. These variations were not found, however, in the α-sources ^{238}Pu and ^{239}Pu (See Table 3.1).

Parkhomov found that eight different radionuclides exhibited fluctuations with a period of one year. Given that the data were collected by various groups using five different types of detectors and exhibited close agreement in magnitude and phase, Parkhomov concludes that one can "...state with confidence that the underlying cause of the periodic patterns in the count rates are the variations in the rates of radioac-

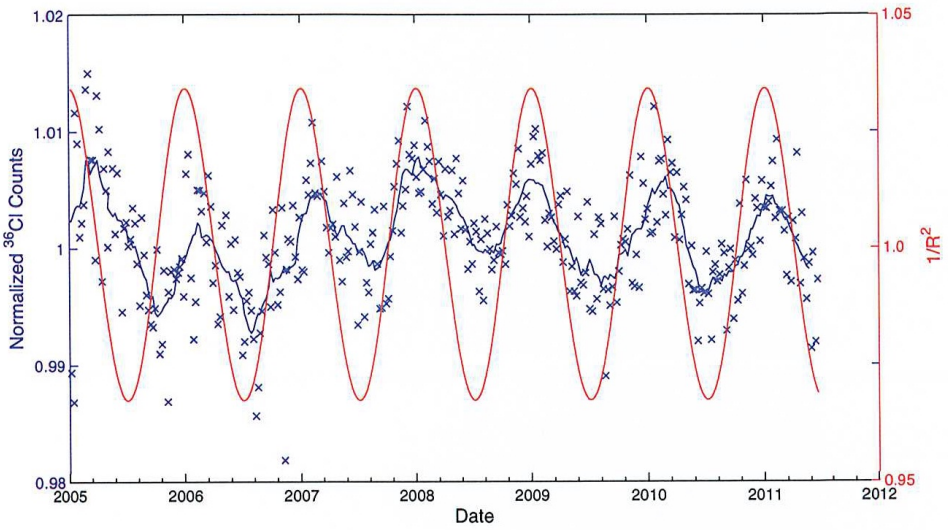

b

Figure 3.7. Normalized, weekly ^{36}Cl gross counts collected as part of a calibration routine at the OSURR overlayed with $1/R^2_{ES}$ distance between Earth and Sun [10].

tive decays rather than the drifts and non-stabilities of registering equipment" [15]. Spectral analysis yielded several significant periods in the data (Figure 3.9).

The one-year period displayed the largest peak-to-trough variation at 0.13% of the average count rate, while near-month periods had an amplitude of around 0.01%. Diurnal periods are also discussed, and it is argued that the total effects cannot be described simply by orientation relative to some anisotropy in space, nor by an influence due to solar neutrinos. The latter argument is based on the apparently weak interaction of high energy neutrinos with matter. Parkhomov then considers the hypothesis that β-decay is influenced by relic neutrinos. He argues that the data is in agreement, qualitatively, with expected effects due to the flux of these slow neutrinos through Earth.

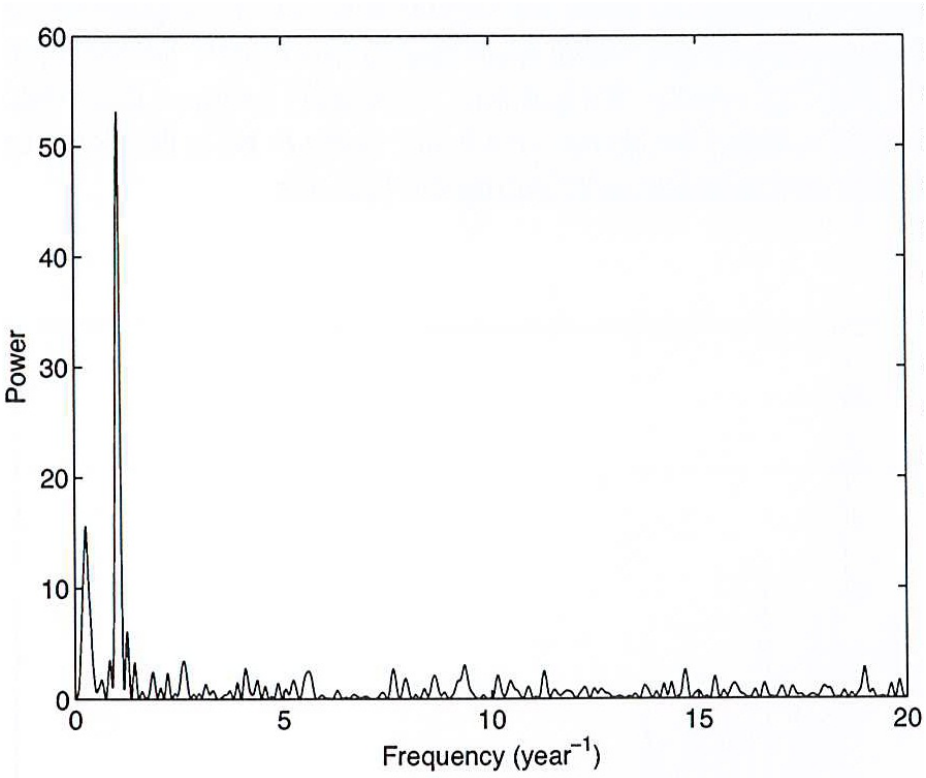

Figure 3.8. Power spectrum of OSU calibration data clearly shows an annual signal is present [10].

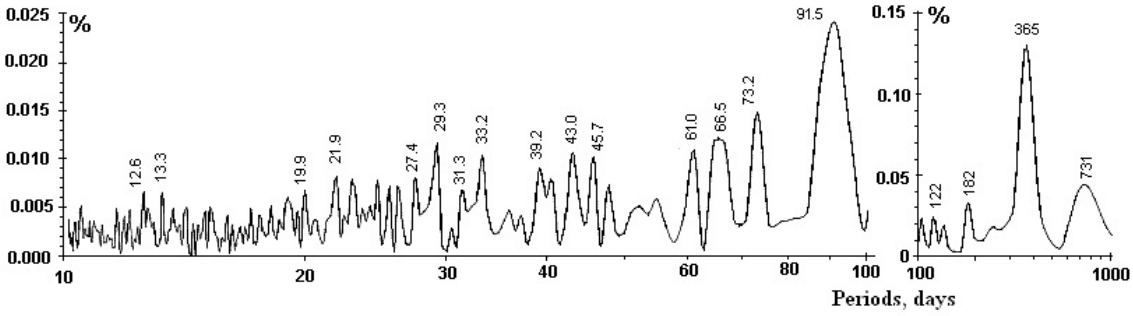

Figure 3.9. FFT analysis of ^{90}Sr-^{90}Y decay data converted to periods in units of days. The amplitude represents the percentage of the average count rate a given frequency contributes [15].

Ref.	Sources	Decay type	Detector	Time span	Periods, days (magnitude, %)	Months of high/low values
3	^{56}Mn	β^-	NaJ+PMT	02.78-01.87	365(0,3)	01/07
1	^{3}H	β^-	Scint.+photodiode	11.80-05.82	365(0,35)	02/08
4,14	^{32}Si	β^-	Prop. Counter	02.82-02.86	365(0,12); 32,5(0,01)	02/08
4	^{36}Cl	β^-, e.c.	Prop. Counter	02.82-02.86	365(0,12)	02/08
2,14	^{226}Ra	α, β^-	Ion. Chamber	10.83-06.99	365(0,1); cf. fig.3	01/08
9	^{137}Cs	β^-	NaJ+PMT	(19-23)04.94	1(0,06)?	
8	^{238}Pu	α	Energy evolved	10.97-10.99	None	
10	^{137}Cs, ^{60}Co	β^-, β^-	NaJ+PMT	12.98-04.99	1(?); ~30	
5-7	^{60}Co	β^-	G-M counter	03.99-10.03	365(0,2)	03/09
11,12	^{137}Cs, ^{60}Co	β^-, β^-	Ge(Li) semic.	03.00-04.00	1(0,5)?	
5-7	^{90}Sr-^{90}Y	β^-, β^-	G-M counter	01.00-12.10	365(0,13); cf. fig.1	03/09
5-7	^{239}Pu	α	Si-semic.	02.00-05.03	None	
5-7	^{90}Sr-^{90}Y	β^-, β^-	G-M counter	10.02-12.10	365(0,15)	03/09
6	^{239}Pu	α	Si-semic.	10.06-12.10	None	

Table 3.1
Summary overview of several radioactivity experiments as they pertain to variations in count rates [15].

3.7 Falkenberg

In the early 1980s, E.D. Falkenberg performed an 18-month experiment in which he monitored the decay of a tritium sample in order to determine if a periodic fluctuation, correlated with the solar neutrino flux, could be found [2]. The experimental setup consisted of a phosphorescent material containing tritium located near an array of photo diodes, whose sum current was recorded and analyzed. Falkenberg notes that special care was taken to avoid seasonal effects and long-term drifts. Characterization of the DAQ system yielded an overall temperature drift of 0.35% / °C with ± 0.01 °C short-term stability and ± 0.08 °C long-term stability. Falkenberg notes that the data collected reflect degradation effects on his detection system as well as the decay of the tritium, itself. Furthermore, he argues that the adequate suppression of environmental effects allows the assumption that this degradation is aperiodic, which, in turn, allows any periodic fluctuation present to be attributed to the decay of tritium rather than any degradation effect. Falkenberg's analysis showed that a

significant sinusoidal fluctuation with a yearly period and an amplitude of 0.37 % is present in the data.

3.8 Baurov

Y.A. Baurov et al. presented data and analysis of the β-decay count rate of ^{137}Cs and ^{60}Co collected between December 1998 and April 1999 [16]. The experimental setup consisted of one NaI detector to monitor background activity, a second NaI detector monitoring the decay of a ^{137}Cs source, and a BGO scintillator for the ^{60}Co source. The detectors were placed inside Permalloy cylinders meant to shield the PMTs from effects of the magnetic field, and data on both count rates and energy distributions were collected along with temperature and power-source voltage levels. The data analyzed was subject to minimal discrimination, having only low-energy noise cut off. After accounting for the temperature dependence of the decay rate, a Fourier transformation showed two distinct periods of 24 hours and 27 days.

3.9 Steinitz

G. Steinitz et al. studied samples of ^{222}Rn in order to probe the nature of known temporal variations in radiation levels associated with the substance [21]. Typical explanations of these variations include varying atmospheric conditions and subtle geodynamic processes. Specifically, "...atmospheric pressure and temperature have been proposed for the origin of the periodic signals observed in ^{222}Rn time series. However, other studies indicate that a consistent meteorological influence cannot be identified as giving rise to variability in ^{222}Rn time series..." [21]. Data from the Israel Geodynamic Radon Project, collected along the western boundary fault of the Dead Sea transform, exhibit: "a) unambiguous temporal signature types; b) recurrence at the different locations within the same geologic unit; and c) similar features recorded in diverse geographic, geological and geodynamic situations. The main types recognized are multi-year, annual radon, multi-day and daily-radon signals

as well as intense variations lasting up to several hours" [21]. Analysis of a further dataset led the authors to conclude that the annual and daily radon signals were likely caused by "a solar irradiance related process" [21].

In order to further understand the causes of these variations in radiation levels, the authors conducted three experiments utilizing sealed volumes containing samples of radon. In the first two experiments, multiple gamma detectors were placed outside the sealed volume in differing orientations. The data from experiment 1 exhibited large temporal variations consisting of a small, long term decrease, subtle, irregular, multi-day variations, and larger, periodic diurnal signals, whose amplitude was 10-25% of the nominal radiation level. Experiment 2 exhibited the same signals, with amplitudes of the diurnal component at 10-30% of the nominal value. Perhaps the most interesting observation was that "Dissimilar manifestations of the [daily radon] signal were recorded by gamma sensors located at different positions around the ^{222}Rn system indicating that the radiation pattern from ^{222}Rn in the experimental volume was non-uniform both spatially and in time. Such variation patterns cannot be attributed to release-emanation-exhalation processes, to mass transfer/exchange with the surrounding, nor with variations in pressure or temperature" [21].

While the first two experiments employed gamma detectors outside the sealed volume containing radon, experiment 3 utilized internal and external gamma detectors as well as an internal alpha detector. It was observed that as the ^{222}Rn came into secular equilibrium inside the tank, the amplitude of the daily-radon signal increased proportionally. This implies that the periodic signal originates within the ^{222}Rn gas inside the sealed container. An annual periodicity with a maximum in the summer and a minimum in the winter is clearly seen by the three internal detectors. There is a phase lag of 15-20 days in the alpha signal with respect to the gamma, while the environmental temperature peak lags that of the gamma signal by roughly 30 days. Further, the authors found that multi-day signals were observed by all detectors, as were daily periodicities, which differed among the detectors in amplitude, shape, and phase. The implication of the dissimilar yet related signals is that "such variation

patterns cannot be explained in terms of a varying concentration of a component [radon] of the gas phase within the confined system" [21]. Examination of the daily signal by means of the daily amplitude showed a reverse seasonal relationship between the alpha and gamma signals, i.e., the gamma data exhibit a maximum in the summer, while the alpha data show a maximum in the winter. A fast Fourier transform (FFT) analysis of the daily-radon signals yielded frequencies which match well-known solar tide frequencies of 24 h, 12 h, and 8 h. These observations led the authors to propose "that an external influence related to solar irradiance interacts with the ^{222}Rn system, homogeneously dispersed in the gas phase, leading to a spatially non-homogeneous radiation" [21].

3.10 Schnoll

Schnoll, et al. have found evidence of persistent, time-dependent, fine-structure features in several data sets, ranging from the biological to the physical domain and covering more than forty years [3]. In 1955, an experiment concerning the rates of biochemical reactions resulted in data points clustered mostly around a few discrete values. This was unexpected but initially attributed to a handful of biological phenomena. Subsequent experiments, however, apparently showed that these explanations were not sufficient. It was reported that they "...observed a striking similarity in the fine structure of histograms in different experiments, and an obvious regularity as they changed their shape in consecutive experiments." As the researchers sought to isolate the origin of this effect, their experiments transformed from biological in nature to purely physical. They eventually took detailed measurements of radioactive decay and, remarkably, found very similar fine-structure features in their two independent experiments. They note that, "Twenty-five years of research brought us to the conclusion that the discrete nature of the distributions of measured quantities is a nontrivial and universal feature." Further measurements of radioactive decay were taken with various detector types on a handful of different elements and decay

processes, taking care to eliminate or account for environmental contributors. As mentioned previously, Schnoll et al. found the shapes of their various histograms changed over time. Further analysis showed a strong likelihood of these shapes repeating with periods of 24 hours, 27 days, and 365 days. This led them to consider the source of the phenomenon as cosmogonic in nature.

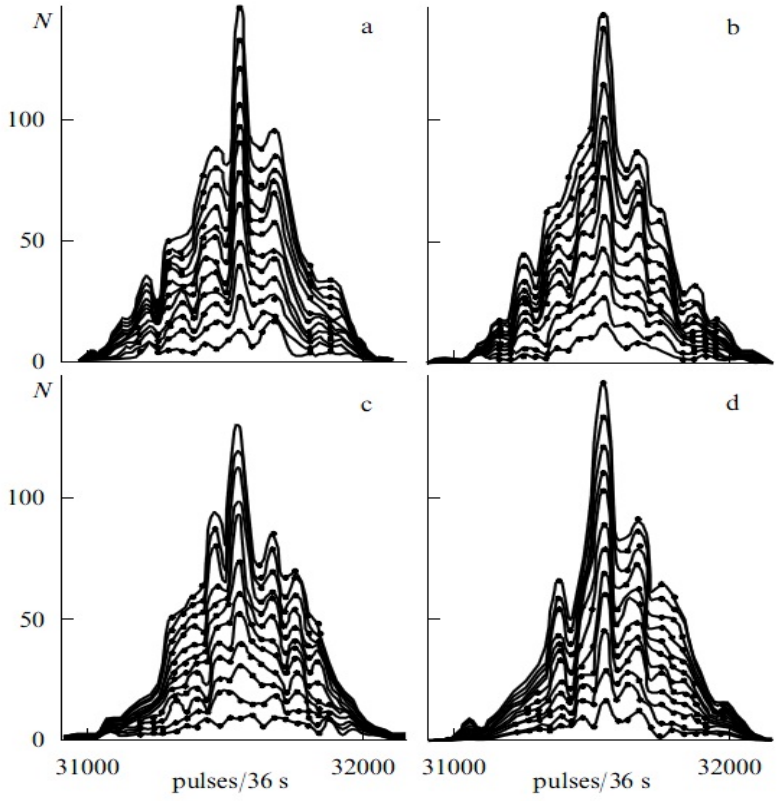

Figure 3.10. Figure 1 of [3] illustrates common features in measurements of radioactive decay of a ^{55}Fe sample.

3.11 DAMA/LIBRA

The following discusses a past analysis done in collaboration with J. Nistor, which is of interest to the current discusison. DAMA/LIBRA is a second-generation ex-

periment designed, in part, to exploit the theorized annual modulation signature of dark matter in the galactic halo ([33], [34], [35], [36], [37], [38]). The experiment is located in Italy at the underground Gran Sasso National Laboratory and began collecting data in March of 2003. Special attention has been given to the building materials in order to ensure low levels of radioactivity. The experiment utilizes approximately 250 kg of highly radio-pure NaI(Tl) housed along with the rest of the DAQ system inside 1 m of concrete made from Gran Sasso rock and further shielded by lead and paraffin [33]. Multiple systems are in place to seal out environmental radon, and a sensor monitors and records the level in the experimental room. Stable operating temperatures are ensured by means of a redundant air conditioning system, and operating conditions are recorded with the experimental data. The 250 kg of NaI(Tl) comprises 25 detectors, each of size $10.2 \times 10.2 \times 25.4\ cm^3$. The 9.70 kg detectors are arranged in 5 rows by 5 columns, and along with two PMTs for each detector, are housed in a sealed, low-radioactive-copper enclosure flushed with high-purity N_2.

As of 2010, DAMA/LIBRA had accumulated an exposure of 0.87 ton×yr over 6 years, which is combined with DAMA/NaI's 7-year 0.29 ton×yr exposure. The cumulative data (1.17 ton×yr) are plotted in Figure 3.11 [35]. Since the probability of a dark matter particle interacting with more than one detector is negligible, only single-hit events are analyzed in a normal data run. A software energy threshold of 2 keV is also applied. Indeed, while the single-hit residuals show features consistent with a dark matter modulation signal, analysis of multiple-hit events yields no such signal. One interpretation of the DAMA/LIBRA data, which is of interest to our research, is that a modulation of ^{40}K contamination in the NaI detectors could explain the signal being seen.

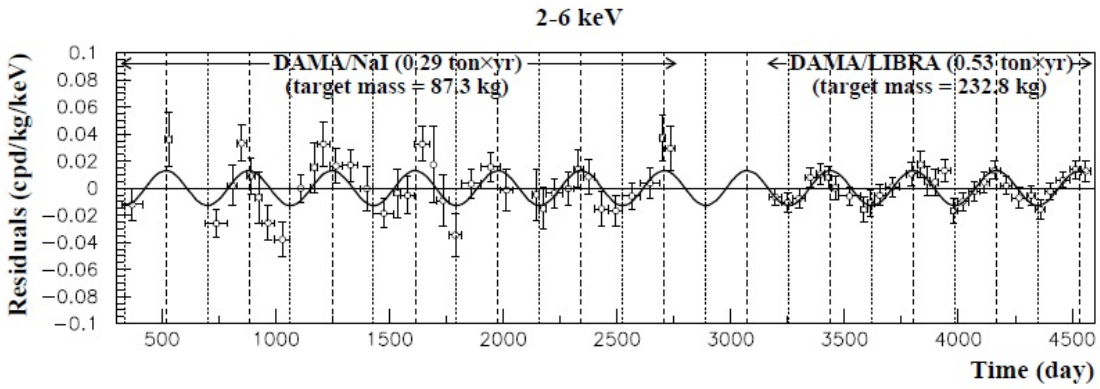

Figure 3.11. Figure 1 from reference [35] shows the combined 11-year, single-hit event residuals from DAMA/NaI and DAMA/LIBRA in the 2 - 6 keV range. The zero time, t_0, corresponds to January 1 of the first year of data. Horizontal bars represent the time bin-width. The fit curve is a cosine function with period = 1 yr and phase which corresponds to June 2.

Contaminants

Even with the careful selection of materials, there exists some level of undesired radioactivity in various components of the installation, which may affect the background signal. Some information about these contaminants has been reported by the group, but complete data remains undisclosed. Kudryavstev, Robinson, and Spooner conducted Monte Carlo simulations of expected background rates, using their existing knowledge of modelling background signals and their experience in running the NAIAD dark matter experiment [39]. A synopsis of their results and interpretations is presented here.

The event rate in a given energy bin can be written as:

$$R(E,t) = b(E) + S_0(E) + S_m(E)cos(\omega(t - t_0)), \tag{3.1}$$

where b is the background rate, S_0 is the non-modulated component of the dark matter signal, S_m is the amplitude of the modulated component of the dark matter signal, ω is the frequency of modulation, and t_0 is the time of the signal maximum. Given, that the time-dependent, modulated portion of the dark matter signal will contribute nothing when averaged over an integer number of years, one can test the agreement between the sum of the reconstructed spectrum of the signal, $S_0(E)$, and the background, $b(E)$, with the measured spectrum. To this end, the expected background signal is simulated.

The analysis considers three possibilities for background radioactivity, including sources external to the NaI crystals, sources within the crystal's volume, and sources within the thin surface layer of the crystals. The two latter simulations gave similar results, so only the first two scenarios will be discussed here. A model was constructed using the published geometry of the DAMA/LIBRA set-up, and for the first case, background radiation was simulated to originate in the PMTs attached to the crystals by light guides. For normalization, the concentrations of radioactive isotopes used were typical of ultra-low background PMTs. These are in the range of 20 - 60 ppb for ^{238}U, ^{232}Th, and $^{\mathrm{nat}}$K. Considering DAMA/LIBRA's method of data collection, only single-hit events above 0.5 keV were included.

Next, background sources distributed evenly throughout the crystal volume were modelled. In addition to uranium, thorium, and potassium contaminants, ^{129}I and ^{22}Na were included. The concentration values reported by DAMA were used for normalization, here, although the available data is not complete. Figure 3.12 shows the combined simulated events. The simulated signal (solid curve) below 10 keV is about an order of magnitude smaller than DAMA/LIBRA's reported 1 event/kg/day/keV. A signal similar in amplitude to that reported by DAMA/LIBRA, was achieved by simulating 2 to 8 times the reported contamination levels of ^{238}U, ^{232}Th, and $^{\mathrm{nat}}$K in the crystal (dashed curve). Similarly, the results of higher external contamination (dotted curve) is shown.

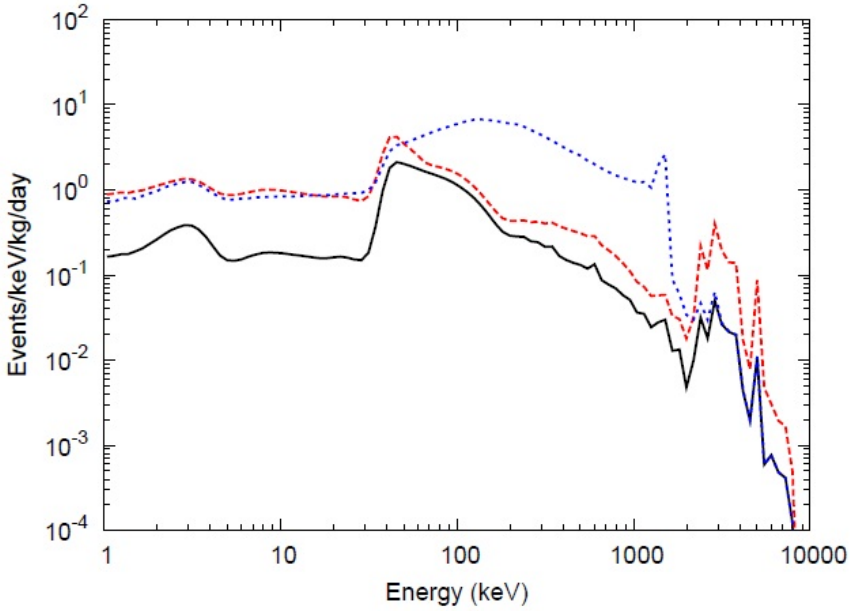

Figure 3.12. Figure 4 from reference [39] shows the combined events from simulated background radiation in the PMTs and crystals. The solid line represents the assumed contamination levels, while the dotted and dashed lines represent increased levels of contamination in an attempt to make the simulated data fit DAMA/LIBRA's reported signal (See text for details)

.

Figure 3.13 shows the low-energy simulated events, using the aforementioned increased contamination levels. The simulated spectrum is compared to the measured signal in three ways: i) no WIMP signal subtraction (open squares), ii) subtraction of signal from 60 GeV (assumed) WIMPs with σ_{SI} = 7 x 10^{-6} pb (filled squares), and iii) subtraction with σ_{SI} = 2 x 10^{-6} pb (empty circles).

Decay Rate Modulation

Kudryavstev et al. note that further adjustments are needed in order to bring the simulated background into better agreement with the measured data, but we are

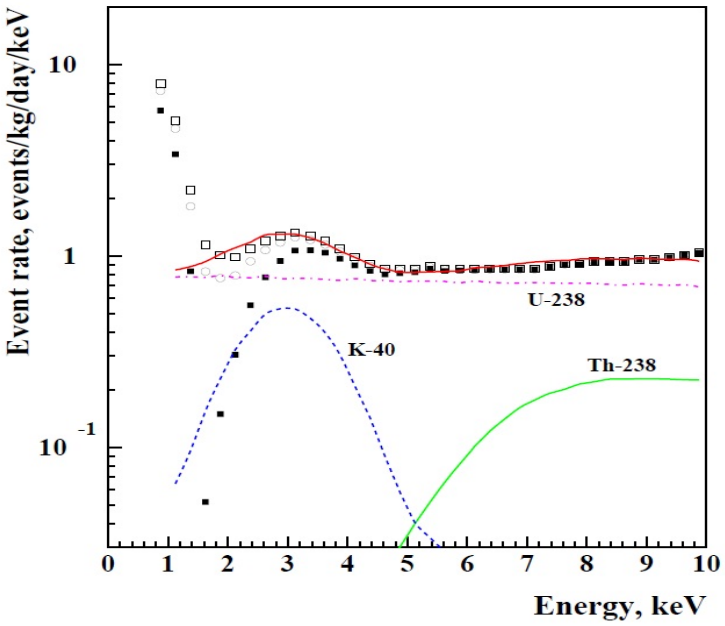

Figure 3.13. Figure 5 from reference [39] shows the combined low-energy events from simulated, background (solid curve) for increased concentrations of contaminants. The measured DAMA/LIBRA signal is shown using open squares. The filled squares and open circles represent this signal after subtracting assumed contributions from 60 GeV WIMPs

.

mainly interested in the small peak near 3 keV. It is clear in Figure 3.13 that this peak is due to the simulated ^{40}K contamination present in the crystal. As Kudryavstev, Robinson, and Spooner note, this may explain the annual modulation DAMA/LIBRA sees around the 3 keV peak.

Naturally occurring potassium consists of 0.0117% ^{40}K, which has a half-life of approximately 1.25×10^9 yr. ^{40}K's branching ratio is roughly 89% β decay to the ground state of ^{40}Ca (Figure 3.14) and 11% electron capture to an excited state of ^{40}Ar (Figure 3.15) [40], which yields a 1461 keV γ (nuclear de-excitation). Additionally,

3.2 keV of energy is liberated through x-rays or auger electrons associated with the replacement of the captured K-shell electron.

Due to a short interaction length, the 3.2 keV x-rays or auger electrons are essentially always collected by the originating detector, while the 1461 keV γ-rays may escape and interact with adjacent detectors. The DAMA/LIBRA collaboration has looked at these double-hit events, consisting of a low-energy event in one detector and a higher-energy event in an adjacent detector (see Figure 3.16). The correlation between the 1461 keV γ-ray with a 3.2 keV event is clear. In fact, DAMA/LIBRA analyzed the detection efficiency for such double-hit events in order to place a limit on the contamination of ^{nat}K in their detectors.

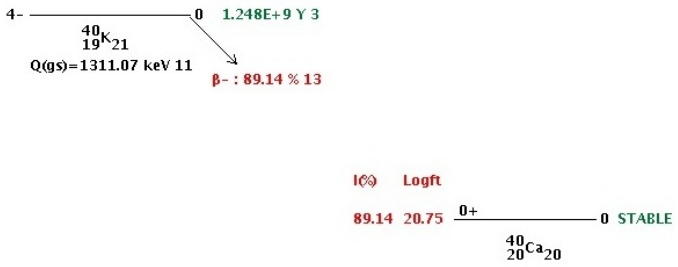

Figure 3.14. Decay scheme for ^{40}K via β to the ground state of ^{40}Ca [40].

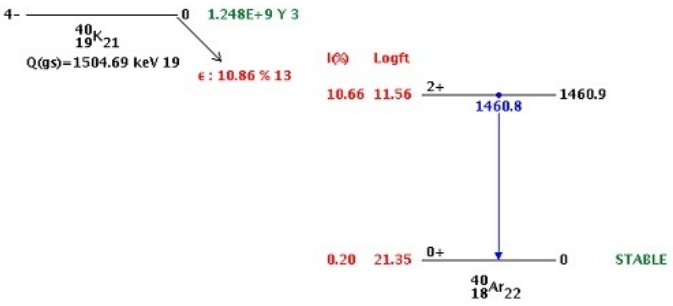

Figure 3.15. Decay scheme for ^{40}K via electron capture to ^{40}Ar [40]

.

DAMA's analysis of the coincidence data illustrated in Figure 3.16 places the ^{nat}K content in the crystals at ~ 20 ppb [33], so the total amount of ^{40}K in the NaI target can be estimated by the following

$$\begin{aligned} M_{^{\mathrm{nat}}\mathrm{K}} &= 20 \times 10^{-9} \times M^{*}_{target} \\ M_{^{40}\mathrm{K}} &= 0.000117 \times M_{^{\mathrm{nat}}\mathrm{K}} = 2.34 \times 10^{-12} \times M^{*}_{target} \\ &= 5.45 \times 10^{-10}\,\mathrm{kg} \end{aligned} \tag{3.2}$$

where M is mass. Hence, the total particle concentration of ^{40}K is given as

$$N_{^{40}\mathrm{K}} = \frac{M_{^{40}\mathrm{K}}}{m_{^{40}\mathrm{K}}} \times 6.022 \times 10^{23} = \frac{5.45 \times 10^{-10}\mathrm{kg}}{39.964 \times 10^{-3}\mathrm{kg/mol}} \times 6.022 \times 10^{23} = 8.2 \times 10^{15}\,\mathrm{atoms} \tag{3.3}$$

The decay of ^{40}K into ^{40}Ar via electron-capture occurs with a branching ratio of 10.72% and involves a K-shell electron approximately 76% of the time. Its half-life is 1.248×10^{9} years or $T_{1/2} = 4.55 \times 10^{11}$ days (half-life taken as quoted by DAMA collaboration [35]). Therefore the number of k-capture events per day is on the order of:

$$R = 0.1072 \times 0.76 \times \lambda \times N_{^{40}\mathrm{K}} = 0.1072 \times 0.76 \times 1.52 \times 10^{-12} \times 8.2 \times 10^{15} = 1054\,\mathrm{cpd} \tag{3.4}$$

where $\lambda = \log 2 / T_{1/2} = 1.52 \times 10^{-12}\mathrm{d}^{-1}$. This rate is approximately 4.5 cpd/kg, which corresponds to 2.3 cpd/kg/keV, some fraction of which likely contribute to their single hit event rate of 1.3 cpd/kg/keV. The various reports of modulation in radioactive decay data that are outlined in this chapter have motivated us to investigate the issue further. In the next chapter, we discuss our work in independently studying the decay of ^{32}Si, utilizing the source observed in the previously discussed BNL experiment.

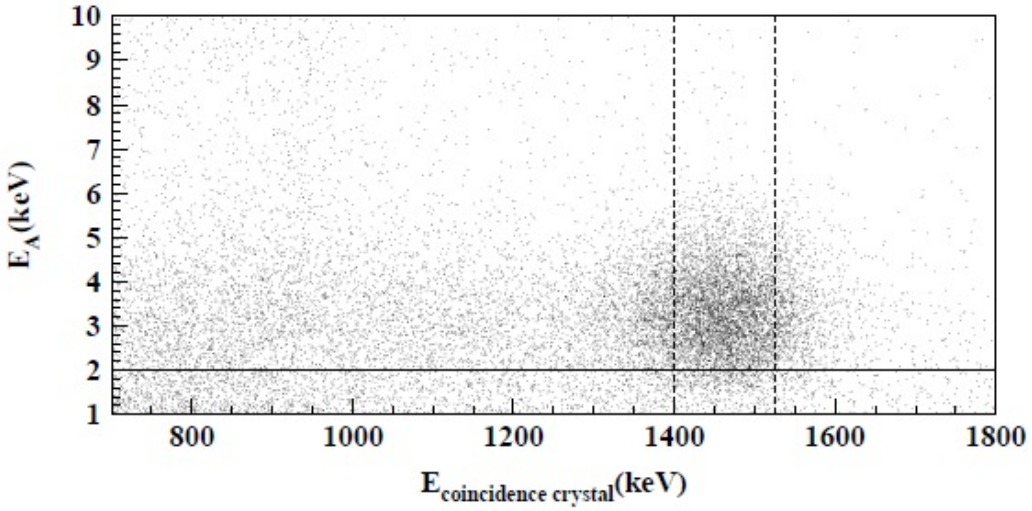

Figure 3.16. Figure 9 of reference [33] shows low-energy events occurring in one detector as a function of simultaneous events in other detectors.

4. NuHaven

4.1 Overview

The sample changer implemented in the original BNL measurements [1] of the half-life of ^{32}Si was provided to us and modified for the NuHaven (NH) experiment. Modifications include a collar designed to secure our detector to the sample changer (Figure 4.1), sensors for automatic confirmation of sample placement, and snubbers to dampen the motion of the sample cart as it arrives at the end of the rails. We built a modern data acquisition (DAQ) system including additional environmental control and extensive logging. The sample changer was placed in a modified 55-gallon steel drum and kept at a controlled pressure with dry nitrogen, which also allowed us to minimize variations in relative humidity, while the temperature of the room was controlled by means of a water-cooled air conditioner. This allowed us to remove the window-mounted air conditioner and heavily insulate the windows in order to improve temperature stability in the room. The DAQ system consists of a 2-inch Bicron plastic scintillation detector coupled with an Ortec 276 base with preamp. A spectroscopy amplifier and MCA connected to a PC running Maestro32 and custom LabVIEW software make up the rest of the DAQ system.

The original ^{36}Cl and ^{32}Si samples used in the BNL experiment were also provided to us. The ^{32}Si sample was produced using SiO_2 enriched in ^{30}Si to 95.55% from Oak Ridge National Laboratory [1]. The triton beam facility at BNL was then used to produce the ^{30}Si(t,p)^{32}Si reaction, beginning in December 1968. When available between other experiments, the triton beam was used to irradiate the target, and by April 1969, the target had received a total beam charge of 1150 μAhr (4.14 Coulombs). Considerable chemical processing of the sample began in late 1971 in order to remove organic compounds in the epoxy used to secure the SiO_2 powder for irradiation.

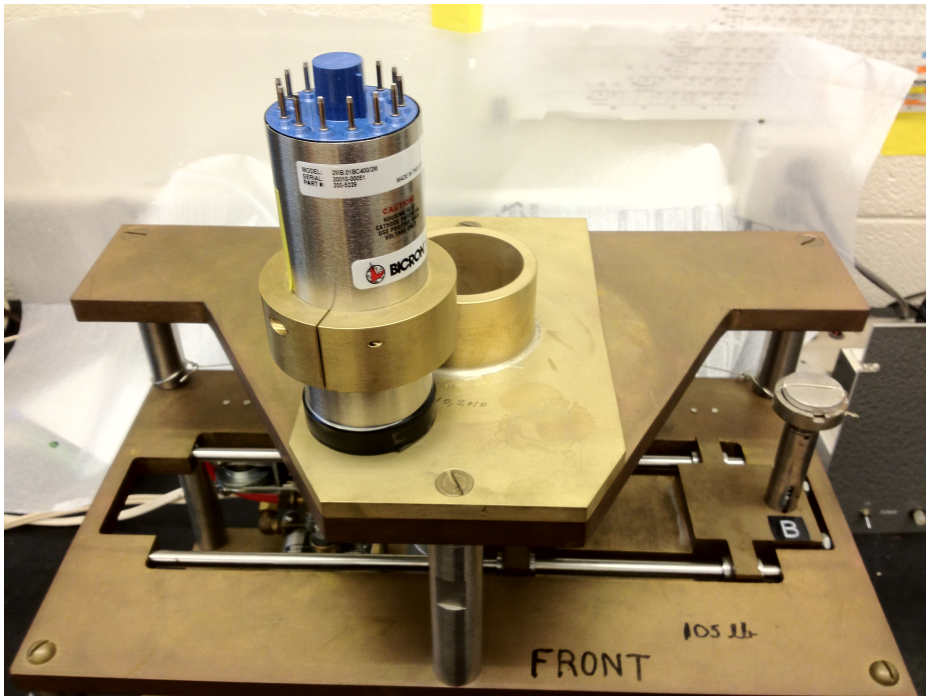

Figure 4.1. Detector mount fabricated to accommodate the new detector on the original BNL sample changer. The detector slides down into the top plate of the sample changer, and the collar attached to the detector holds it at the desired height.

Finally, 47.7 mg of SiO_2 powder was cemented in a brass source holder and bonded with electrically conducting cement to an aluminum foil so as to prevent possible surface charging of the source.

The sample changer alternates between the long-lived ^{36}Cl and ^{32}Si every 30 minutes for the duration of each run (200 cycles, book-ended by background measurements). This interweaving of ^{36}Cl and ^{32}Si observations is designed to minimize the effect of systematics in the DAQ system. Temperature, pressure and %RH are monitored by a NIST traceable data logger (TR-73U by T&D Corp.) inside the drum and capable of $\pm 0.3^{\circ}$ C, ± 5%RH, and ± 1.5 hPa accuracy. The readings have been shown to be repeatable to the tenths digit, the limit of the resolution of the device. Based on the pressure reading, the software determines the desired state of a valve

(open/close), controlling the flow of nitrogen into the drum. The magnetic field is monitored with a 3-axis magnetometer running on an Arduino micro-controller, and the high voltage supplied to the detector is recorded with an ADC, as is the line voltage. All of these parameters are recorded by the LabVIEW program every 60 seconds (See figures 4.2 and 4.3).

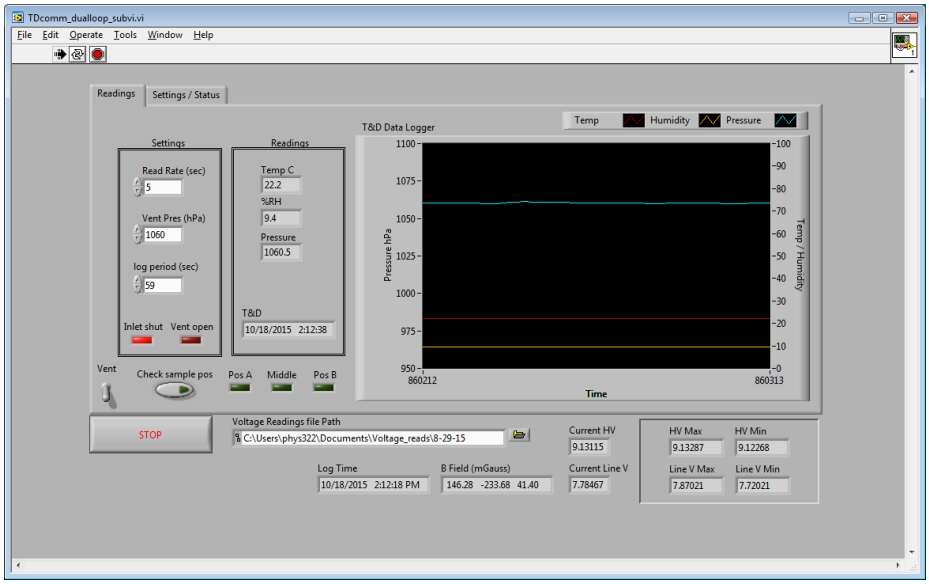

Figure 4.2. Custom Interface for controlling, monitoring, and logging environmental data.

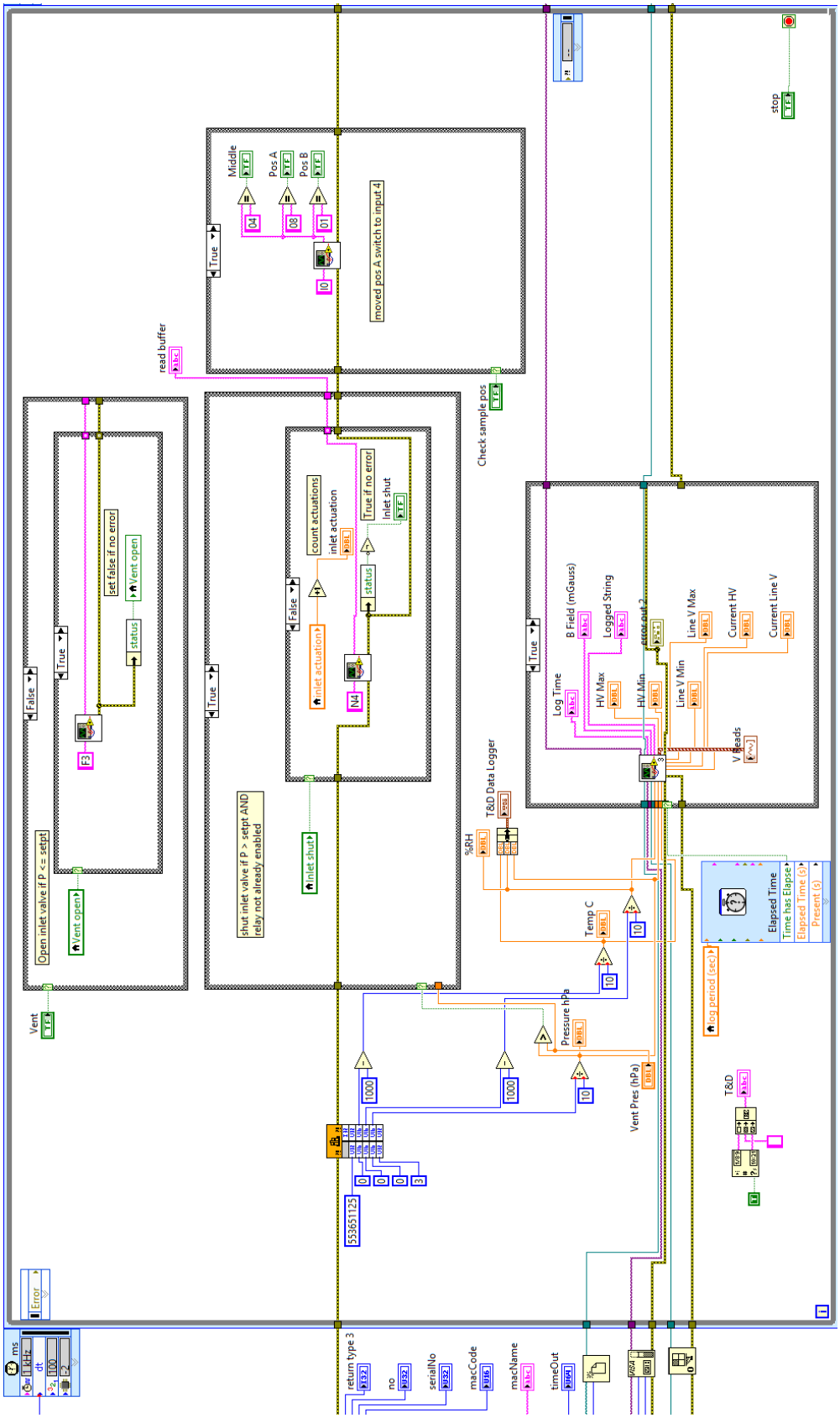

Figure 4.3. Part of the data acquisition program code for controlling and logging environmental data.

Det. Orientation	B Orientation	Coil Current (A)	Count Rate (cps)	Peak Pos. (Channel)
Horizontal	Down	-2.31 A	104.81 cps	84
Horizontal	Off	0 A	104.85 cps	85
Horizontal	Up	2.04 A	105.4 cps	85
Vertical	Down	-2.3 A	121.57 cps	65
Vertical	Down	-1.1 A	122.49 cps	85
Vertical	Off	0 A	122.87 cps	84
Vertical	Up	1.1 A	122.10 cps	86
Vertical	Up	2.3 A	121.86 cps	71

Table 4.1
Characterization of detector's response due to changing magnetic field. Since we found that the detector was possibly susceptible to changes in magnetic field along the detector axis, we repeated the above measurements for 1.1 A coil current and an extended acquisition time. These observations confirmed that no significant change in CR or peak location occurred for a magnetic field of 2 Gauss (approx. 4 times Earth's magnetic field).

4.2 System Characterization

Several tests were performed on the system in order to characterize its dependence on changing environmental conditions. The detector was placed in various orientations relative to a controllable magnetic field produced by a set of Helmholtz coils. The detector response was evaluated at approximately 2 Gauss (1.1 amp coil current) and 4.6 Gauss (2.3 amp coil current) in axial and perpendicular orientations (relative to the detector axis), and the ^{36}Cl sample was observed for changing count rates and peak position. At 2 Gauss (4 times the Earth's magnetic field), no significant change in count rate or peak position was found, but at 4.6 Gauss, the peak position shifted significantly for the case where the magnetic field was oriented axially relative to the detector (see Table 4.1).

The DAQ system and high voltage (HV) supply were connected to a constant voltage tranformer, whose output is nominally 117 V, in order to mitigate effects from fluctuating line voltage. The HV output was found to be stable to 0.1 V given

an input ranging from 109 to 125 volts. The output only began to drop when the input was decreased to 92.1 V. The NIM bin DAQ electronics, whose specifications require 103 - 129 V, were also tested in the same range of applied voltage and found to be stable to better than one channel in gain.

Early characterizations based on temperature showed that the HV output varied with temperature at around 0.8 channels/ °C. However, the recording of the HV output mitigates the need to extrapolate this relationship from the room's temperature. The recent addition of a peltier temperature control system has allowed us to more precisely characterize the system's dependence on both temperature and HV while isolating the HV supply from the rest of the DAQ components. The detector with PMT and NIM bin were characterized by incrementing the temperature of their enclosure 1 °C at a time, between 21 °C and 25 °C and recording the decay spectra. Separately, the dependence on detector voltage was quantified by changing the HV in 5 V increments while holding the temperature of these components constant. The observed counts per 30-minute interval for both ^{32}Si and ^{36}Cl are shown in figures 4.4 - 4.7.

Although determining the ratio of ^{32}Si to ^{36}Cl largely mitigates systematic effects, the unique energy spectra of the two samples respond to a change in detector voltage differently. An increase in voltage brings fractionally more low-energy counts into the integration region for ^{36}Cl than what is pushed out at the upper end. The opposite is true for ^{32}Si, so not only are the effects different in magnitude but also opposite in direction. ^{36}Cl shows a fractional dependence on detector voltage of approximately 2.4×10^{-4}/V, while ^{32}Si exhibits approximately -1.6×10^{-4}/V. In order to account for these effects, a scaling algorithm, discussed in the next section, was developed. The effect of temperature on the detector and DAQ system is much less evident. The ^{36}Cl data show no obvious effect, though the ^{32}Si data exhibit an increased spread during and after the cooling period. In order to ensure that no solid angle changes due to placement occurred while characterizing for temperature and HV, the ^{36}Cl data were taken while increasing those parameters, independently, and the ^{32}Si data

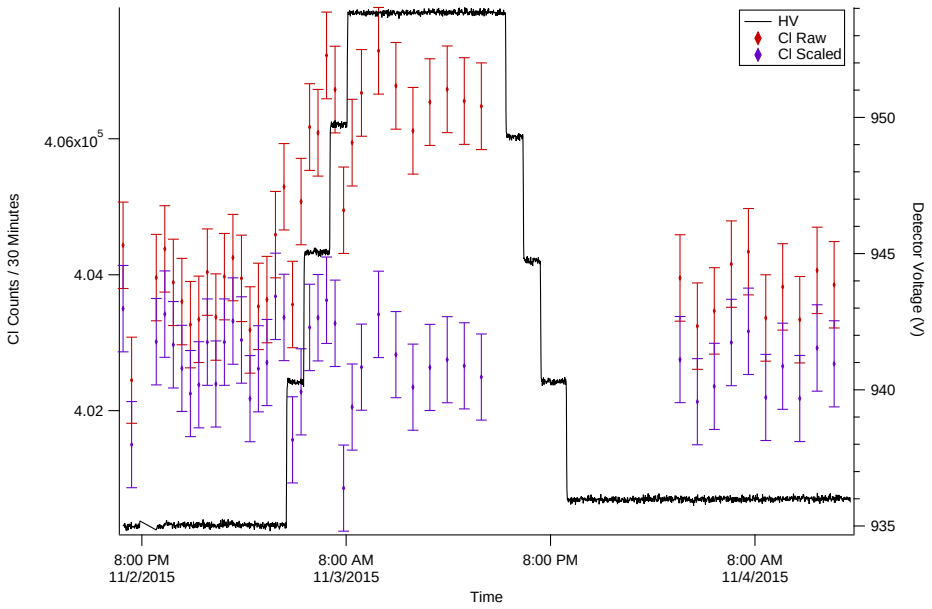

Figure 4.4. 30-minute raw and scaled ^{36}Cl counts while changing the detector voltage.

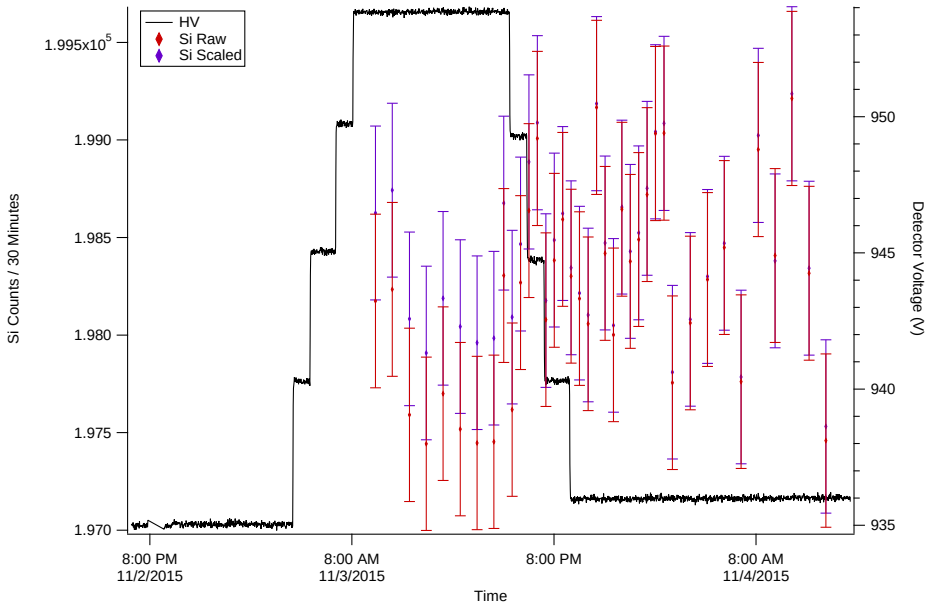

Figure 4.5. 30-minute raw and scaled ^{32}Si counts while changing the detector voltage.

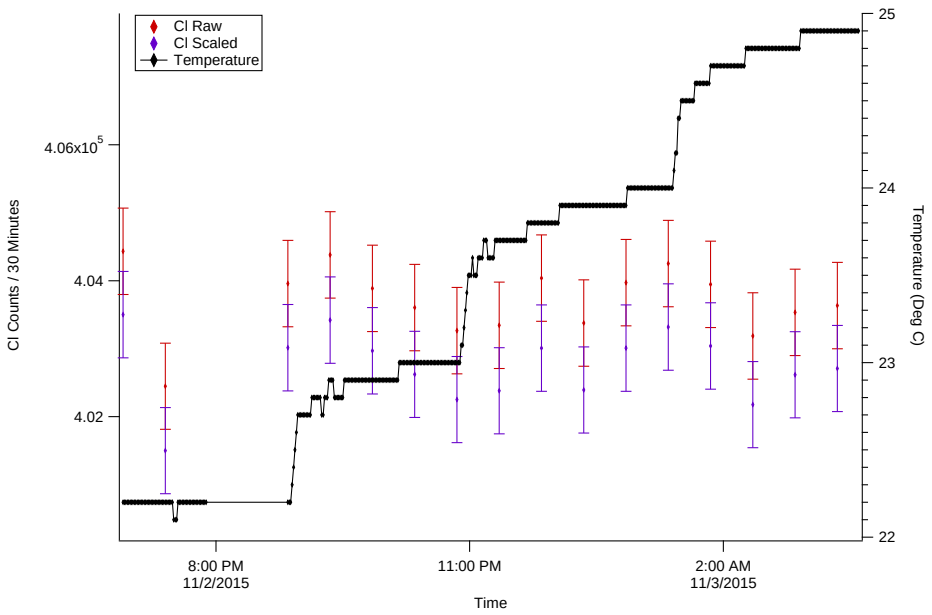

Figure 4.6. 30-minute raw and scaled ^{36}Cl counts while changing the temperature of the detector and NIM bin electronics.

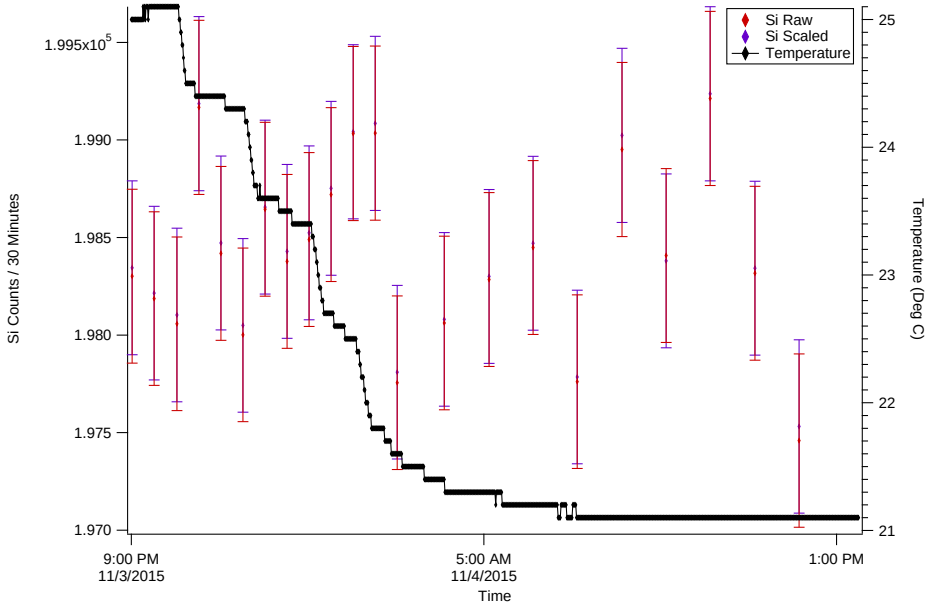

Figure 4.7. 30-minute raw and scaled ^{32}Si counts while changing the temperature of the detector and NIM bin electronics.

were collected while bringing them back down. The samples were shuttled back and forth, as usual, while holding the parameters constant, to allow evaluation of the scaling operation at different set points. The asymmetry in increasing and decreasing the temperature is thought to be responsible for the increase in spread in ^{32}Si counts observed, perhaps due to differences in effects of thermal expansion versus contraction of the sample changer. The fact that the spread remains after the measured air temperature in the drum stabilizes leaves open the possibility of variation in sample placement under the detector. In either event, the effect is included in the systematic uncertainty determination, though a longer characterization is planned in the future in order to investigate this further.

4.2.1 Scaling Algorithm

The aforementioned scaling algorithm was developed by V. Barnes, D. Neff, and H. Kaplan. The process evaluates an archetypal spectrum for each isotope and applies the requisite energy scaling to all other spectra in order to correct for gain shifts. In order to establish a standard gain, a set of spectra collected while the gain was stable, are averaged together to produce an archetype ROOT histogram object. Subsequent spectra's histograms are then compared to the archetype and accordion-scaled in energy by computationally minimizing the bin-by-bin differences.

The efficacy of the scaling algorithm can be seen by comparing the scaled and non-scaled data in figures 4.4 - 4.7. The relationship between the computed scaling parameters and the detector voltage is also shown in Figure 4.8. It is clear that the scaling parameters track the detector voltage, as expected.

4.3 Counting Procedure

The ^{32}Si and ^{36}Cl samples were placed on symmetric, micrometer-adjustable source holders in the sample changer and positioned 2.00 mm $\pm$0.02mm from the face of the detector and locked in place. A piston driven with nitrogen gas moves

the desired source into place under the detector automatically when requested by the DAQ software, and once the sample is confirmed to be in position by a sensor, an 1800 s live-time collection of the energy spectrum begins. The nitrogen exhaust generated from changing samples is piped out of the drum, avoiding fluctuations due to sample changing. Each run of 200 cycles is book-ended by 30 minute collection of background activities (see Figure 4.9), which are nominally less than 2.0 cps, with a variation of less than 0.3 cps. This is slightly lower than the level observed in the BNL experiment ($\sim$ 6.5 cps) in the two background measurements they took – one preceding the experiment and one at its conclusion – even when accounting for the differences in count rate of their samples. The variation in Bg activity during the BNL experiment is unknown.

4.4 Half-life Determination

The following analysis proceeds without background subtraction for comparison to the BNL observations, but it is followed by a separate analysis showing the effect of background removal. Between June 2013 and June 2015, more than 3×10^9 ^{32}Si decays and 6×10^9 ^{36}Cl decays were recorded. These data provide good statistics for determining the half-life of ^{32}Si despite the relatively short observation time, compared to its half-life. As previously noted, each sample was observed in an alternating fashion, such that the data points for ^{36}Cl and ^{32}Si are interwoven. This procedure helps ensure that systematic effects are not preferentially affecting one sample, as might occur if one were to observe each sample for days or weeks at a time. In determining the half-life of ^{32}Si, the ratio of ^{32}Si/^{36}Cl is analyzed so as to suppress such systematic effects. What results should yield an accurate half-life for ^{32}Si, as the half-life of ^{36}Cl ($T_{1/2,Cl} \approx 300,000$ yr) is very long compared to the length of the experiment (i.e. the slope of the ^{36}Cl data is expected to be zero).

In the following analysis on the half-life of ^{32}Si, systematic errors are determined from the characterization data previously presented. Although the scaling algorithm

was shown to mitigate the effects due to gain shifts to within the statistical error bars, we quote the contribution of HV to systematic uncertainty as equal to the size of the statistical uncertainty of each datum. The increased spread observed in the ^{32}Si characterization data, during and after the temperature changes, motivates an additional increase of $1\sigma_{statistical}$ in reported systematic uncertainty. A longer characterization in the future may allow this to be reduced.

Due to low stability in the first two months of collection, (during which adjustments were still being made to the experimental setup), these data were removed from the analysis, yielding a start date of August 9, 2013. Additionally, an unexplained month-long increase in ^{36}Cl counts between February and March 2014 resulted in a small but significant decrease in ratio data. This was also removed in order to ensure that the half-life determination is as accurate as possible. A handful of outliers generated from days on which only one or a few 30-minute cycles took place (usually due to technical issues) were excluded as well.

The remaining data (Figure 4.10) were averaged over one-day intervals, assigned uncertainties, and the ratio fit to an exponential function:

$$f(t) = Ae^{-\lambda t} \tag{4.1}$$

where A is the amplitude, λ is the decay constant, and t is time. The fitting procedure weights a datum by the associated uncertainty and utilizes the Levenberg - Marquardt algorithm, which minimizes χ^2, defined by,

$$\chi^2 = \sum_{i=1}^{N} \frac{1}{\delta M_i^2} \left[M_i - f\left(t_i; A, \lambda\right)\right]^2 \tag{4.2}$$

where N is the number of data points, M_i is the i^{th} datum, t_i, is the time associated with the i^{th} datum, A is the amplitude, and λ is the decay constant.

As noted above, only the spectra collected on a given calendar day were averaged together; days on which a run was started or ended, for example, do not contain 24 hours worth of data collection. The best fit exponential yields $T_{1/2}$ = 162.2 yr ± 1.8 yr (statistical) ± 3.5 yr (systematic) with χ^2_{DOF} = 1.02, where χ^2_{DOF} is χ^2 per

degree of freedom. The residuals of the purely-exponential fit are plotted in Figure 4.11 and fitted to a cosine function, while the histogram of the residuals is shown in Figure 4.12. The period of this cosine fit was then input as the expected period in a combined exponential+cosine fit (equation 4.3) to the non-Bg-corrected ratio decay data, in order to remove the effect of the oscillatory behavior on the half-life determination (see Figure 4.13).

$$F(t) = Ae^{(-\lambda t)}(1 + Bcos(\omega t + \phi)) \tag{4.3}$$

This fit yielded a half-life of 160.3 yr ± 1.9 yr (statistical) ± 3.7 yr (systematic) with a period of 1.13 ± 0.23 yr and $\chi^2_{DOF} = 0.96$. The residuals of this fit are plotted in Figure 4.14, and the histogram is shown in Figure 4.15.

We note that forcing the period to 1 yr improved χ^2_{DOF} slightly as well as the distribution of residuals as seen in Figure 4.16. In iterating this observation, the phase resulting from the forced fit was then held constant, while allowing the period to once again be free, resulting in a further improvement to the distribution of residuals, as seen in figures 4.17 and 4.18. Under these conditions, the resulting period was 1.03 ± 0.03 yr.

The combined exponential+cosine function is important to consider, as a cyclic signal (of any origin) of non-integer periods present in the data will affect the half-life determination. In the case at hand, the non-Bg-corrected data are found to fit best to a sinusoidal curve whose period (1.13 ± 0.23 yr), indicates that it has not returned to its minimum at t_{final}. The effect of excluding this behavior from the fit, is an artificially long half-life, and we indeed see the purely-exponential function yields a half-life $\sim$ 2 yr longer than the combined exponential+cosine function.

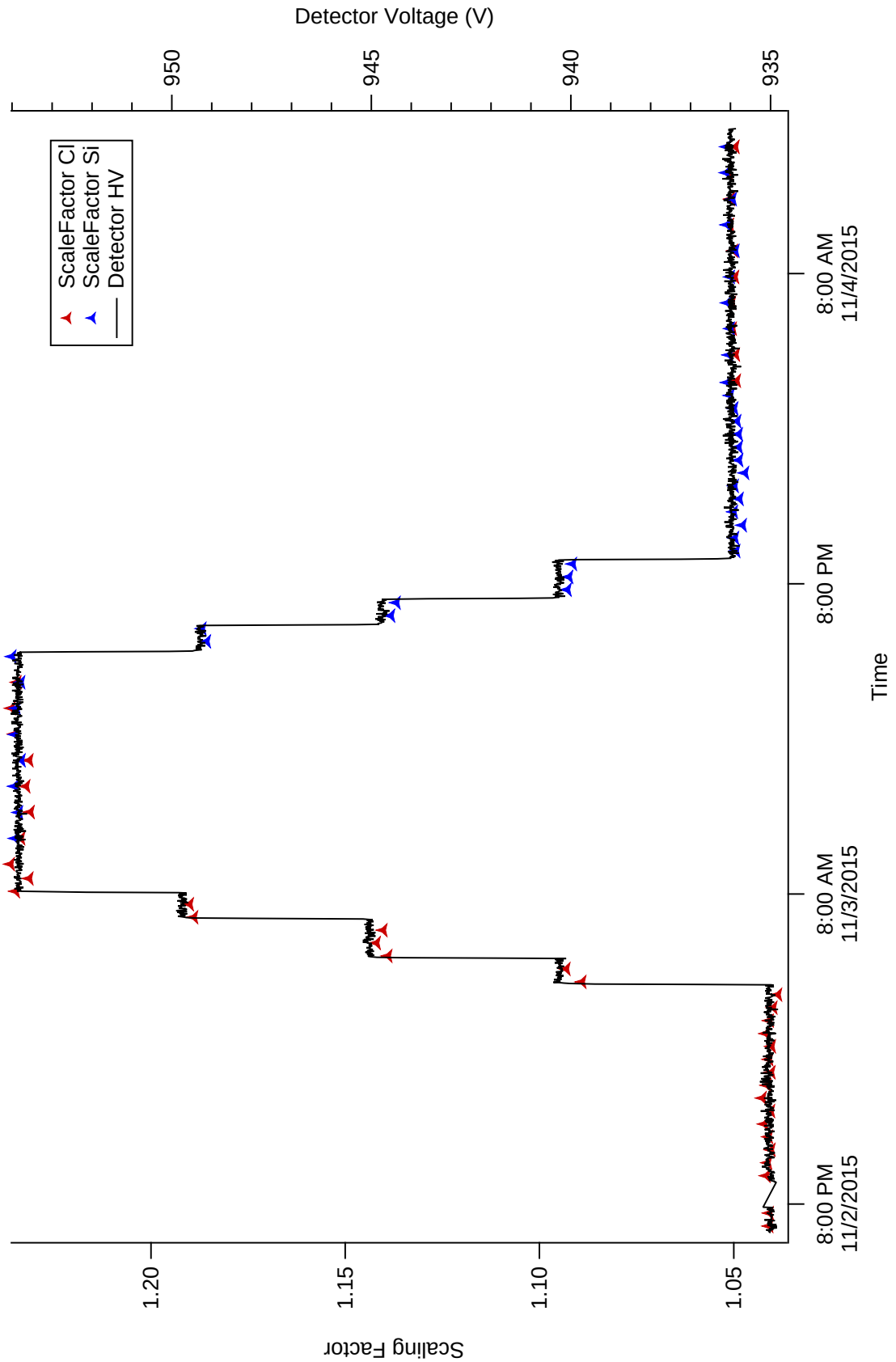

Figure 4.8. Computed scaling parameters overlayed on the recorded detector voltage during characterization.

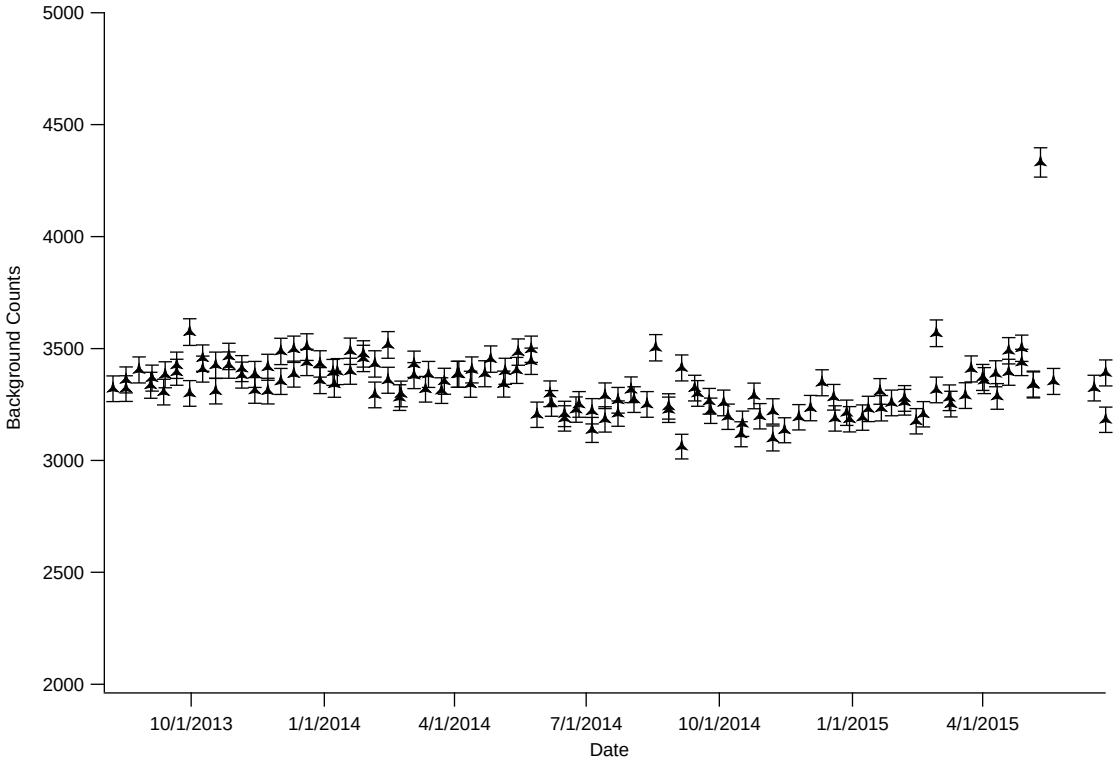

Figure 4.9. 30-minute periods of background activity over the course of the experiment show minor variation of approximately a few hundred counts over the course of the experiment. The shift in nominal activity represents a forced decrease in the HV supply. The outlier was recorded on May 11, 2015.

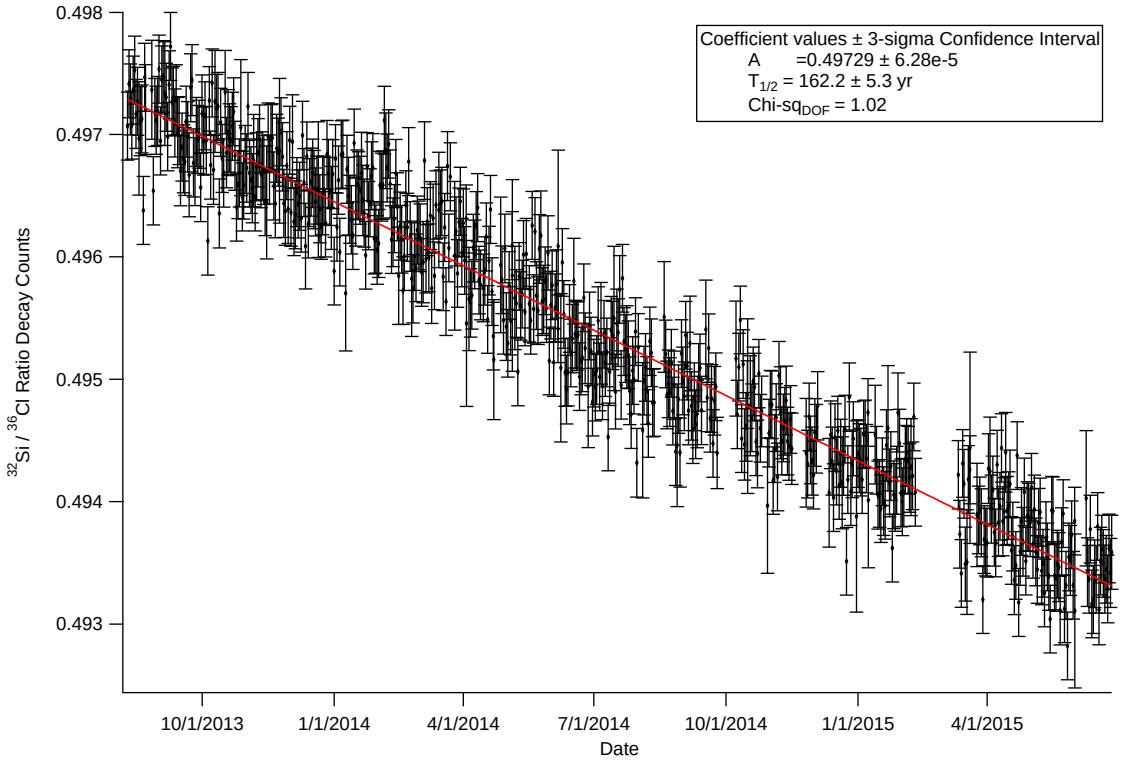

Figure 4.10. Ratio of non-Bg-corrected ^{32}Si to ^{36}Cl data fit to a pure exponential function.

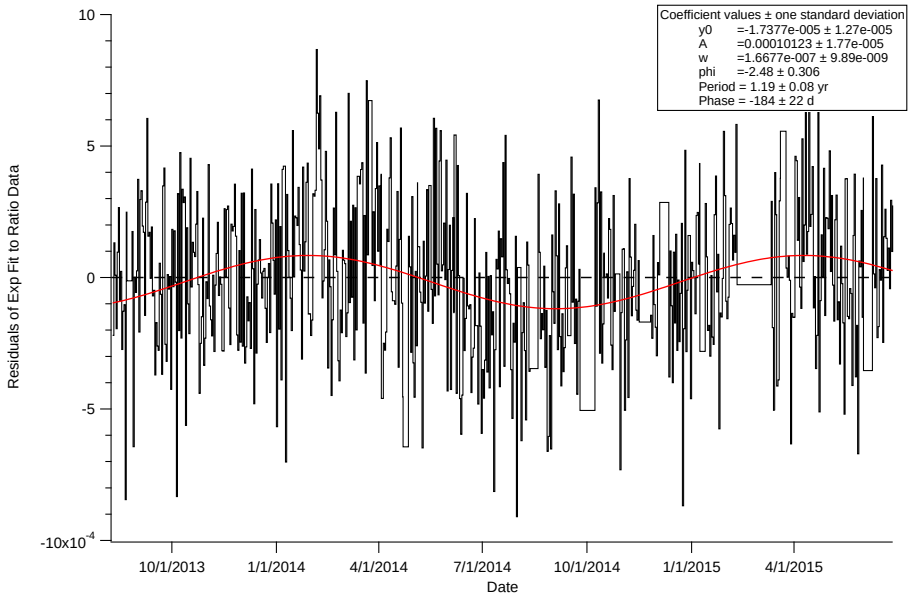

Figure 4.11. Residuals of pure exponential fit to ratio decay data show an oscillatory behavior. The best-fit cosine is included, exhibiting a 1.19 yr period.

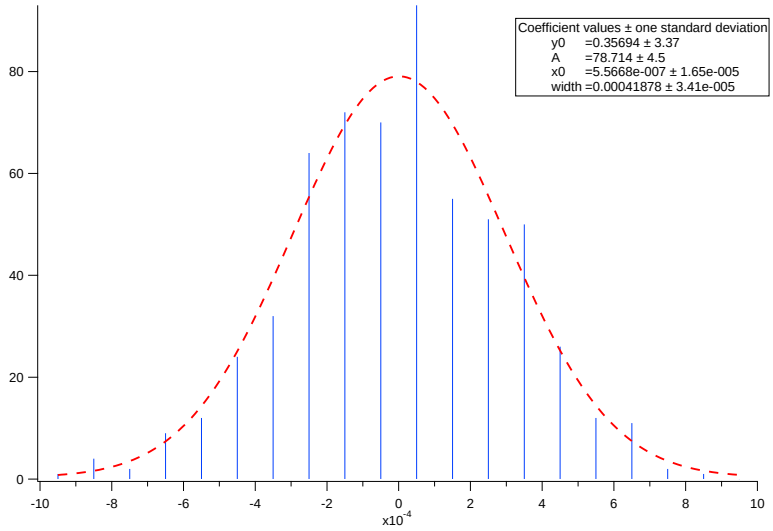

Figure 4.12. Histogram of residuals of the exponential-only fit to the non-Bg-corrected ratio decay data.

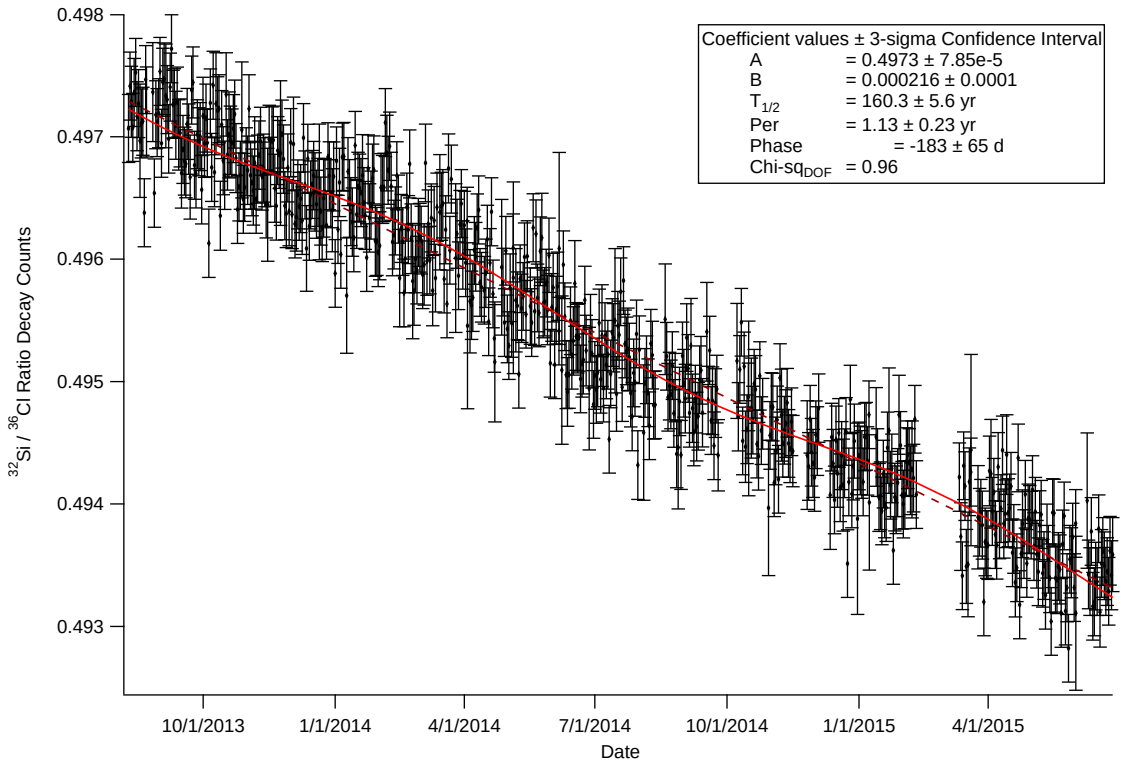

Figure 4.13. Combined exponential+cosine fit to the non-Bg-corrected ratio decay data. The fit yielded a half-life of 160.3 ± 1.9 yr (statistical) ± 3.7 yr (systematic), with a period of 1.13 ± 0.23 yr. The period and phase determined from the cosine fit in Figure 4.11 were input as initial values in this fit.

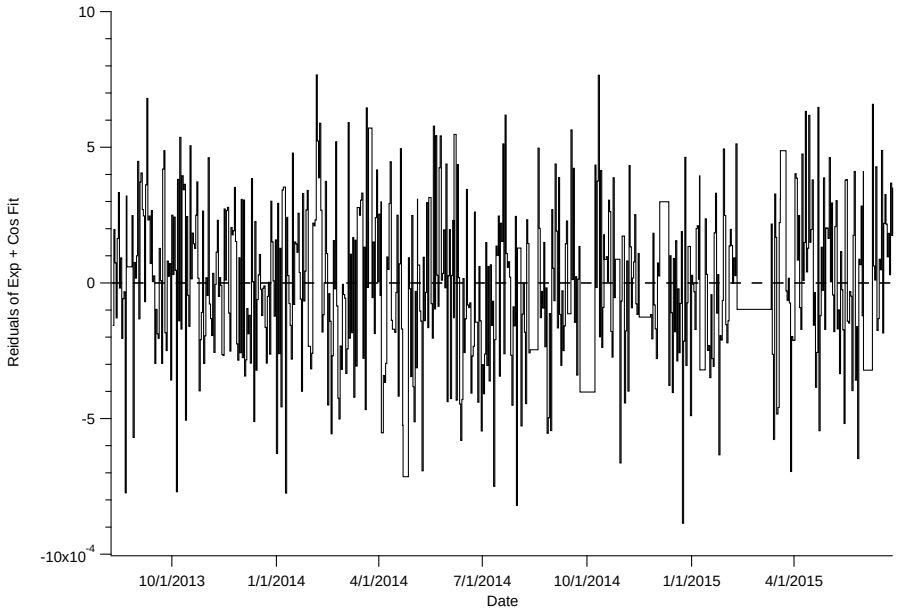

Figure 4.14. Residuals of the combined exponential+cosine fit to the non-Bg-corrected ratio decay data.

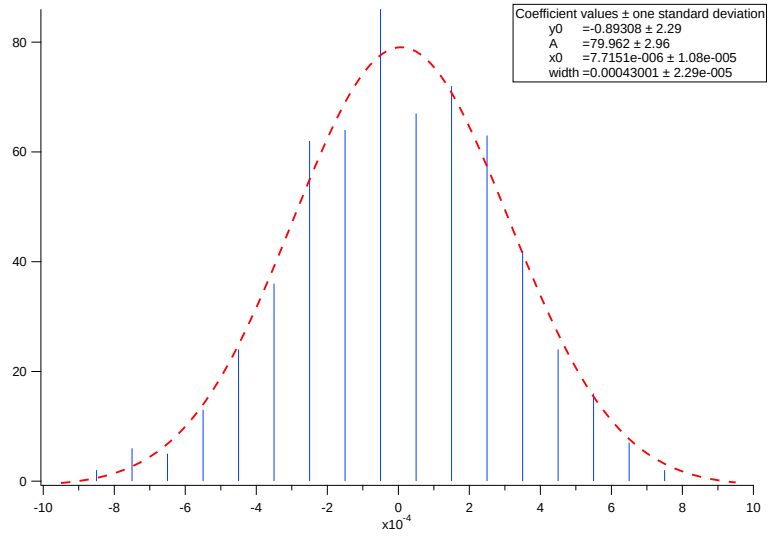

Figure 4.15. Histogram of residuals of the combined exponential+cosine fit to the non-Bg-corrected ratio decay data.

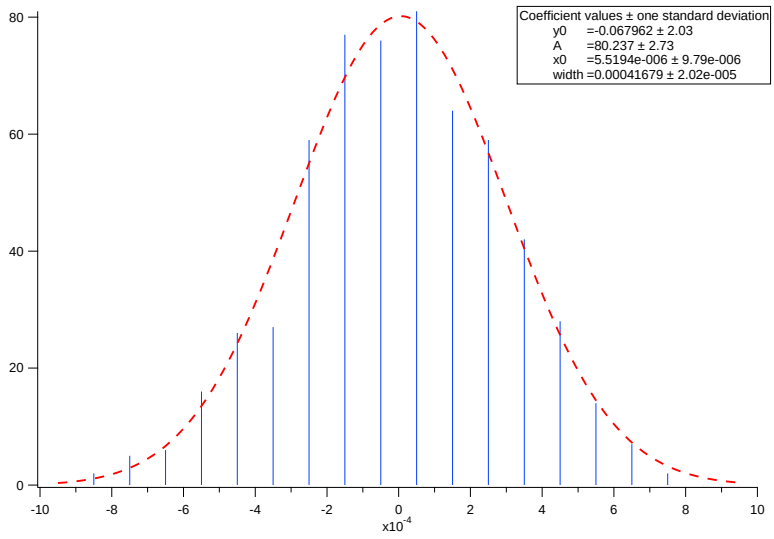

Figure 4.16. Histogram of residuals of the combined exponential+cosine fit to the non-Bg-corrected ratio decay data, forcing period to 1 yr, which improved the distribution.

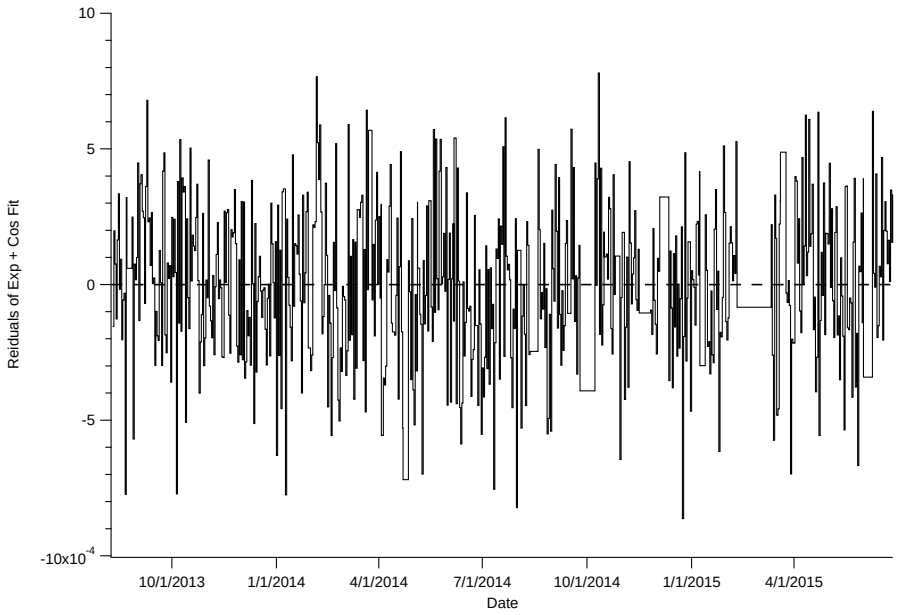

Figure 4.17. Residuals of the combined exponential+cosine fit to the non-Bg-corrected ratio data, holding the phase at previously determined 1-year-period value.

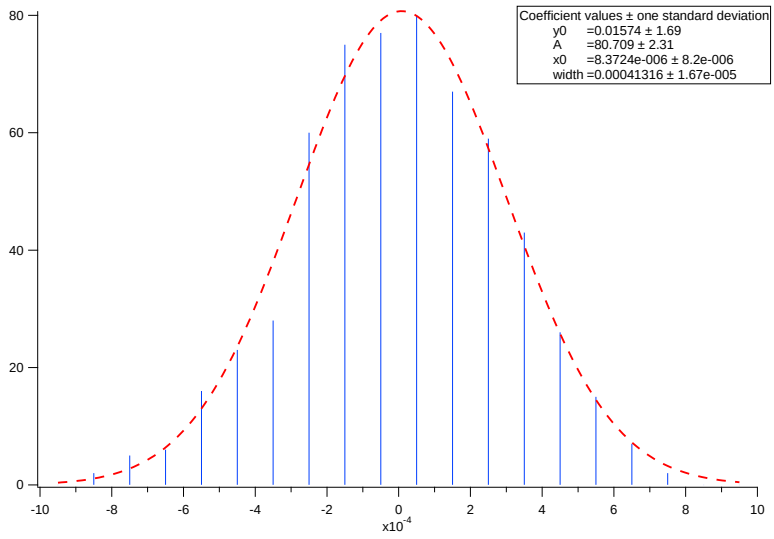

Figure 4.18. Histogram of residuals of the combined exponential+cosine fit to the non-bg-corrected ratio decay data, holding *phase* at previously determined 1-year-period value.

4.5 Variation in Decay Rate

An additional aim of this experiment was to investigate the variation in decay rate observed in the original experiment at BNL. As previously noted, the residuals of the exponential fit to the daily mean non-Bg-corrected ratio (Figure 4.11), exhibit a periodic variation with an amplitude of approximately 1×10^{-4}. A power spectrum analysis by Peter Sturrock on ^{32}Si yields the most significant frequency at 0.93 yr^{-1} (see Figure 4.19), whereas ^{36}Cl shows no 1 yr^{-1} frequency (see Figure 4.20). The power spectrum of the ^{32}Si/^{36}Cl ratio data exhibits a primary frequency at 0.86 yr^{-1} (Figure 4.21. It is also worth noting that his analysis showed the standard deviation of the NH data to be approximately 1/3 that found in his analysis of the BNL data.

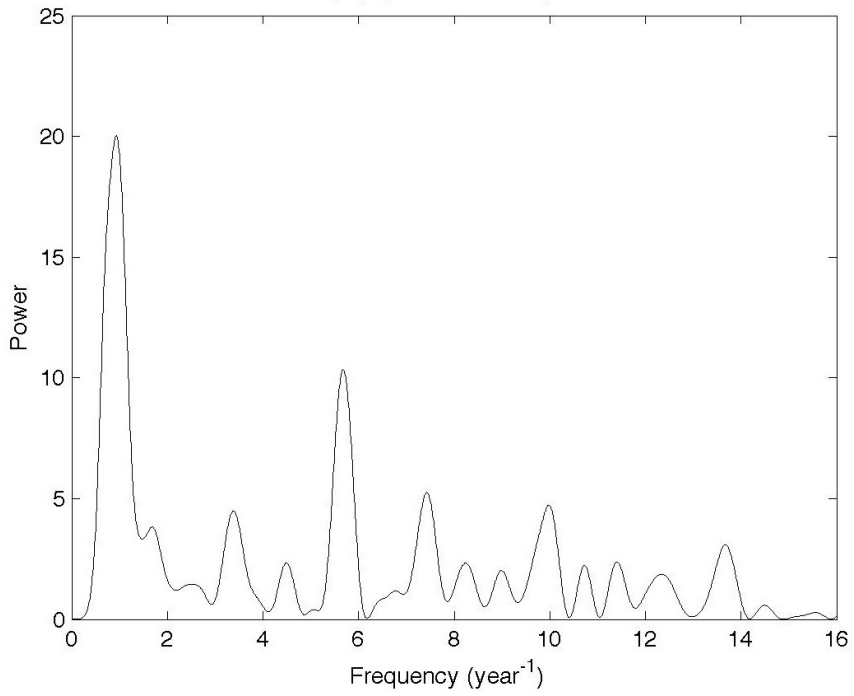

Figure 4.19. A power spectrum analysis of ^{32}Si shows the most significant frequency at 0.93 yr^{-1}.

Data were collected for temperature, pressure, relative humidity, magnetic field, line voltage, and high voltage over the course of the experiment. Each parameter was

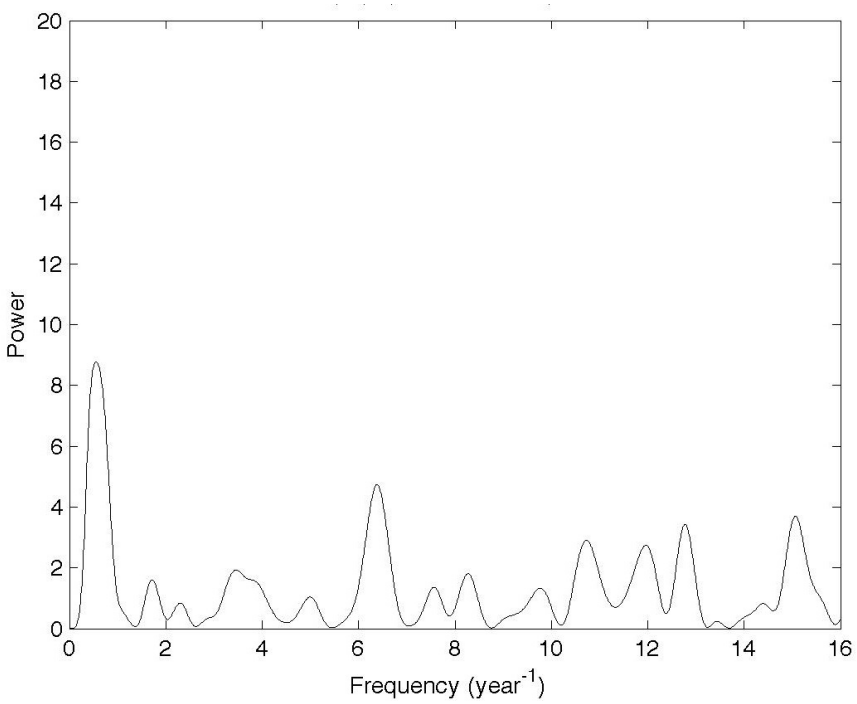

Figure 4.20. A power spectrum analysis of ^{36}Cl is absent of the strong 1 yr periodic signal seen in ^{32}Si. The leftmost peak is located at 0.55 yr^{-1}.

recorded at one-minute intervals and averaged to match the analysis of the decay data (see Figure 4.22. The variation in daily average temperature is typically less than $\pm 2\,^{\circ}$C. The recorded pressure data show excellent stability, stable to a few tenths of an hPa, apart from a few larger deviations due to infrequent hardware issues. Similarly, the %RH was stable to better than $\pm 1\%$ at almost all times. Typical variations in the observed magnetic field during normal data acquisition were less than 10 mG (Figure 4.23). We witnessed an apparent shift in the baseline magnitude on the order of 50 mG, but the change was primarily in the the longitudinal components, whereas the axial component (relative to the detector) was shown to be the most significant to detector behavior. Even if the aforementioned change in the magnetic field had been along the detector axis, it is still twenty times below the 2 Gauss level, shown to be a safe region of operation. Given the step-wise nature of this change, it is likely

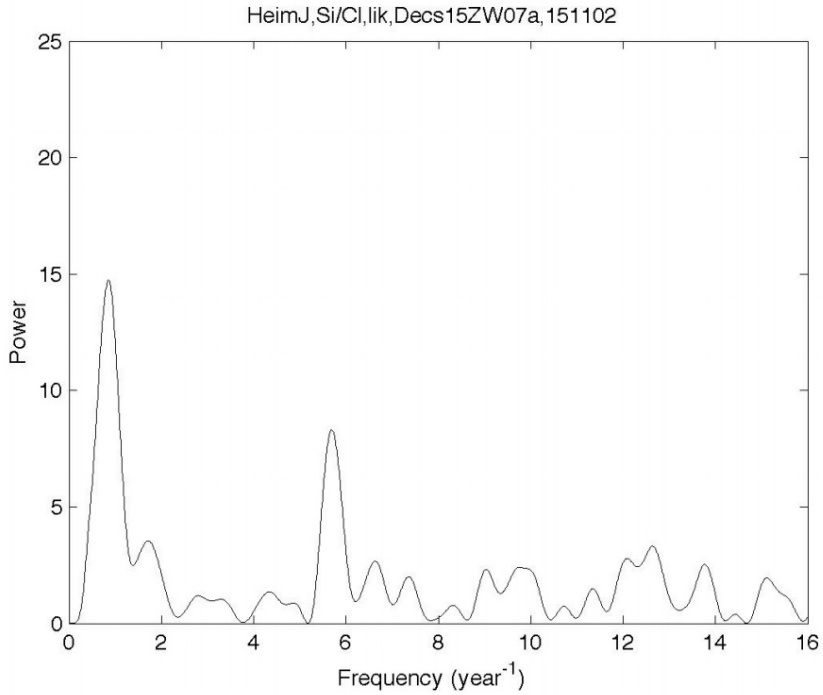

Figure 4.21. Power spectrum of $^{32}Si/^{36}Cl$ exhibits a primary frequency of 0.86 yr^{-1}.

that other equipment in the room was moved or that the sensor shifted, physically. The line voltage varied between 115 and 119 V, which falls well within the bounds of stability shown by our characterization of the system, discussed earlier. The high voltage was seen to vary between 950 V and 955 V before we lowered the set point, and typically between 935 V and 940 V after. As previously discussed, we applied a scaling algorithm in an attempt to correct for these variations.

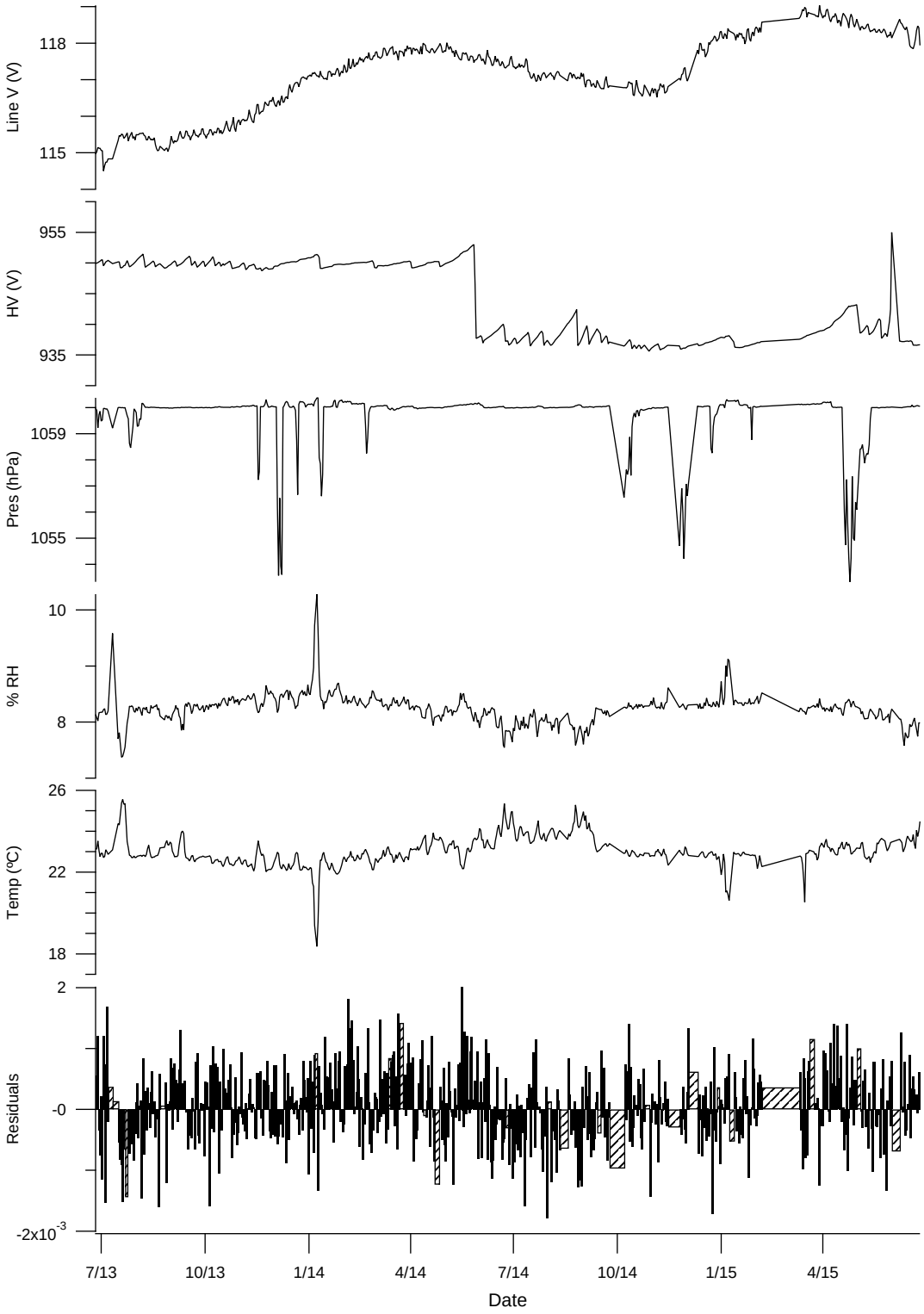

Figure 4.22. Daily mean values of decay ratio residuals and environmental observations. Approximately 5×10^6 environmental readings have been logged collectively.

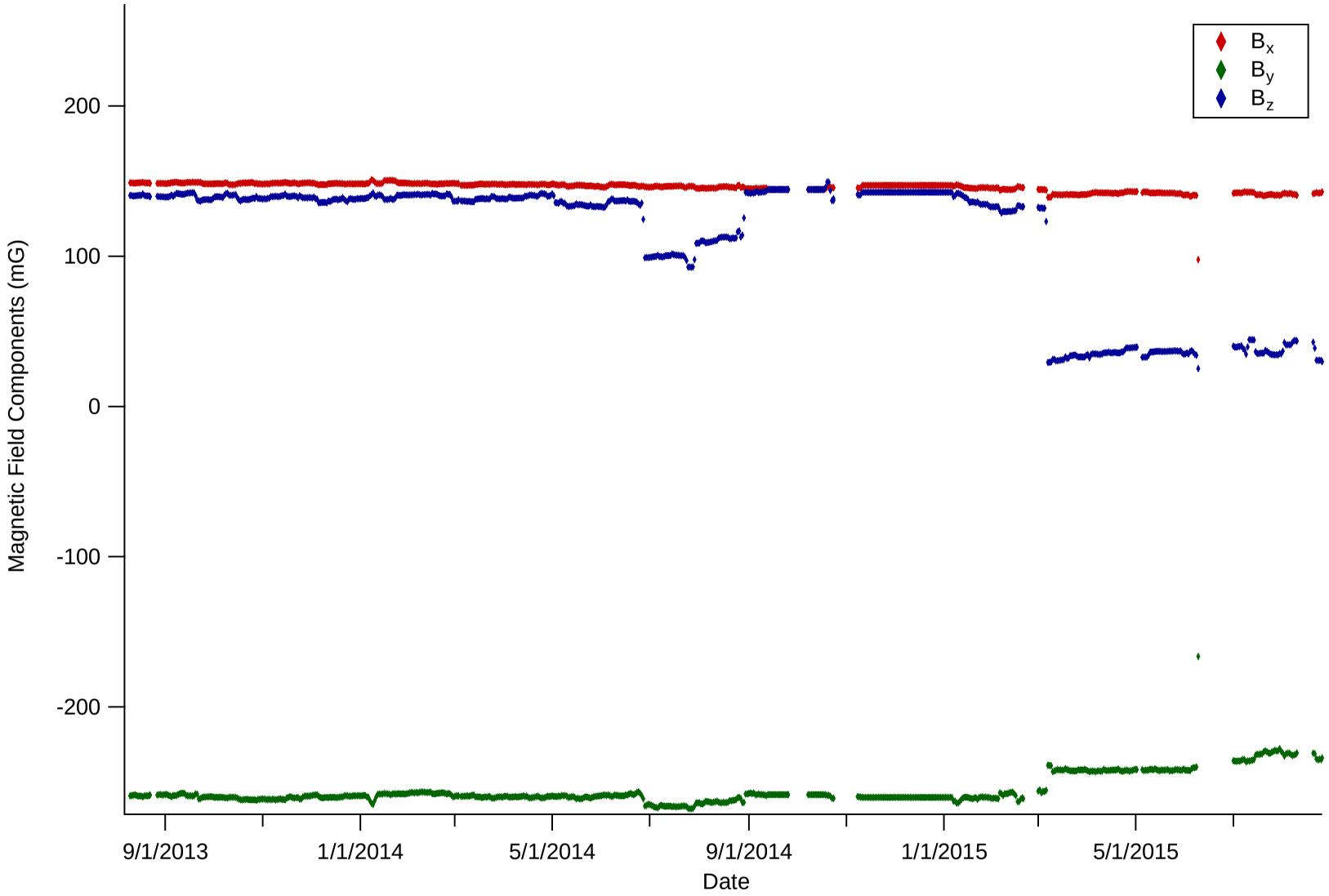

Figure 4.23. Daily mean values of observed magnetic field components. B_x is oriented along the axis of the detector.

4.6 Correlation

IBM's SPSS statistical software package was utilized in quantifying the correlation between decay data and environmental parameters. A multiple linear regression was performed on the data set consisting of nearly 600 daily-mean data points contained in each of the parameters. Since the ^{32}Si/^{36}Cl ratio exhibits a natural trend over time, due to ^{32}Si's shorter half-life, the fractional residuals of the exponential fit to the ratio data were used in this analysis. The regression yielded a weak, negative correlation to temperature, with a Pearson value of -0.15, while the detector voltage showed a weak (but positive) correlation of 0.16. Finally, the correlation to $1/R^2_{ES}$ was 0.11. Due to the strong collinearity between temperature and %RH, the latter was not included in the correlation analysis; it's correlation to ratio decay data was seen to be essentially the opposite of temperature, as expected. Table 4.2 shows the correlation values between the decay data and environmental parameters.

Modeling the simultaneous behavior of all parameters, yielded a global Pearson correlation of 0.229 for an R^2 of 0.052. The three most important predictors of the resulting model were reported to be HV, temperature, and $1/R^2_{ES}$, in decreasing order. It is no surprise that the detector voltage is the most significant predictor. If anything, the weak Pearson correlation coefficient assigned to HV speaks to the efficacy of the scaling algorithm in correcting for gain shifts. Further, given the effect temperature was shown to have on the HV supply, and the relationship between temperature and $1/R^2_{ES}$, these results are not particularly enlightening on their own.

A rolling correlation was performed between a given set of data (ratio residuals, for example) and the remaining parameters. That is, the correlation was evaluated for each iterated offset (in days) of the given set to static sets of the other parameters. First, we consider the correlations produced by rolling $1/R^2_{ES}$, as this is both of interest to our research, and relatively easy to interpret. In Figure 4.24, we see that the magnitude of correlation between $1/R^2_{ES}$ and temperature is maximal (and negative) for a phase of zero. One may also note that the correlation between line voltage

and $1/R_{ES}^2$ is large, but with a significant phase shift. Line voltage understandably exhibits a yearly periodicity, in which case it will certainly correlate strongly to some set of shifted $1/R_{ES}^2$ data. The phase for maximal correlation of high voltage to $1/R_{ES}^2$ is zero, most likely exhibiting the effect of temperature on the HV supply. We note a non-zero phase for maximal correlation to the ratio decay data, which is interesting for two reasons. The first is that effects due to detector voltage are expected to produce a signal in phase with the HV supply as well as the temperature, due to the former's response to the latter. The second reason this observation is interesting is that similar phases in decay data have been previously reported [41].

Further analysis by means of a rolling correlation of the individual ^{32}Si and ^{36}Cl decay data, as opposed to the ratio data, yields disparate behavior in terms of phase for maximal correlation (see Figure 4.25) to $1/R_{ES}^2$, resulting in the phase shift of the ratio. From our characterization of the DAQ system, it was determined that a larger detector voltage increases the observed counts of ^{36}Cl, while decreasing those of ^{32}Si. The resulting ^{32}Si/^{36}Cl ratio must then decrease for an increase in detector voltage. However, we also found that heating the HV supply resulted in a decrease in voltage, indicating that the effect of seasonal temperature fluctuations should work to increase the ^{32}Si/^{36}Cl ratio in the summer and decrease it in the winter. Our decay data, on the other hand, show the opposite behavior.

We now turn to rolling through the index of the ratio decay data residuals, while correlating to the environmental parameters, including $1/R_{ES}^2$. We find, here, that temperature and HV show the largest correlation values for zero shift in date of the residuals data set (see Figure 4.26). Again, we see that the largest correlation to Earth-Sun distance exists for a non-zero shift in index of the residuals.

Finally, we compare the variation in decay rate observed at BNL, with the same samples, to that noted above. In the BNL experiment, Alburger and Harbottle observed a variation in the ratio with a 1 yr period, as shown in Figure 3.2. We fit their ^{32}Si/^{36}Cl ratio decay data to a pure exponential function with the same method utilized in the analysis of our data and plot the residuals for each on the same graph

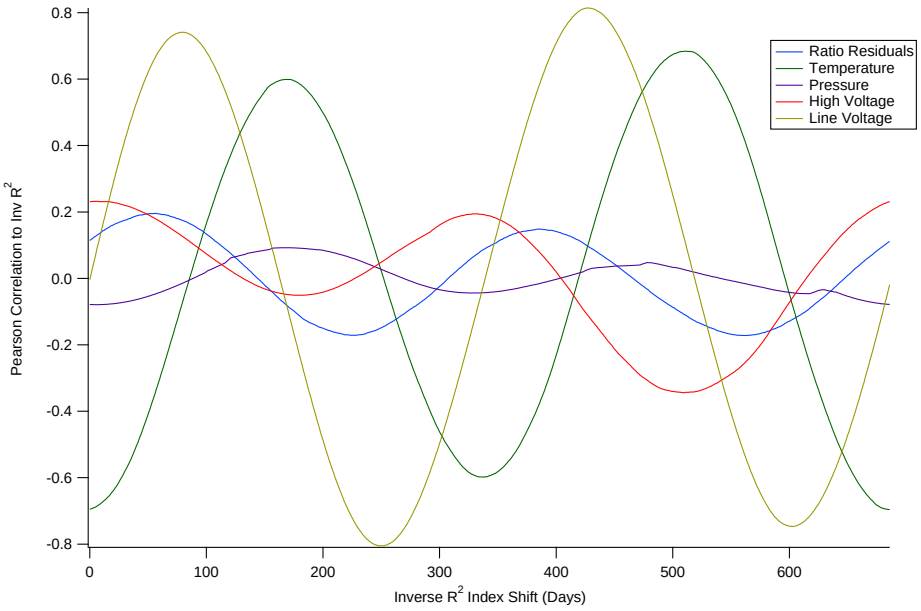

Figure 4.24. Correlation of environmental parameters and ratio residuals with $1/R^2_{ES}$, for each index shift (representing days) of $1/R^2_{ES}$. The effect is to show phase offsets of parameters for maximal correlation to Earth-Sun distance. The x-axis represents number of days shifted for each point along a given curve.

	Residuals	Temperature	Pressure	HV	LV	$1/R^2$
Residuals	1	-0.147	-0.012	0.161	0.052	0.111
Temperature	-0.147	1	0.047	-0.453	0.198	-0.694
Pressure	-0.012	0.047	1	0.082	-0.086	-0.085
HV	0.161	-0.453	0.082	1	-0.447	0.214
LV	0.052	0.198	-0.086	-0.447	1	-0.022
$1/R^2$	0.111	-0.694	-0.085	0.214	-0.022	1

Table 4.2

Table of Pearson Correlation values for environmental parameters and residuals of non-Bg-corrected $^{32}Si/^{36}Cl$ ratio decay data.

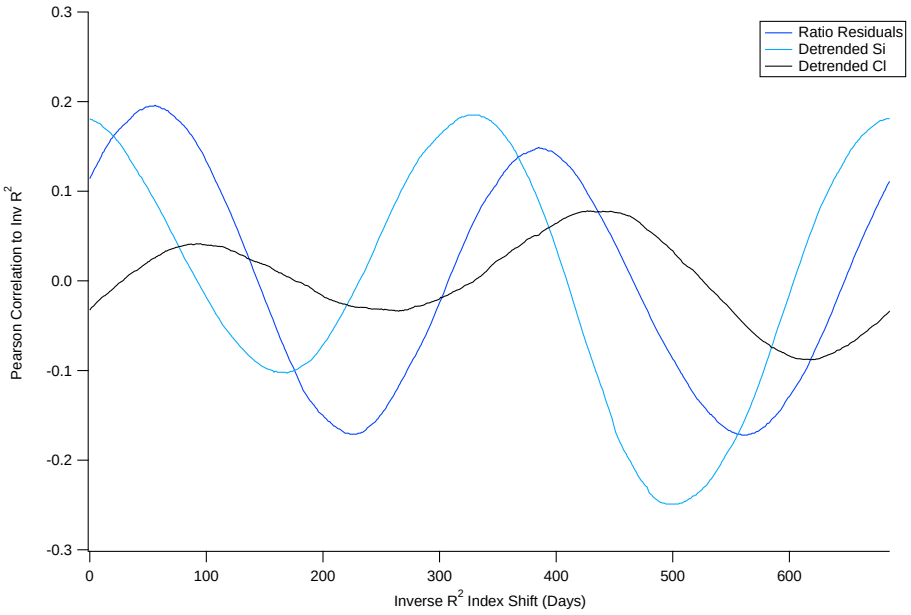

Figure 4.25. Rolling Correlation of decay ratio residuals as well as ^{32}Si and ^{36}Cl data, separately, to $1/R^2_{ES}$ while shifting its index.

(see Figure 4.27). For cleanliness, the NH data are collapsed to monthly mean values, approximating their frequency of data points. Each year of the respective experiment is represented by a different shade of red or blue. In Figure 4.28, the residual values for a given month are further averaged into a single data point for each experiment. The similarity of the observed deviation from the exponential fits is clear. We note that the magnitude of the averaged residuals in the NH experiment is approximately a factor of 4 smaller than those observed in the BNL experiment. This may provide insight as to the cause of the variation; it is assumed that the temperature control is tighter in the NH experiment, but the necessary systematic recordings were not made during the BNL experiment, as this variation was unexpected. It will be interesting to observe the behavior of the residuals with highly stable temperature and HV in future NH data.

We previously argued that the fractional effect of HV on the ^{36}Cl and ^{32}Si data, as well as the ratio data, was smaller than the statistical error bars. Allowing for

systematic effects of the same magnitude as the statistical error bars yields fractional count rate dependencies (on detector voltage) large enough in size to encompass the periodic signal. With that said, however, our data show approximately the opposite phase as would be expected based on the behavior of the data in our characterization studies. One might argue that the scaling algorithm is simply over-correcting the data, yielding this opposing behavior, but analysis of the scaled and unscaled ratio data in Figure 4.8 shows that the ratio of the second half of the data set (represented on the right side of the graph), after scaling remains slightly higher than the scaled data on the left hand side, indicating that the algorithm is not over-correcting this data. The fact that the observed signal is essentially opposite to the characterized temperature-dependent HV effect deserves further investigation.

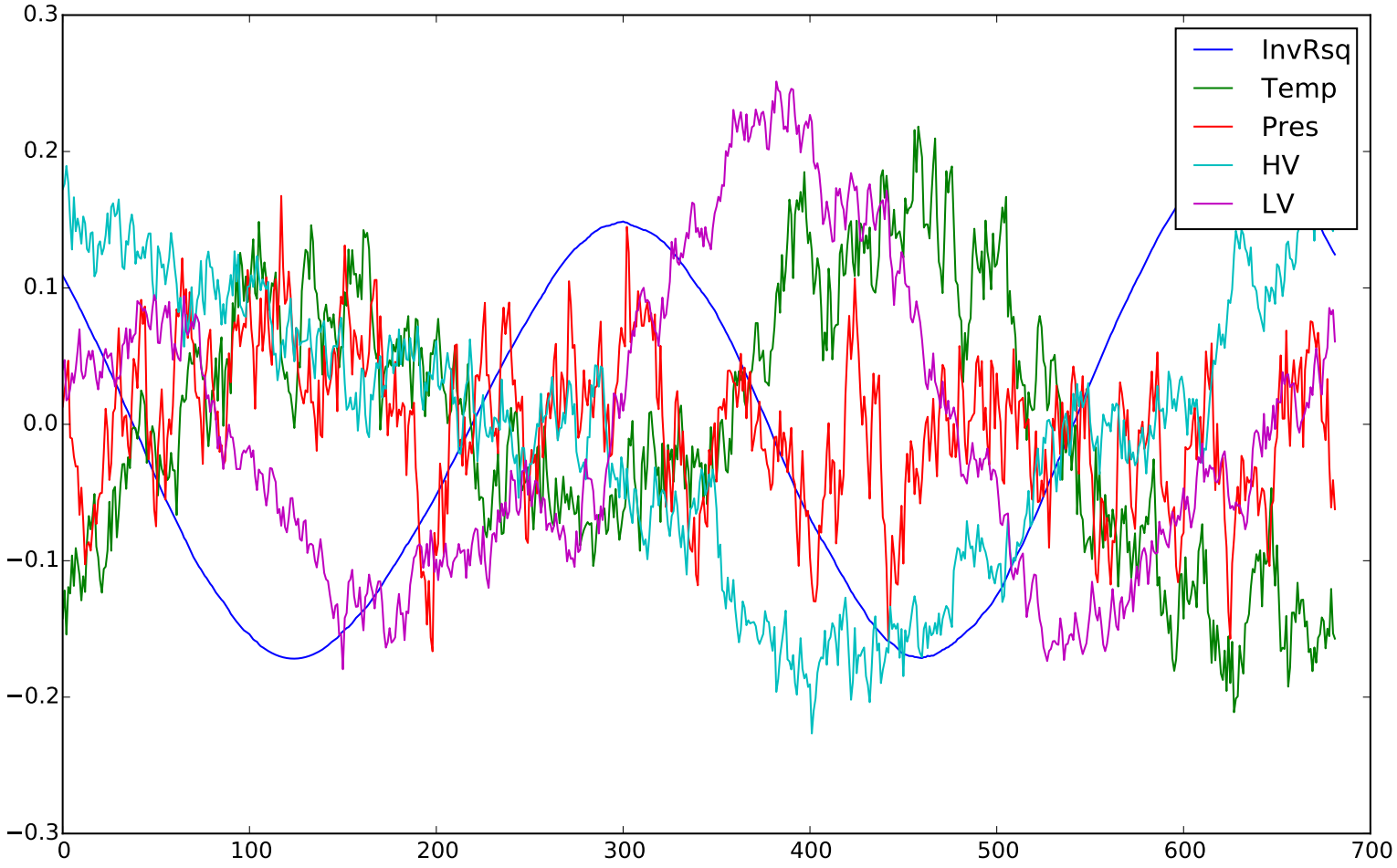

Figure 4.26. Correlation of environmental parameters with decay ratio residuals, while shifting the residuals by day for each correlation value calculation.

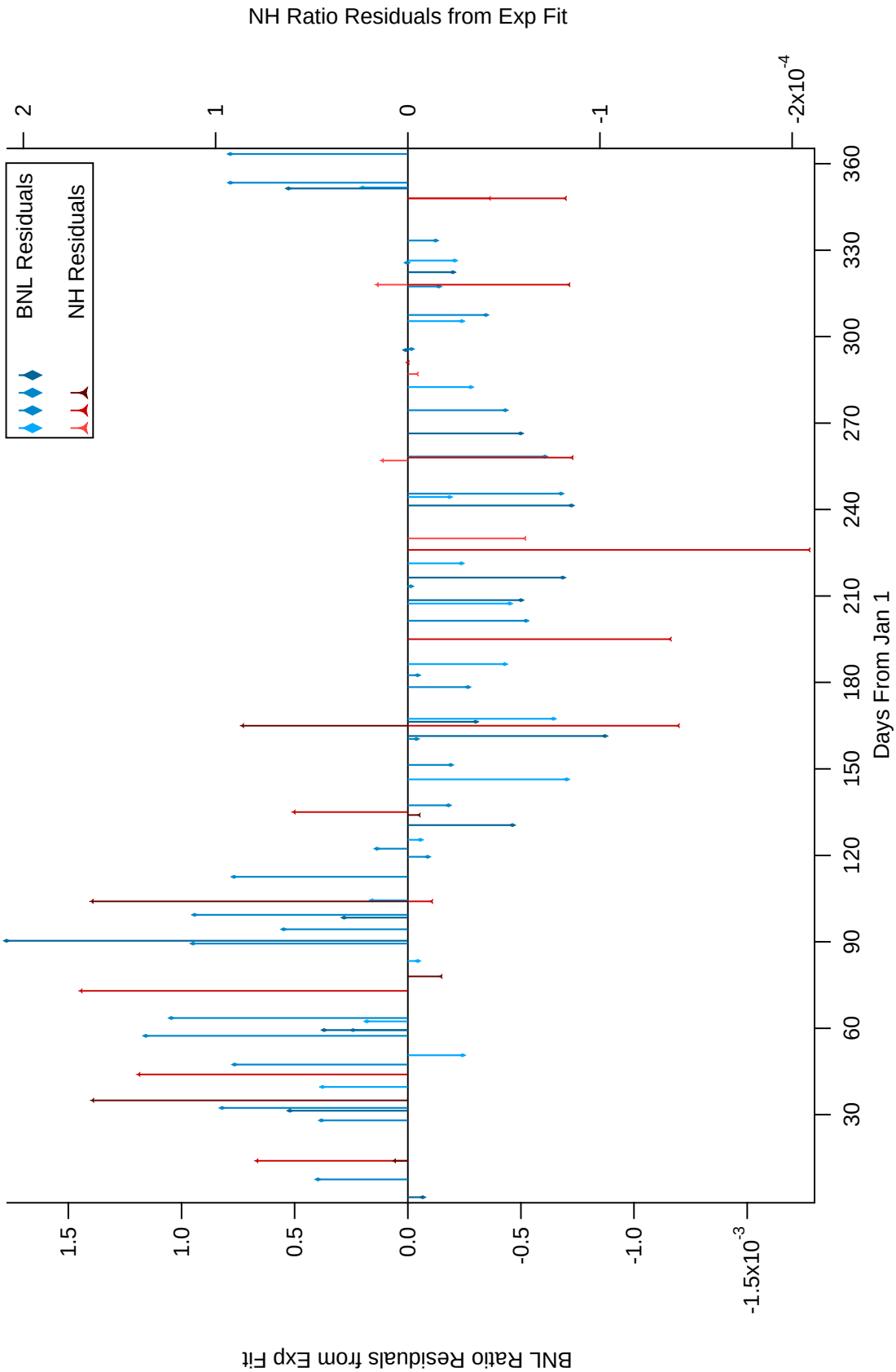

Figure 4.27. Year over year monthly mean values for residuals of $^{32}Si/^{36}Cl$ ratio decay data for the original BNL experiment (blue) and the NH experiment (red). Years are indicated by differing shades of each color.

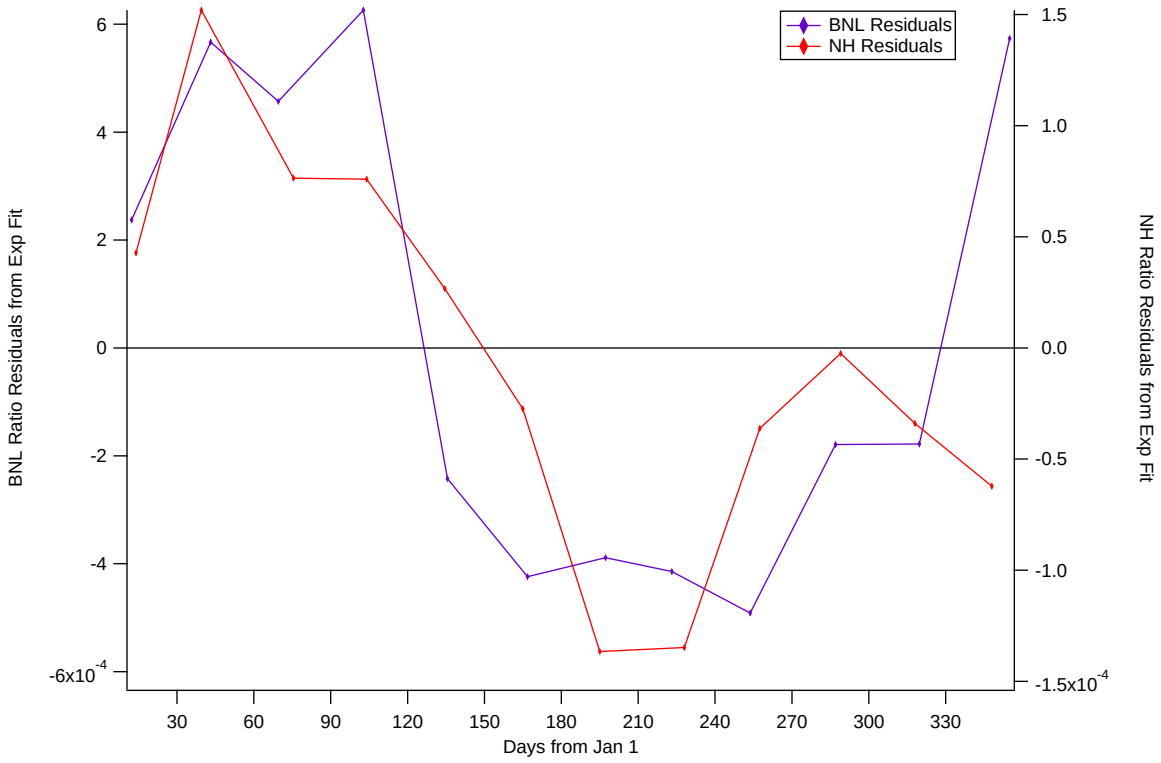

Figure 4.28. Total monthly mean residuals of $^{32}Si/^{36}Cl$ ratio decay data for the original BNL experiment (blue) and the NH experiment (red), irrespective of year.

4.7 Background

As the BNL experiment was solely intended to determine the half-life of ^{32}Si, the relatively low background (Bg) rate was deemed negligible and not recorded over the course of the experiment. Thus, we cannot state the variation in Bg during that experiment. However, based on the amplitude of modulation ($\sim 1 \times 10^{-3}$) observed in the BNL data and the reported count rates of ^{32}Si (247 cps) and ^{36}Cl (358 cps), which are assumed to include the nominal Bg, we can estimate the change in Bg which could cause the modulation by:

$$(1 + A) \times \frac{R_{Si}}{R_{Cl}} = \frac{R_{Si} + \delta R_{Bg}}{R_{Cl} + \delta R_{Bg}} \tag{4.4}$$

where δR_{Bg} is the nominal change in background activity that would cause a modulation amplitude, A. Inserting the reported count rates for ^{32}Si, ^{36}Cl, and A yields:

$$(1 + 1 \times 10^{-3}) \times \frac{247}{358} = \frac{(247 + \delta R_{Bg})\text{cps}}{(358 + \delta R_{Bg})\text{cps}}$$

which results in:

$$\delta R_{Bg} = 0.8\text{cps}$$

as the amplitude of Bg variation required to manifest a modulation of 1×10^{-3} in the ratio decay data.

In the NH experiment, the full-spectrum Bg varied between ∼3000 and ∼3500 counts per 1800 s collection (Figure 4.9), bookending each set of 200 ^{32}Si/^{36}Cl cycles. The decreased stability in background, seen in the latter half of the figure, is suspected to be due to larger drifts in the HV supply, as suggested by Figure 4.29. In order to subtract the Bg activity from the region of integration (ROI) of the decay data, the nearest background observation is interpolated using the determined scaling parameter of each individual ^{32}Si and ^{36}Cl cycle. Although the accordion scaling algorithm greatly reduces effects due to gain shifts, a varying background will not be sufficiently corrected for without removing it independently. We see evidence

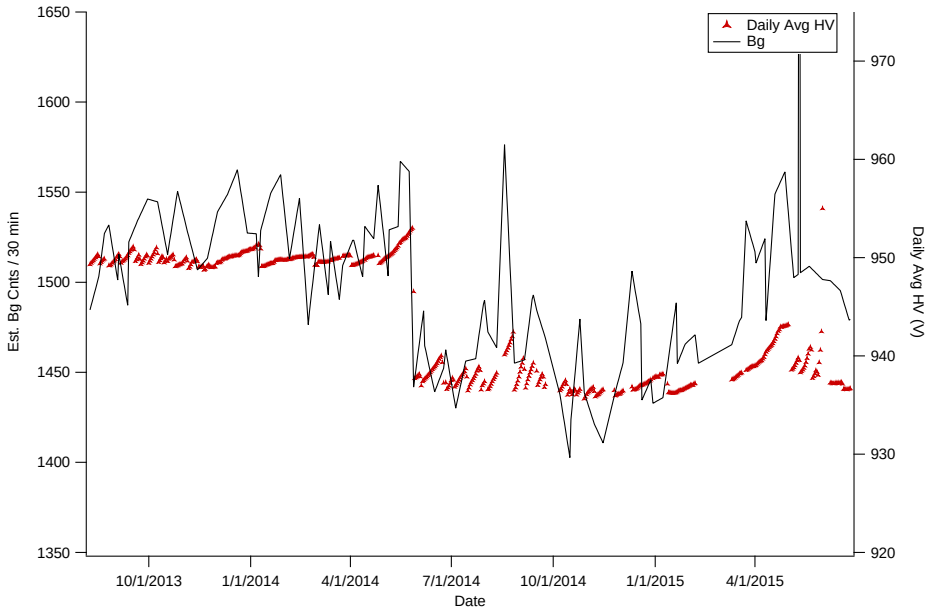

Figure 4.29. Daily average HV records overlayed with *manually estimated* background activity suggests that the variation in the observed background is driven by the detector voltage (HV).

of this in Figure 4.30, which shows the residuals of the exponential fit to the non-Bg-corrected ^{32}Si/^{36}Cl ratio decay data overlayed with *manually estimated* ROI Bg activity. The manual estimate simply multiplied all full-scale Bg data by 0.45, estimating the fraction of counts in the ROI region, and linearly interpolating between adjacent Bg measurements, without referencing the recorded detector voltage. It is certainly compelling enough to require a robust background removal.

In order to determine a reasonable magnitude for the possible effect of the variation of corrected Bg, we average the estimated ROI bg activities between January 1 and April 1, 2014, during which the modulation of the ratio decay data is maximally positive, as well as between July 1 and October 1, 2014, when the modulation is maximally negative. Using the difference in these values, equation 4.4 suggests the contribution of varying Bg is approximately 2×10^{-4}. This is large enough to account for the variation seen in our non-Bg-subtracted ratio decay data, though it

assumes the accordion scaling performed on the data does nothing to suppress the changes in Bg, which is unlikely. It may useful to quantify this suppression by artificially increasing the Bg in a future characterization. We proceed by subtracting the computationally-determined Bg from the ^{32}Si and ^{36}Cl data.

After the background counts in the ROI are determined for each ^{32}Si and ^{36}Cl cycle, individually, they are subtracted, propagating statistical uncertainties. These data are combined into daily mean ^{32}Si/^{36}Cl ratios and fit with a purely exponential function, weighted by total statistical and systematic uncertainties (Figure 4.31. The half-life determination of this fit yields $T_{1/2}$ = 161.8 yr $\pm$ 1.7 yr (statistical) $\pm$ 3.3 yr (systematic) with $\chi^2_{DOF} = 1.07$, which agrees very well with Thomsen's determination [42]. The residuals of this fit and the associated histogram are presented in Figure 4.32 and 4.33, respectively. Comparison to the non-Bg-corrected residuals (Figure 4.11) indicates a marginal decrease in amplitude of approximately 4.5×10^{-6}. The determined period of the cosine fit moved closer to 1 yr, as well, though a

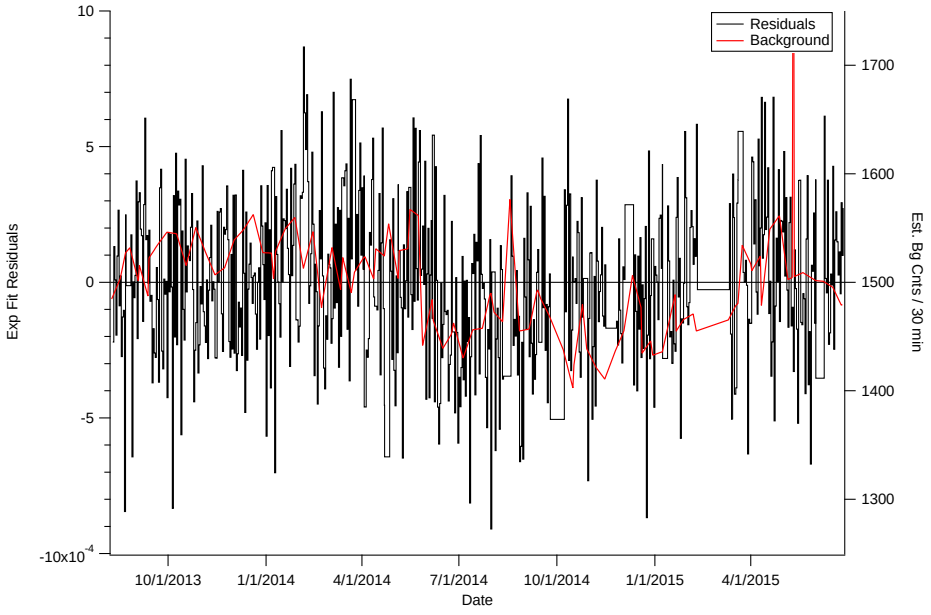

Figure 4.30. Residuals of the earlier exponential fit to non-Bg-corrected ratio data overlayed with *manually estimated* background activity.

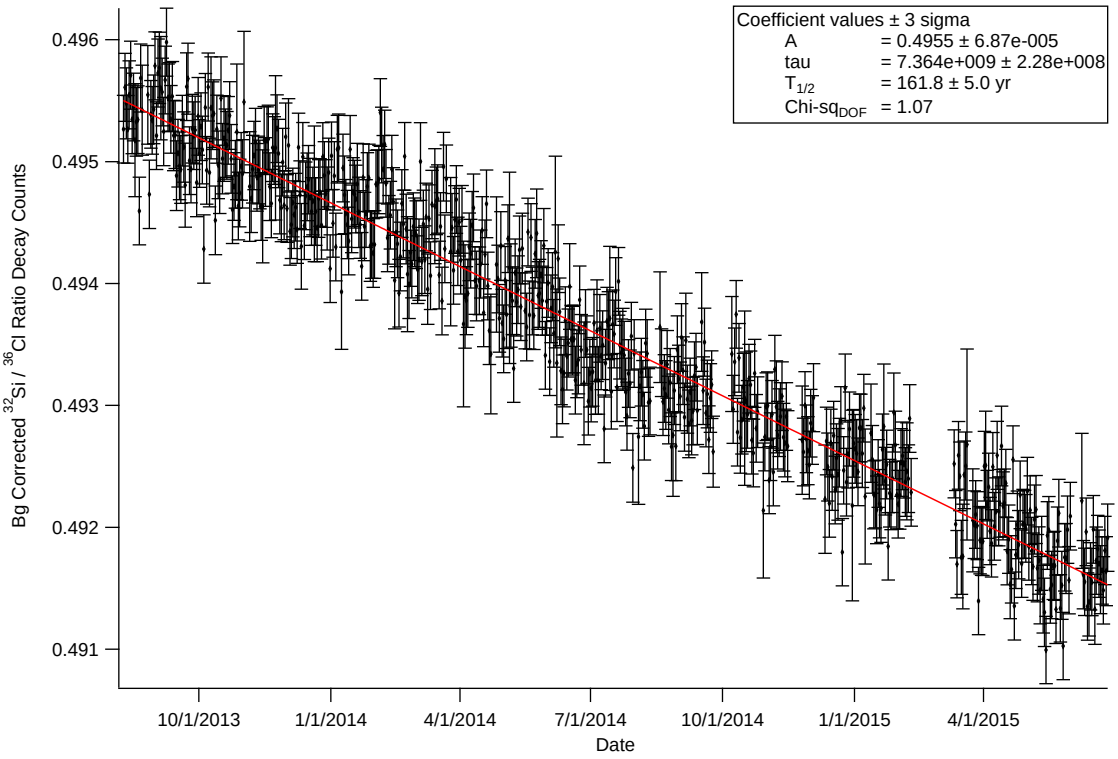

Figure 4.31. Exponential fit to the Bg-corrected ratio decay data yields $T_{1/2}$ = 161.8yr $\pm$ 1.7 yr (statistical) $\pm$ 3.3 yr (systematic) with χ^2_{DOF} = 1.07.

more robust frequency analysis is desired. We note that these results are unexpected after having observed the relationship between the non-Bg-corrected residuals and the estimated Bg activities, as it was presumed that the more robust Bg subtraction would remove the observed modulation. We are scrutinizing the Bg removal procedure to ensure it is effective. Although the initial suggestion (to Igor Pro's iterative fitting process) for the cosine's period was approximately 1 yr, as in the earlier analysis, various initial values above and below this failed to produce any obvious improvement in χ^2_{DOF} and distribution of residuals. Utilizing the period and phase from the cosine fit (Figure 4.32), we once again employ a combined exponential+cosine function (Figure 4.34) with the aim of removing the effect of a

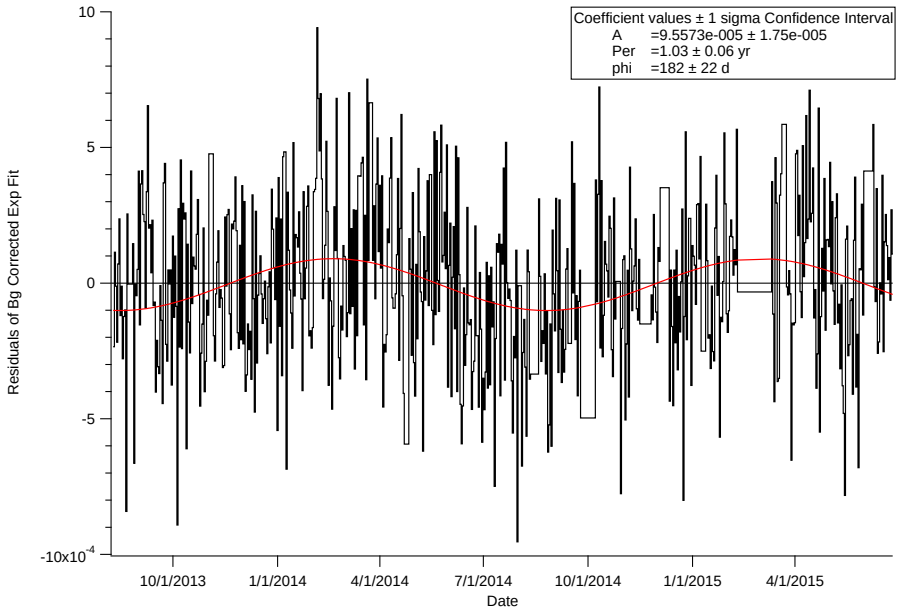

Figure 4.32. Residuals of the purely exponential fit to the Bg-corrected ^{32}Si/^{36}Cl ratio data, fit with a cosine function.

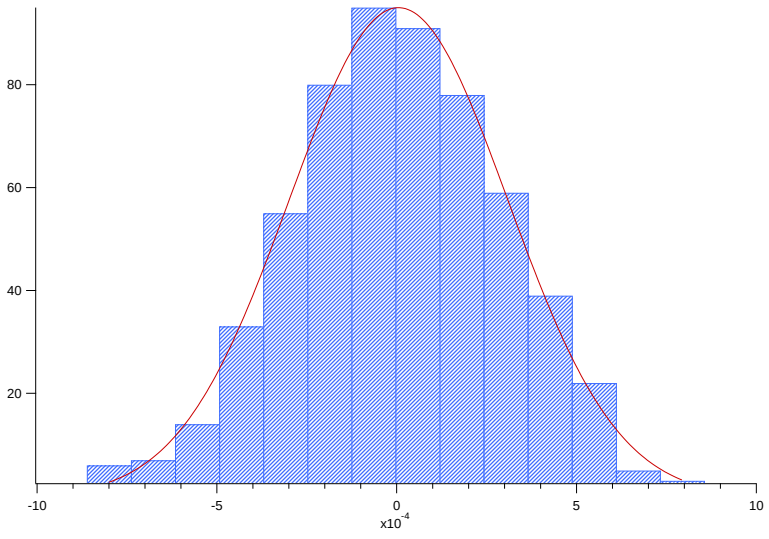

Figure 4.33. Histogram of the residuals of the cosine fit in Figure 4.32.

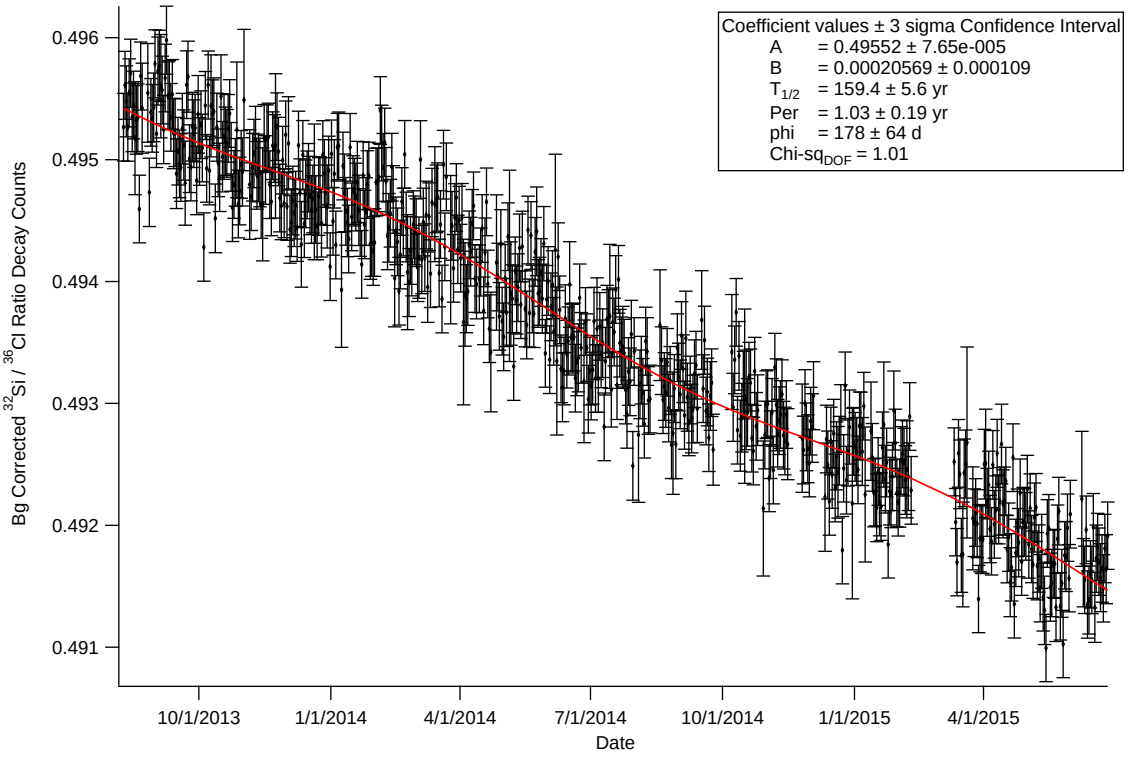

Figure 4.34. The combined exponential+cosine function 4.3 fit to the Bg-corrected ratio decay data yields $T_{1/2}$ = 159.4 yr ± 1.9 yr (statistical) ± 3.7 yr (systematic) with $\chi^2_{DOF} = 1.01$.

non-integer number of oscillatory cycles on the half-life determination. The result is $T_{1/2}$ = 159.4 yr ± 1.9 yr (statistical) ± 3.7 yr (systematic) with$\chi^2_{DOF} = 1.01$. Based on all of our analysis presented here, on the ^{32}Si/^{36}Cl data, we regard this is as the most reliable half-life determination and present it as our result.

The results of repeating the regression analysis on the Bg-corrected data (using SPSS statistical software) are presented in Table 4.3. Compared to the correlation analysis performed on the non-Bg-corrected data, temperature and HV show a slightly weaker correlation to the fractional ratio residuals, while $1/R^2_{ES}$ exhibits a slightly stronger correlation. Building a model based on the simultaneous behavior of the above parameters results in a somewhat lower global Pearson correlation coefficient of

	Residuals	Temperature	Pressure	HV	LV	$1/R^2$
Residuals	1	-0.126	-0.010	0.127	0.082	0.120
Temperature	-0.126	1	0.048	-0.452	0.193	-0.696
Pressure	-0.010	0.048	1	0.080	-0.085	-0.083
HV	0.127	-0.452	0.080	1	-0.448	0.222
LV	0.082	0.193	-0.085	-0.448	1	-0.014
$1/R^2$	0.120	-0.696	-0.083	0.222	-0.014	1

Table 4.3
Table of Pearson Correlation values for environmental parameters and residuals of Bg-corrected ^{32}Si/^{36}Cl ratio decay data.

0.218, and we note that $1/R^2_{ES}$ moved up to the most important predictor (previously 3^{rd} after temperature and HV) reported by SPSS. The overall model scored 4.8% accuracy, similar to the previous model for the non-Bg-corrected data. A rolling correlation on the Bg-corrected data did not exhibit any notable changes, nor did the stacked month-by-month BNL and NH residual plots, so further discussion of these is skipped, for brevity.

4.8 Extended Half-Life Determination

An interesting opportunity arises from the fact that we have observed the same physical samples first studied by Alberger and Harbottle at BNL. Due to the design of BNL and NH experiments, namely utilizing the ratio of ^{32}Si/^{36}Cl in order to determine the half-life, differing systematics are suppressed. In the case of gain shifts manifesting differently in the two isotopes, we have corrected for the effect, as discussed previously. Thus, we perform an extended fit over the entire 33 years containing the two observation periods, which greatly increases the baseline of the determination to a significant fraction of ^{32}Si's half-life. Because the intrinsic event rate should lie along the same exponential curve, we can solve for the requisite 'geometric factor' arising from differences in solid angle subtended by the respective

detectors, by which to shift the NH data up or down. All NH data are scaled by the same value, such that these data are not biased by the operation. The significant increase in the baseline constrains the fit to a much higher degree than was achievable in previous direct counting determinations, yielding a relatively small uncertainty on the determined half-life. For this exercise, we have used the non-Bg-subtracted NH data, mirroring the non-removal in the BNL data.

The functional form to which the entire data set is fit can be written as

$$f(t) = \left[A \times e^{-\lambda t}\right]\left(1 - \mathcal{H}\left(t\right)\right) + \left[\Gamma \times A \times e^{-\lambda t}\right]\mathcal{H}\left(t\right) \tag{4.5}$$

where the Heaviside function, $\mathcal{H}\left(t\right)$, is defined by:

$$\mathcal{H}(t) = \begin{cases} 0, & t < Jan1, 2013; \\ 1, & t > Jan1, 2013; \end{cases}$$

and Γ in a geometric scaling factor.

In order to determine Γ, Excel's solver function was utilized to perform an iterative minimization of χ^2_{DOF} (arising from an exponential fit), while allowing λ, Γ, and A to vary. For consistency and presentation, the NH data were multiplied by the geometric factor, and the entire data set was fit to an exponential using Igor. Given the matching period and phase of oscillation, shown in Figs. 4.27 and 4.28, the data were also fit to the previously defined combined exponential+cosine function 4.3. The difference in half-life determinations between the two fits was 0.07 yr, with the combined function yielding a slightly better χ^2_{DOF} (See Fig. 4.35).

To show the fit of the cosine term to the data, separate graphs are shown (Figs. 4.36 and 4.37), scaled to the individual data sets. Histograms of the residuals resulting from the purely exponential fit and the combined exponential+cosine fit are presented in Figs. 4.38 and 4.39. The half-life of ^{32}Si determined by the best-fit

exponential+cosine function is 160.0 ± 0.11 yr (statistical) ± 0.22 yr (systematic), with a period of 1.07 ± 0.01 yr and a χ^2_{DOF} 0.96.

Finally, performing a global half-life determination across the BNL and Bg-corrected NH data shows improvements in the fit. Figures 4.40 and 4.41 show the global fit, zoomed in on the time domain of each experiment.

The fit results in a half-life of 161.7 yr ± 0.11 yr (statistical) ± 0.22 yr (systematic) with $\chi^2_{DOF} = 1.01$. The histogram of the residuals of this fit is shown in figure 4.42. The fact that the global fits to the BNL and NH data sets result in approximately the same χ^2_{DOF} as the individual NH analysis is a good indicator that the analysis is reasonable. The 33 yr span of the combined data set offers further confidence in the NH half-life determination, as it covers a significant fraction of the half-life and is consistent with the earlier determination.

4.9 Summary

Half-life determinations from various experiments are listed in Table 4.4, exhibiting a clear lack of consensus. The grouping of determined values by method, suggests that the discrepancies are of systematic origin, though we note that our determination is consistent with Thomsen's AMS + activity result [42], which differs from the other AMS determinations substantially. Although not large, the discrepancy between our determination and that of the BNL experiment is possibly explained by the unknown contribution of their background or more obscure systematic effects in either experiment.

Referring back to equation 4.4 once again, we can make a basic estimate on the size of trend in the Bg at BNL that would be required to bring our half-life determinations into agreement. Adjusting each Si_{BNL} and Cl_{BNL} datum by a linear trend between +0.1 cps (in the beginning) and -0.1 cps (at the end), we determine an adjustment to their half-life determination of $\sim$ 3 yr, which would make our respective determinations consistent at the 1σ level. It may be interesting to investigate the cosmic muon

Method	$T_{1/2}$ (yr)	Reference
Ice Core	330(40)	Clausen [43]
	222, 277	Clausen → Demaster [44]
Sedimentary Core	276(32)	Demaster [44]
	217(29)	Demaster → Cumming [45]
AMS	101(18)	Kutschera et al. [46]
	108(18)	Elmore et al. [47]
	132(13)	Chen et al. [48]
Activity + AMS	133(9)	Hofmann et al. [49]
	162(12)	Thomsen et al. [42]
Direct Decay Measurement	172(4)	Alburger et al. [1]
	159.4(5.6)	This Work

Table 4.4
Summary of half-life determinations for ^{32}Si, grouped by method.

flux during this period as well as comparing it to the period of the NH experiment regarding both the half-life determinations and observed cyclic modulation.

The analysis of the NH data both before and after Bg subtraction has been instructive for several reasons. First, it allows us to better understand the BNL data and the likelihood of Bg fluctuations causing the observed periodic modulation of their decay data. As previously noted, a seasonal change in background of approximately 0.8 cps could have affected their ratio decay data at the level of 1×10^{-3}. However, analysis of our own data showed that removing the Bg only marginally affected the observed modulation. In light of these results, we are scrutinizing the Bg correction algorithm to be certain we are achieving optimal results. The need for daily Bg observation has become clear and is being implemented as we move forward.

Additionally, we aim to improve our experimental platform in a few other areas, using the knowledge gained during this phase. These improvements include maintaining highly stable temperature and HV, conducting longer term, more precise

characterizations of the platform, and evaluating possible improvements to the scaling process. Heightened stability in HV, alone, will greatly diminish the range over which the scaling algorithm is required to operate.

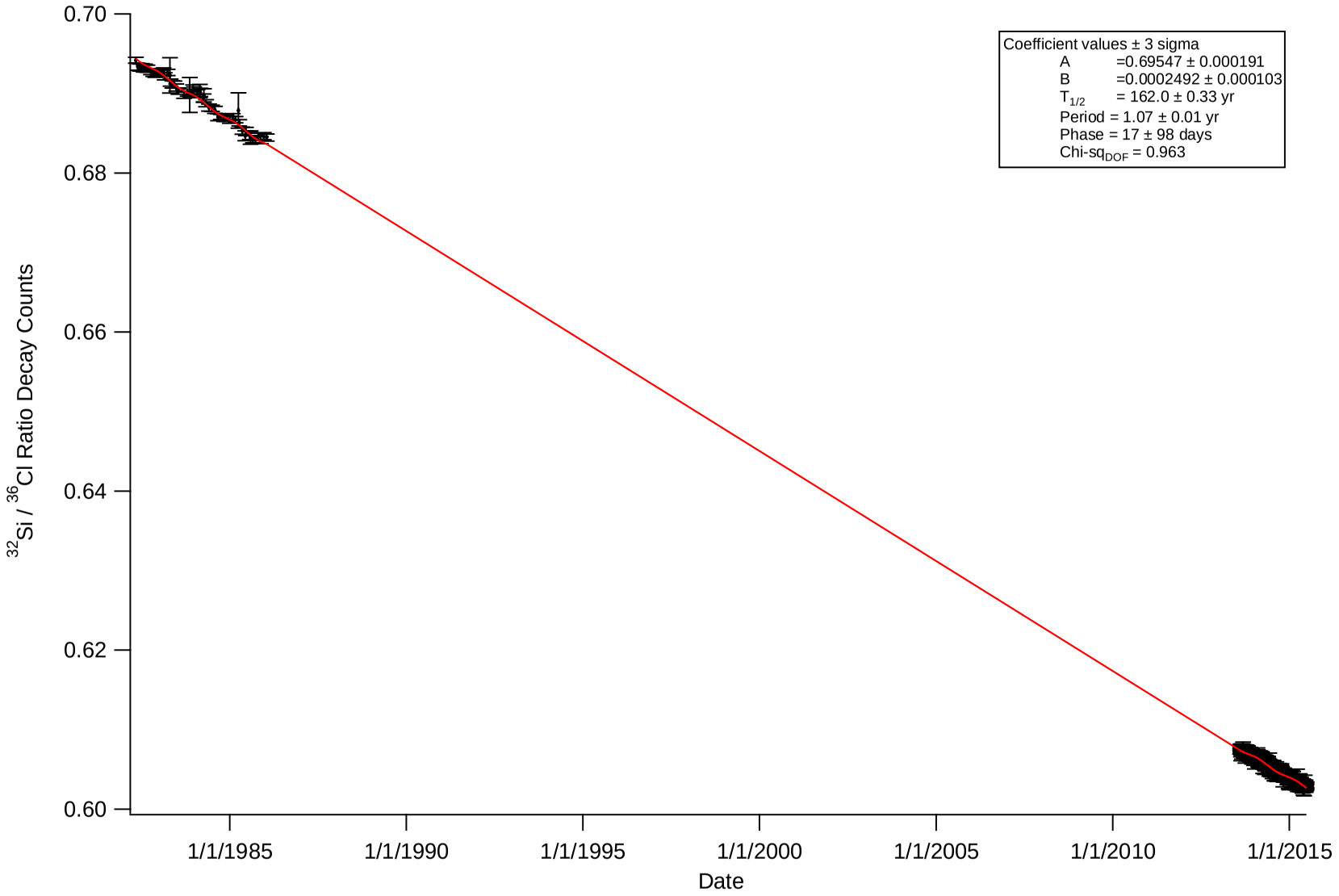

Figure 4.35. Exponential+cosine fit to extended BNL and non-Bg-corrected NH ratio data eq:(4.3).

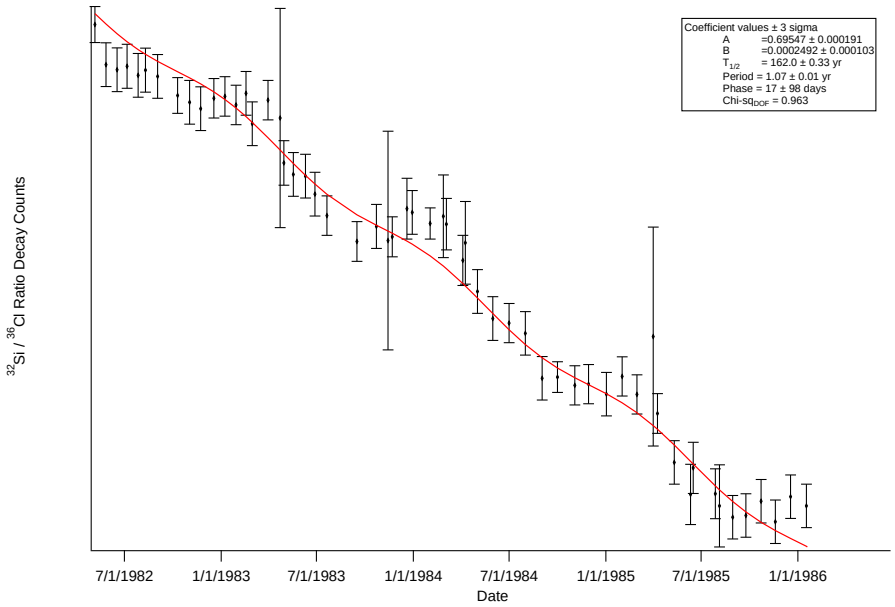

Figure 4.36. BNL data region of the extended fit to the combined exponential+cosine function (eq:4.3).

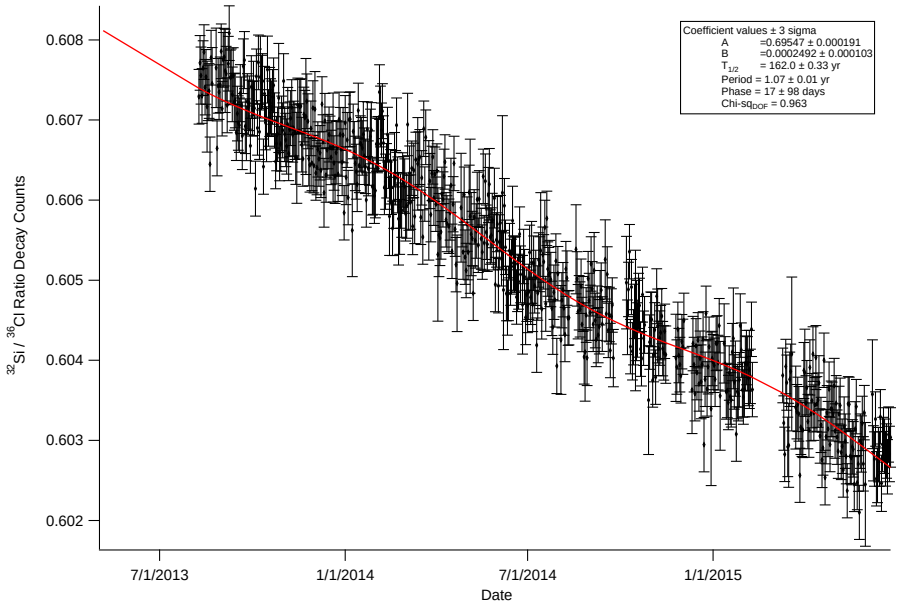

Figure 4.37. NH data region of the extended fit to the combined exponential+cosine function (eq:4.3).

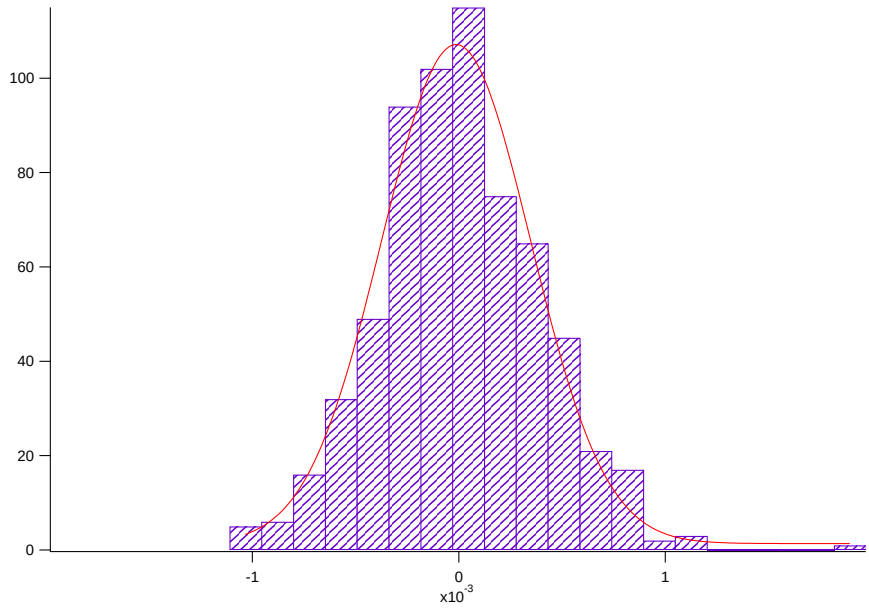

Figure 4.38. Histogram of residuals of a purely exponential fit to the extended BNL and non-Bg-corrected NH data set.

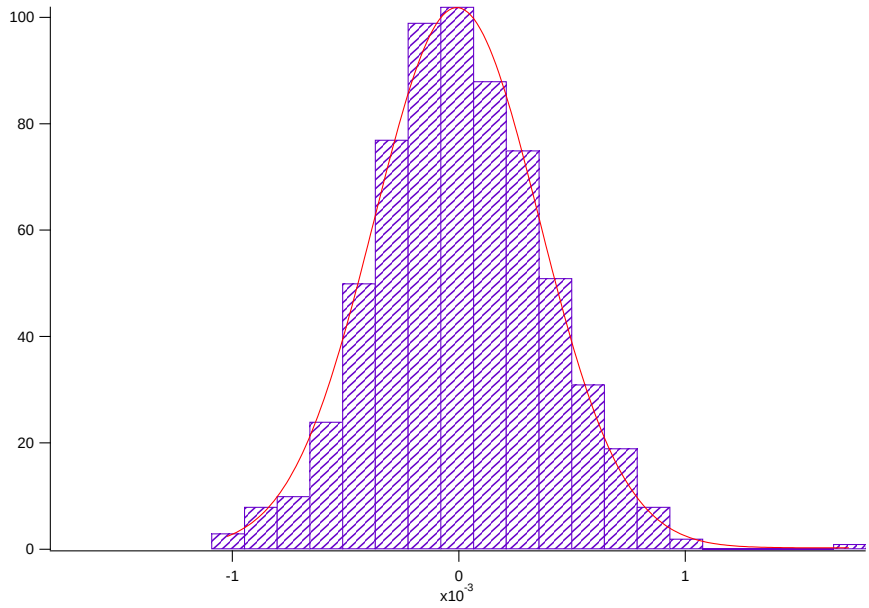

Figure 4.39. Histogram of residuals of the combined exponential+cosine fit to the extended BNL and non-Bg-corrected NH data set.

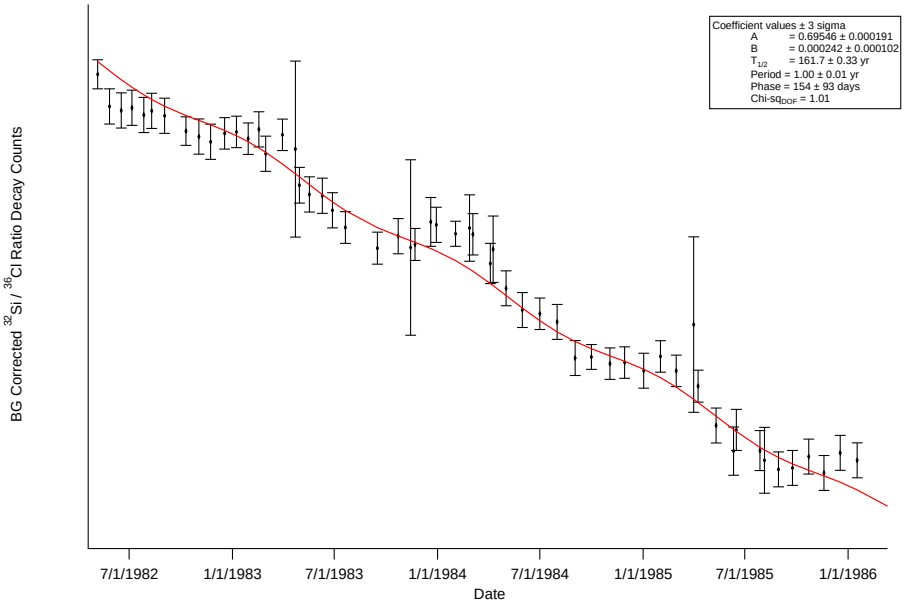

Figure 4.40. BNL portion of the global exponential+cosine fit to the BNL and Bg-corrected NH data, simultaneously.

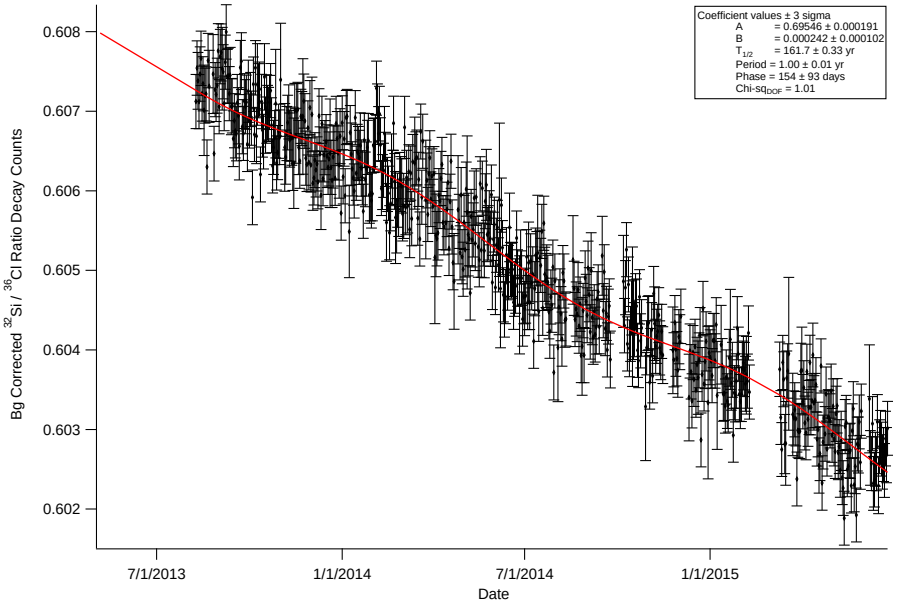

Figure 4.41. NH portion of the global exponential+cosine fit to the BNL and Bg-corrected NH data, simultaneously.

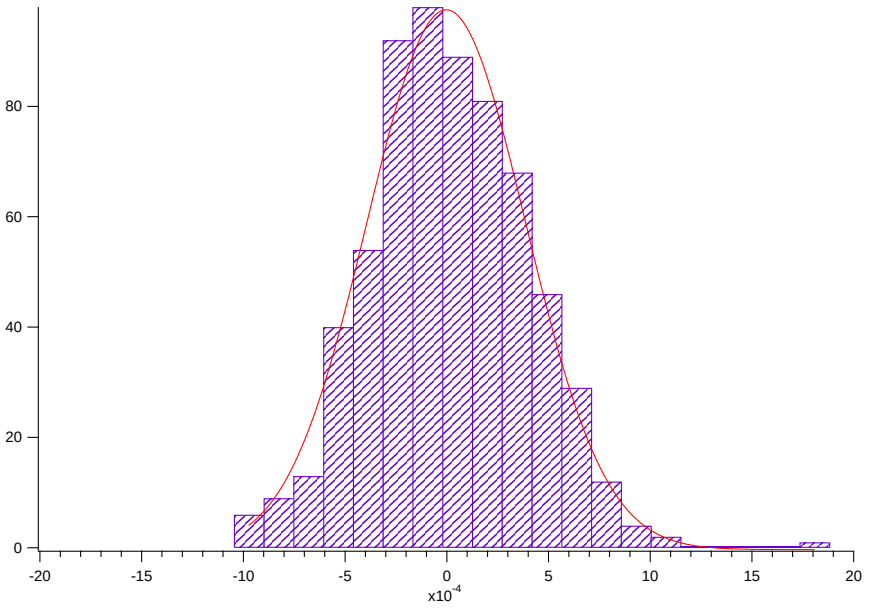

Figure 4.42. Histogram of the residuals for the global exponential+cosine fit to the BNL and Bg-corrected NH data.

5. Self-Induced Decay

5.1 Background

Anomalies encountered during preliminary analysis for a seemingly unrelated experiment (discussed in the next section), provided the motivation for revisiting the SID prescription, which was done in collaboration with J. Nistor [50]. A number of reported periodic variations in nuclear decay rates is (see Table 1.1). The observed frequencies suggest an association with the Sun, as in the case of an annual signal presumed to arise from the annual variation of the Earth–Sun distance [51], a (10–15) yr^{-1} variation associated with the Sun's rotation [52,23], a Rieger periodicity [9], and a short-term statistically significant change in the ^{54}Mn decay rate coincident with a solar flare [11]. Further evidence of a connection between nuclear decay and solar indices data is reported in [24]. A possible mechanism to account for a solar influence would be a coupling of the decaying system to solar neutrinos ($\nu_\odot$) via some as yet unknown interaction.

A test of the solar neutrino hypothesis was carried out in Refs. [53] and [54], which compared the decay rates of ^{198}Au in a thin gold foil, a gold wire, and a gold sphere having both the same mass (1 mg) and the same specific activity. The basis for this comparison was the observation that the electron-antineutrinos ($\bar{\nu}_e$) produced from those ^{198}Au atoms undergoing decay would bathe the undecayed atoms in the sphere in a flux of $\bar{\nu}_e$ that could be comparable to (or even greater than) ambient $\nu_\odot$ flux. If the effects of $\bar{\nu}_e$ on a decaying atom were similar to those of $\nu_\odot$, then the decay rate of the spherical sample could be measurably different from that of the foil or wire, in which most $\bar{\nu}_e$ would presumably leave the sample without significant influence on the decay process. It is clear that this hypothesized "self–induced decay" (SID) effect in the sphere is a non-linear phenomenon since its effect on the activity of the sample

Run	$T_{1/2\,\mathrm{exp}}$ (hr)	χ^2_{exp}	$T_{1/2\,\mathrm{SID}}$ (hr)	χ^2_{SID}
Au105	64.365 ± 0.007	1.44	64.642 ± 0.008	0.98
Au301	64.062 ± 0.017	1.52	64.629 ± 0.019	1.04
Au401	64.394 ± 0.005	1.56	64.610 ± 0.006	1.12
Au501	64.484 ± 0.007	1.10	64.574 ± 0.008	1.05
Au502	64.078 ± 0.004	6.32	64.672 ± 0.005	1.05

Table 5.1
Exponential and SID fits to net counts for various ^{198}Au data sets. The NIST published value for ^{198}Au is $T_{1/2} = 64.684 \pm 0.005$ hr.

depends on the activity itself. As shown in Ref. [53], the SID effect is characterized (to first order) by the differential equation

$$-\frac{dN(t)}{dt} \equiv -\dot{N} \cong \lambda_0 N(t)\left[1+\xi\frac{N(t)}{N_0}\right], \tag{5.1}$$

where λ_0 is the decay constant in the absence of SID (i.e. $\xi = 0$), N is the number of activated nuclei, and $N_0 \equiv N(t=0)$.

The objective of this discussion is to highlight the similarities of predicted SID behavior to that of typical dead-time effects, which are a consequence of the fact that detector dead-time effects are also non–linear in the activity of the sample (or more precisely the count rate). Hence, dead-time effects could be confused with the SID effect and vice versa. The result is that certain dead-time corrections may remove non–linearity in decay data which may arise from fundamentally physical, rather than instrumental, origins.

5.2 Experimental Motivation

A reactor based experiment was designed to irradiate several short-lived isotopes on a regular basis and subsequently observe them via direct decay measurements in order to determine the half-lives repeatedly throughout the year. The primary

objective was to determine whether these shorter lived isotopes exhibit an annual time-dependence in their decay rates, similar to the those presented in Table 1.1, which would otherwise be obscured by their short life-times. During the course of this experiment, we experienced significant obstacles due to technical reactor issues and maintenance. Though the original scope of the experiment was unable to be realized, it provided the means for the analysis presented in this section. The samples studied are listed in Table 5.2.

Isotope	Decay Mode	Half-life	Significant Photons (keV)	Intensity
^{116m}In	β^- : 100.00%	54.29 m	411.8	95.62%
^{56}Mn	β^- : 100.00%	2.5789 h	846.754	98.9%
			1810.72	27.2%
			2113.05	14.3%
^{187}W	β^-: 100.00%	23.72 h	479.53	26.6%
			551.55	6.14%
			618.37	7.57%
			685.81	33.2%
			772.87	5.02%
^{76}As	β^-: 100.00%	1.0942 d	559.10	45.0%
			657.05	6.2%
			1216.08	3.42%
^{198}Au	β^-: 100.00%	2.6952 d	411.80	95.62%
^{122}Sb	β^-: 97.59%	2.7238 d	564.24	70.67%
	ϵ: 2.41%		692.65	3.85%

Table 5.2
Isotopes under study in the PUR1 reactor experiment with energy of prominent gammas in each istotope's spectrum.

5.2.1 Experimental Setup

Up to three samples were run simultaneously utilizing two [Bicron] 3-inch NaI(Tl)well detectors and an HPGe detector. The well detectors were connected to Ortec Digibases and a PC running Ortec's Maestro32 MCA software, while the HPGe setup used Ortec nim-bin modules connected to a PC running the same Maestro MCA software. Each well detector is housed in a two-inch-thick lead cave to minimize background counts and events from the other sample (see Figure 5.1). The HPGe setup was in a separate room, and the detector was housed inside a cylindrical copper shield. The ^{116m}In and ^{187}W samples, due to their complex energy spectra, were run on the HPGe setup due to the greater energy resolution afforded.

Figure 5.1. Each NaI well detector is housed in a 2-inch-thick lead cave. The sample vials are placed in the well for counting.

5.2.2 Sample Preparation

The mass of each sample was optimized based on the available neutron flux near the core of PUR1 and the relevant reaction cross section for neutron capture, such that a convenient time of irradiation was achieved. The mass was recorded and the sample placed in a small polyethylene vial and heat sealed (see figure 5.2). The vial was then cleaned with ethyl alcohol and rinsed with deionized water before being labeled with a unique ID number so that a sample's run history could be tracked. Several samples of each isotope were utilized in order to allow an observed sample to return to low activity before being irradiated again; typically, samples were allow to 'cool' for 10 half-lives or more.

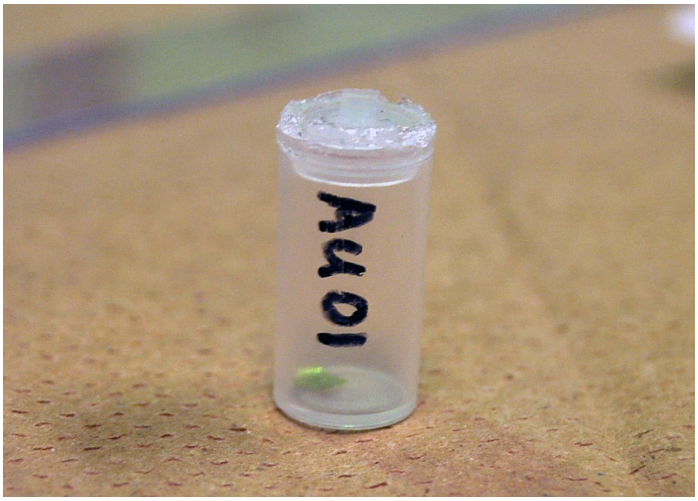

Figure 5.2. The samples were weighed and sealed in a polyethylene vial, cleaned and labeled.

5.2.3 Procedure

According to a weekly schedule, a sample was lowered into the reactor pool adjacent to the core for a predetermined length of time in order to achieve an initial activity optimized for data collection. After the allotted time, the sample was pulled

from the reactor and immediately checked for activity using a Geiger counter. If the activity level was suitable, the sample was placed into a well detector for counting. Otherwise, the sample was allowed to cool, briefly, or lowered back into the reactor as needed. We chose ∼3500 cps as a suitable initial count rate so as to minimize dead time while still accumulating sufficient data for statistical considerations. The activity of a sample at the end of irradiation is given by:

$$A_0 = N\phi\,\sigma S \tag{5.2}$$

where N = number of target particles in sample, ϕ = neutron flux through target, σ = reaction cross section, and the saturation, S, is given by:

$$S = 1 - e^{-ln(2)t_i/t_{1/2}}$$

where $t_{1/2}$ = half-life of sample and t_i = irradiation time. Typical irradiation times were 3-5 min.

5.3 Analysis

Of particular interest to the discussion on SID are the data collected on ^{198}Au, which were in the form of thin foils, typically of mass 12-13 mg. The integral data from the dominant 412 keV peak were analyzed using a weighted least-squares fit to an exponential function. Half-life determinations were near the expected value ($T_{1/2}$ = 64.684(5) hr), but exhibited unexpected variations within subsets of the data, and for data sets with significantly higher count rates. Further analysis repeatedly showed an anomaly in the residuals of the detrended count rates, as depicted in Figure 5.3, which are expected to be distributed normally about unity. Similar anomalies were seen in data from other nuclides measured with different detection systems. In the process of investigating the role of dead-time in this behavior, it was discovered

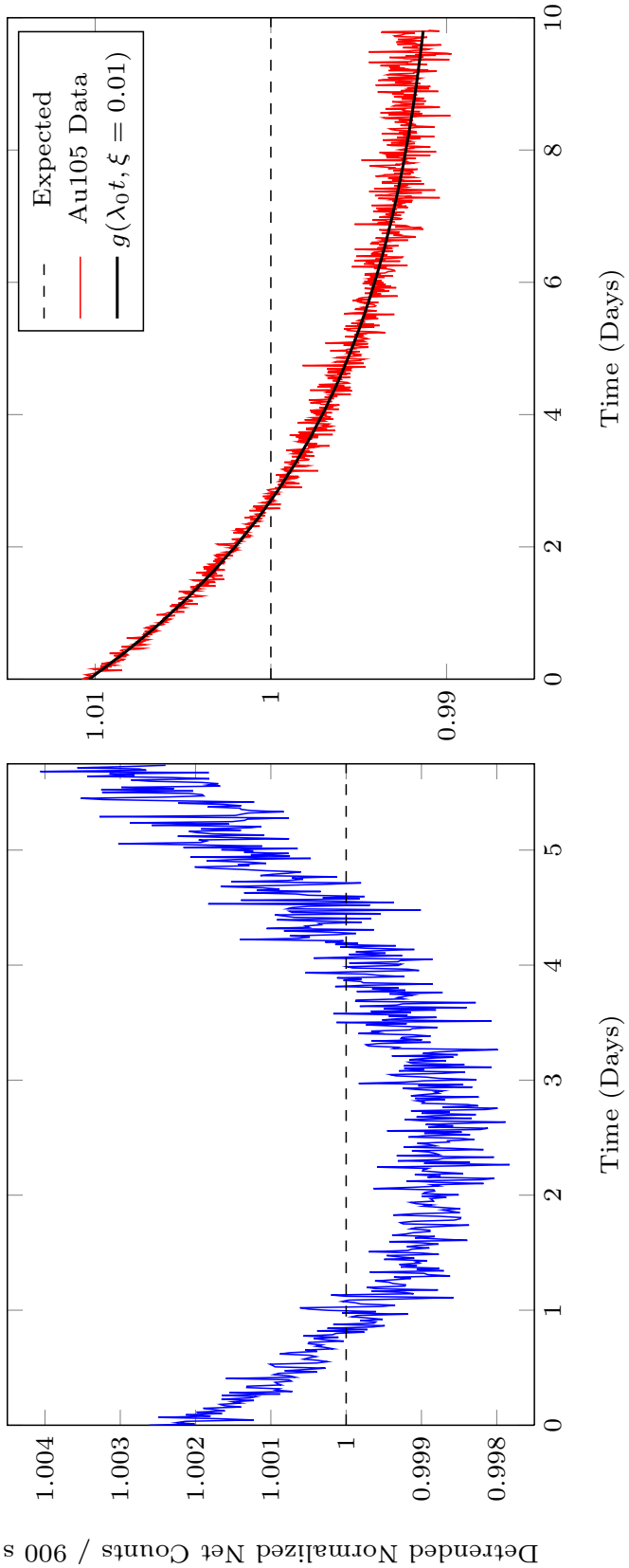

Figure 5.3. Detrended and normalized ^{198}Au counts per 900 second fixed live-time interval. (*Left*) The data were detrended assuming a pure exponential decay model. (*Right*) A representative example of the detrended ^{198}Au net counts (red, solid curve) using best-fit SID parameters. The expected behavior in the absence of SID or experimental bias (black, dashed line) is a random distribution of points about unity. The prediction from a SID perturbation is represented by the solid (black) curve. The function $g(\lambda_0 t, \xi)$ is defined in Eq. (A.12).

that a SID-corrected function yielded better fits and produced more consistent results for half-life determinations. As shown in appendix A.2, it turns out that the behavior of a sample experiencing a SID effect is functionally indistinguishable (to first order in ξ), from the behavior under a systematic over-correction of the dead-time. With that in mind, we present the former case, though the corrections are applicable in both circumstances.

To evaluate the possible presence of a SID effect in our samples, the decay data were analyzed by a weighted best-fit to the first-order SID function (see discussion in section. A.1). The relevant fit parameters were then used to detrend the decay data, and the results (illustrated in Figure 5.3) closely matched the SID prediction presented in Ref. [53]. A SID presence would initially cause depopulation of the sample more quickly than predicted by purely exponential behavior. This in turn would cause the future decay rate to be smaller than expected under exponential behavior, with the crossover necessarily occurring at $T_{1/2}$.

Calculated values for χ^2_{DOF}, presented in Table 5.1, show improvement for the SID prescription compared to an exponential fit. Of particular note is run 'Au502', whose initial activity was roughly double that of the next most active ^{198}Au sample observed. A higher specific activity would be expected to lead to a more pronounced SID effect. While the SID prescription continues to fit very well with this larger non-exponential behavior, the purely exponential fit is poor, yielding $\chi^2_{DOF} \approx 6$.

Analysis of the residuals of the net counts for both the purely exponential fit and the SID fit highlights the differences between the two methods of analysis presented here. The histogram of residuals for the SID fit, presented in Fig. 5.4, shows an approximately Gaussian distribution, whereas the corresponding distribution for the exponential fit is skewed. Plots of the residuals as a function of time further highlight the differences; under the SID prescription, the residuals exhibit a relatively normal distribution about zero, whereas the residuals of the exponential fit show a marked departure. The shape of the exponential-fit residuals is consistent with the sample initially decaying faster than predicted by an exponential model. Analysis of data for

Isotope	$T_{1/2\ \mathrm{exp}}$ (days)	Avg χ^2_{exp}	(min, max)	$T_{1/2\ \mathrm{SID}}$ (days)	Avg χ^2_{SID}	(min, max)
^{198}Au	2.68426 ± 3.9×10^{-5}	2.39	(1.10, 6.32)	2.6929 ± 1.4×10^{-4}	1.05	(0.98, 1.12)
^{76}As	1.09159 ± 8.7×10^{-5}	1.17	(1.03, 1.29)	1.0906 ± 3.6×10^{-4}	1.14	(1.00, 1.24)
^{122}Sb	2.67735 ± 9.5×10^{-5}	5.30	(1.72, 12.3)	2.6531 ± 3.5×10^{-4}	2.06	(1.14, 3.33)
^{56}Mn	0.10690 ± 5.9×10^{-5}	8.38	(1.14, 24.5)	0.10755 ± 1.26×10^{-5}	1.19	(0.78, 2.01)
^{116m}In	0.037906 ± 9.3×10^{-6}	1.83	(0.97, 2.17)	0.03763 ± 1.8×10^{-5}	1.25	(0.95, 2.14)

Table 5.3
Weighted averages of the half-lives of various isotopes using exponential and SID fits to net counts. The associated mean χ^2_{DOF} and range are presented.

other nuclides also shows improvements in fit under SID analysis. Table 5.3 displays the averages of the determined half-life for each nuclide, weighted by the associated error for each datum in the determination. The average χ^2_{DOF} for the exponential and SID fits is also presented, including the range. In all cases, the SID model provides a better description of the data than a pure exponential model. It is important to note that the improvement in fit is not simply due to adding an additional parameter; traditional ad-hoc dead-time corrections introduce an additional parameter, as well, as shown in appendix A.2. The result is that such dead-time corrections would result in discarding any existing SID or similar rate-proportional effect.

However, as previously indicated, it is also true that a larger initial activity corresponds to a higher count rate, and hence, increased dead-time in our experiment. While the Gedcke-Hale live-time clock utilized in this experiment corrects for rate-related losses such as dead-time and pileup, there exists an uncertainty in each time-correction. A systematic over/under correction would produce the same behavior, to first order, as the SID prediction. In either case, these results show the need for a procedure with which to correct for rate-related losses, especially when the observation period of the experiment is comparable to the half-life of the sample being studied. Although, in this case, it is impossible to decouple the two possible sources of the effect, it is possible to design an experiment which can distinguish between the two.

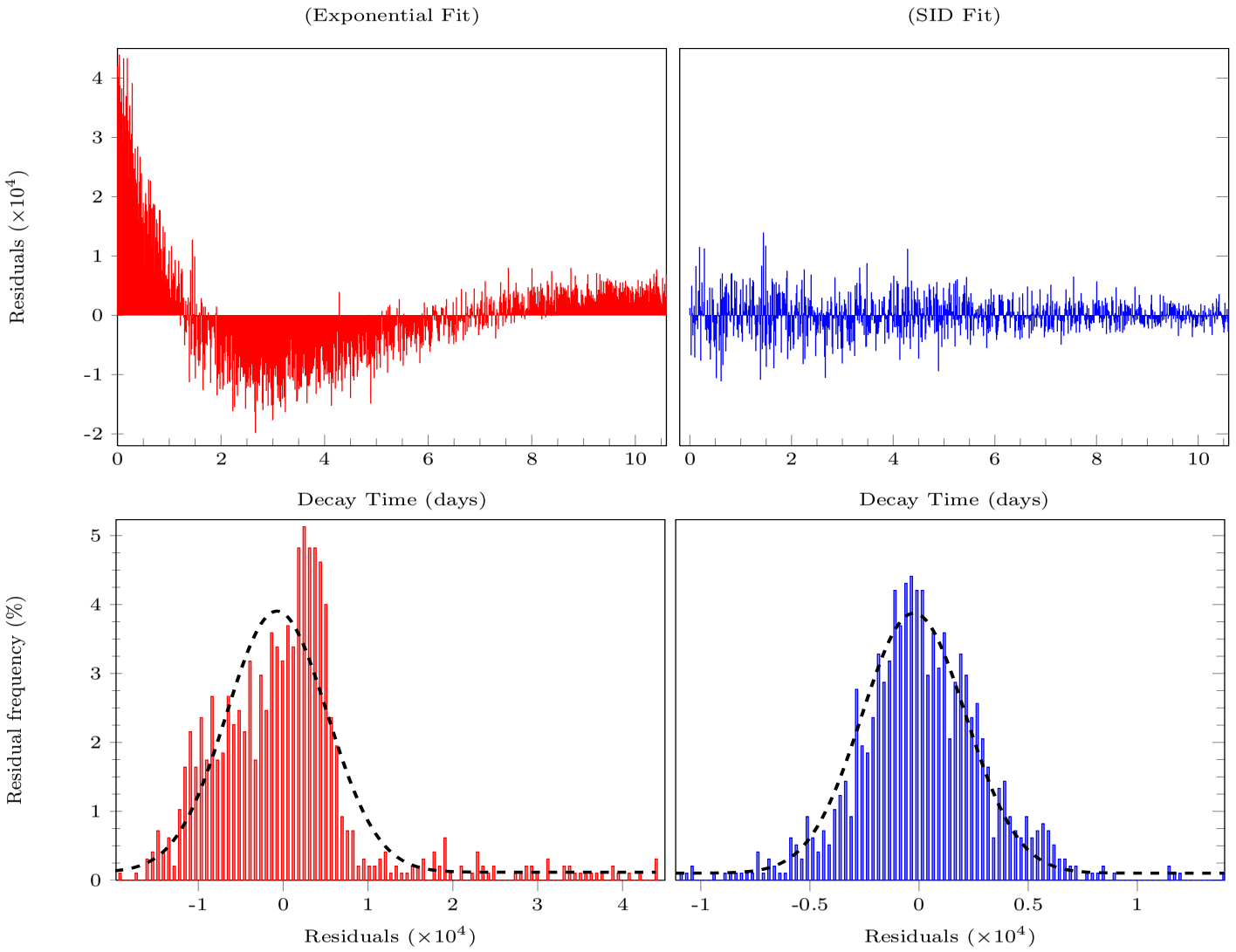

Figure 5.4. Residuals and histograms for pure exponential (left) and SID (right) fits

6. Conclusion

For the ~ 2 yr period represented in this work, we analyzed approximately 6,000 hours worth of data for each sample and have determined the half-life of ^{32}Si to be 159.4 yr $\pm$1.9 yr (statistical) $\pm$ 3.7 yr (systematic). A longer term characterization may allow the quoted systematic error to be reduced, however the values of χ^2_{DOF} obtained in our analyses indicate that we have sufficiently accounted for the uncertainties. Our half-life determination is consistent with that by Thomsen et. al. [42], and the results of performing extended fits across the BNL and NH data lends greater confidence in this determination.

We have also attempted to more fully understand the presence of reported modulation in decay data by carefully remeasuring the decay rates of ^{32}Si and ^{36}Cl while controlling and monitoring the environment of the experiment. Over the period included in the analysis, we recorded approximately 5×10^6 individual environmental readings. We found that the signal that was observed in the BNL data persisted in the NH experiment but was of smaller amplitude. This appears to suggest that the attention we have given to controlling for environmental effects reduced the variation. However, we have also reasoned that it is unlikely that the variation in temperature or detector voltage (presumably the most important factors, given the results of our correlation analysis and the degree to which we controlled the other parameters) is responsible for the modulation, since the ^{32}Si/^{36}Cl ratio exhibits the opposite behavior of what our characterization studies demonstrate. Further, our Bg corrections do not suppress the modulation to any significant degree, and bring the primary frequency of the modulation closer to 1 yr^{-1}.

We also note that although power spectrum analysis by P. Sturrock on both the BNL and non-Bg-corrected NH data show differing oscillatory behavior of the ^{36}Si vs ^{36}Cl samples between the two experiments, the ratio yields a similar variation.

This provides support for the efficacy of utilizing the ratio data in order to mitigate compounded systematic effects. Frequency analysis of the Bg-corrected data is forthcoming. Given the relationship of the data from the two experiments, we have presented a methodology for combining them to produce an extended 30+ yr global fit, which imposes an additional constraint compared to the standard practice of averaging reported values.

Finally, we have presented an analysis of the SID effect with respect to its similarity to rate-related losses in the counting system. Our analysis shows that, at minimum, the fitting model we present provides a convenient way to correct for these losses as well as the possibility that an existing phenomenological effect might be discarded with traditional dead-time corrections.

Our future plans for the NH experiment will address the technical issues encountered during this phase. We will begin collecting daily Bg observations and conduct further evaluation of the the Bg correction and scaling algorithms. The extended temperature stability provided by the PID-controlled peltier unit now affords us great latitude in characterizing the precise temperature dependence of our experimental platform while decoupling the HV supply from these imposed temperature changes, not to mention the benefit to our data acquisition in general. One can also imagine imposing a varying temperature regimen, which is different than the natural environmental cycle, in order to further investigate the issue. Additionally, a highly stable HV supply will address the issues regarding gain shifts that we encountered. Comparing the data collected under these conditions to the previous data, especially regarding the magnitude and phase of variation in the residuals, should be quite informative.

APPENDICES

A. Self-Induced Decay

A.1 SID Phenomenology

On a phenomenological basis, a natural way to investigate the periodicities presented in Table 1.1, as well as a possible influence from neutrinos, is to model the behavior as a modification to the standard exponential decay law, $-dN/dt = \lambda N$, where the decay parameter λ experiences a time–dependent perturbation,[1] i.e.,

$$\lambda = \lambda_0 + \lambda_1(t) \; . \tag{A.1}$$

Since the perturbation is presumed to arise from an interaction with neutrinos or antineutrinos (which will henceforth be referred to as neutrinos), λ_1 will be proportional to (or more generally, a function of) the ambient neutrino flux, which in principle may have contributions from a variety of sources (e.g. solar neutrinos, CνB relic neutrinos, geologic and atmospheric neutrinos, and artificial/reactor-generated neutrinos). For such an exotic interaction to exist in nature, past experimental observations constrain λ_1 to be much less than λ_0, at least for conditions typically encountered in terrestrial experiments.[2] This constraint suggests that it is appropriate to simplify subsequent expressions to lowest order in λ_1/λ_0. For the purpose of comparing SID with dead-time behavior, higher order SID terms will be discarded. The one exception will be throughout the discussion of the "extremal" behavior associated with SID.

As mentioned in Sec. 5, it is hypothesized that a sample undergoing β–decay or K–capture may in fact be able to affect its own rate of decay. Specifically, those atoms which have yet to decay will be bathed in a flux of neutrinos produced from the decaying atoms within the sample. Therefore, a sample with a sufficient internal

[1] We note that a time–dependence in λ does not necessarily imply a departure from randomness, but rather suggests a deviation in the probability distribution which governs the decay.

[2] One could imagine locations where the ambient neutrino flux is significantly larger than that encountered on Earth—such as near or within stellar bodies, for instance.

neutrino flux (i.e., greater than the $\nu_\odot$ flux) should exhibit an experimentally detectable deviation in its decay rate. It is perhaps surprising that an internal neutrino flux significantly higher than the $\nu_\odot$ flux is achievable in relatively small samples, as was accomplished in [53, 54] with a 1 mg gold sphere, foil, and wire.

Given such a case, where the various contributions to the total neutrino flux (within a given sample) are dominated by the the internally generated neutrino flux, it is reasonable to neglect all but this internal source and express the perturbation in the decay parameter as

$$\lambda_1 = -p\dot{N}. \tag{A.2}$$

Explicitly, it is here presumed that the perturbation is proportional to the density of emitted neutrinos, which in turn is proportional to the decay rate (p being the dimensionless proportionality constant). To be more general than Eq. (A.2), the decay parameter may contain additional contributions arising from external neutrinos (which is presumed to be the case for the periodicities observed in Table 1.1). However, for the specific case of a short-lived isotope, one would expect the time-dependence in λ to arise primarily from $\dot{N}$, while the $\nu_\odot$ contribution, for instance, would remain approximately constant during the sample's short lifetime. Using Eq. (A.2), the perturbed system can be characterized by the differential equation:

$$-\dot{N} = \left(\lambda_0 - p\dot{N}\right) N \tag{A.3}$$

$$= \frac{\lambda_0 N}{1 - pN}\,. \tag{A.4}$$

Before presenting a solution to Eq. (A.4), which is relevant for comparison with dead-time effects, we highlight a few points which have not been previously presented elsewhere. Since λdt can be regarded as the probability for an unstable atom to decay within a small time interval dt, it is reasonable to interpret $\lambda_1 dt$ as the probability within this time for an activated atom to decay, due to the proposed SID effect. In other words, the probability for an atom to decay is the sum of two distinct ways in which the decay can occur: a *spontaneous* decay ($\lambda_0 dt$), or an *induced* decay ($\lambda_1 dt$). In this context, the constant of proportionality in Eq. (A.2) can be regarded as the

probability (per emitted neutrino) for a SID to occur, since $-\dot{N}dt$ is the approximate number of neutrinos emitted in time dt.[3] Therefore, each neutrino emitted within a population of N activated atoms is expected to induce pN decays. It may appear at first glance that pN could exceed unity if a single neutrino were able to influence multiple unstable atoms while traveling within the sample. In fact, one could in principle attempt to irradiate a sample continuously until N becomes large enough so that pN is greater than unity; however, the technical question is how such a sample would be created.

To address this question, first consider an "ideal" sample of identical stable atoms which can be irradiated at will by placing the sample in a reactor, for example. Since the activated atoms in the sample will subsequently decay, there is a limit to how many stable atoms become activated—a limit which is reached when the decay rate of the sample (which increases as more atoms are activated) equals the activation rate of the reactor. If the sample being considered decays according to Eq. (A.4), then as pN approaches unity the decay rate diverges. No matter how powerful the reactor, the activation rate will be insufficient to activate more than $1/p$ atoms within the sample, i.e,

$$N_{\max} = 1/p \ . \tag{A.5}$$

This new example of secular equilibrium is depicted in Fig. A.1, and is in stark contrast to a sample governed by the standard decay law, for which the absolute maximum number of activated atoms is limited to the total number of atoms within the population. From this discussion, there is an unavoidable upper bound on pN such that:

$$\xi \equiv pN_0 < 1 \ , \tag{A.6}$$

where $N_0 < N_{\max}$ is the number of activated atoms immediately after the activation process is completed. Note that the SID parameter ξ is the quantity which may be

[3]It may be that p is negative, in which case, $-p$ is the probability of inhibiting a decay event from occurring. The treatment that follows will assume a positive value for p, but the treatment for negative p is readily inferred.

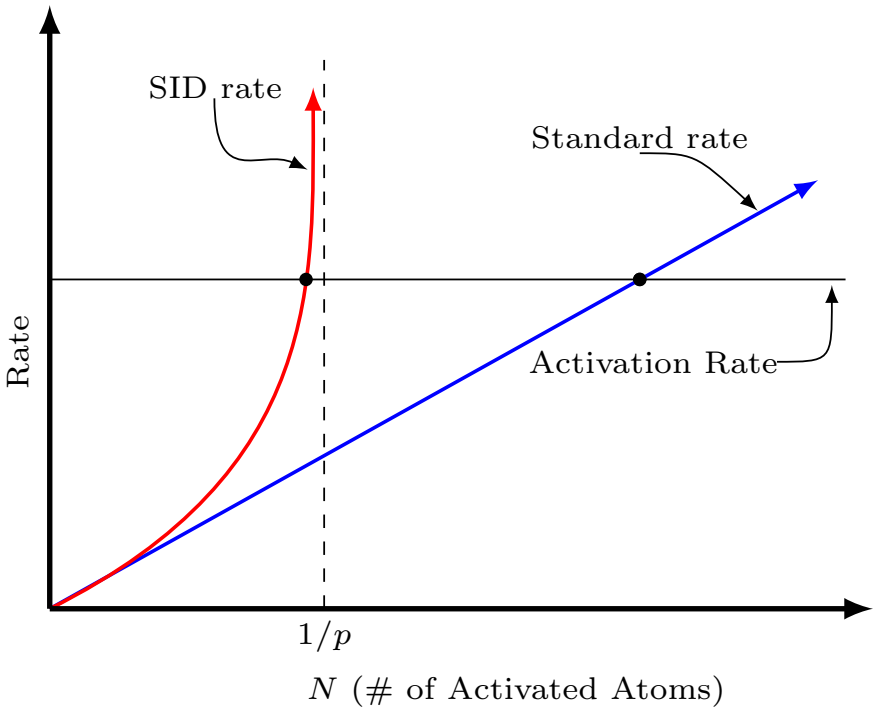

Figure A.1. An illustration depicting *secular equilibrium* for a sample exhibiting the SID behavior (red curve) and a sample undergoing standard exponential decay (blue curve). For a given activation rate, equilibrium is reached with *fewer* activated atoms for a sample undergoing SID decay, and the absolute maximum number of activated atoms is $N_{\max} = 1/p$.

directly measurable by experiment since it represents the fractional change in the decay rate from the expected behavior at $t = 0$.

Finally, given the aforementioned interpretation of p, we could have derived Eq. (A.4) simply by adding up all of the decays expected within a short time interval dt through the distinct ways a decay can occur. Since there are $\lambda_0 N dt$ decays expected to occur randomly, there will also be this many neutrinos available to stimulate additional events. With pN being the number of SID events expected per neutrino, $\lambda_0 N dt(pN)$ would be the expected number of induced decays. However, these SID decays, in turn, produce additional neutrinos for which $\lambda_0 N dt(pN)^2$ decays are expected. The pattern continues since at each stage the additional decays in turn pro-

duce additional neutrinos. Therefore, we can express the total number of expected decays, per unit time, as

$$-\dot{N} = \lambda_0 N + p\lambda_0 N^2 + ... = \lambda_0 N \sum_{j=0}^{\infty} (pN)^j \,, \tag{A.7}$$

where the right side of Eq. (A.7) will always converge for $|\xi| < 1$, and is readily identified with Eq. (A.4). From this construction it is evident that "higher–order SID processes" will have little influence on the total decay rate of the sample given that $|\xi|$ is presumably much smaller than unity. Furthermore, Eq. (5.1) can be obtained by retaining only the first two terms in Eq. (A.7).

The exact solution to Eq. (A.4) is most likely never required. Nevertheless, an implicit solution is obtained by integration, yielding

$$N(t)e^{-\xi N(t)/N_0} = N_0 e^{-\lambda_0 t} e^{-\xi}. \tag{A.8}$$

We can expand Eq. (A.8) in (pseudo) powers of ξ by making use of the *Lagrange inversion theorem*,

$$N(t) = \frac{N_0}{\xi} \sum_{j=1}^{\infty} \frac{j^{j-1}}{j!} \left(\xi e^{-\xi} e^{-\lambda_0 t}\right)^j \,, \tag{A.9}$$

where ξ is assured to fall within the radius of convergence on purely physical grounds. However, it is worth emphasizing that Eq. (A.9) is an accurate solution for situations up to $\xi = 1$, and therefore may be useful in studying the extremal behavior following from the preceding discussion. The decay rate, $n_\xi(t) \equiv -dN/dt$, can be determined from Eq. (A.9) as a series expansion. For typical situations it is sufficient to truncate the expansion to first order in ξ, in which case the decay rate becomes

$$n_\xi(t) = \frac{n_\xi(0)}{1+2\xi} e^{-\lambda_0 t} \left(1 + 2\xi e^{-\lambda_0 t}\right) , \tag{A.10}$$

where $n_\xi(0)$ is the initial decay rate, and the truncation error is on the order of $\mathcal{O}(\xi^2)$. In general, terminating the expansion to the jth term results in a remainder $R_j(\xi, t)$ which decays much more quickly in time than the activity of the sample. In fact, this remainder is comparable to $R_j(\xi, t) \sim \left(\xi e^{1-\xi} e^{-\lambda_0 t}\right)^{j+1}$. Furthermore, we see directly

from Eq. (A.4) that the initial SID rate $n_\xi(0)$ is greater (when $\xi > 0$) than the initial non-perturbed rate, and the two are related according to

$$(1-\xi)\, n_\xi(0) = n_0(0)\ , \tag{A.11}$$

where $n_0(0) \equiv \lambda_0 N_0$ is typically understood to be the initial activity of a sample.

In past discussions in the literature ([53], [54]), one useful quantity that has been studied is the ratio of decay rates with and without a SID effect:

$$g(x,\xi) \equiv \frac{n_\xi}{n_0} = 1 - \xi + 2\xi e^{-x}\ . \tag{A.12}$$

Previous searches for the SID effect (such as those conducted in Refs. [53] and [54]) sought to compare samples of similar activities but differing geometries. In this case, the values of ξ will differ between the samples due to the geometric dependence on p. Consequently, the ratio of the decay rates of one sample to the other is expected to have a temporal trend proportional to $g(\lambda_0 t, \Delta\xi)$, where $\Delta\xi$ is the difference between the values of ξ for each sample. A plot of $g(x, \Delta\xi)$ is shown in Fig. 1 of Ref. [53].

It will be useful in what follows to rewrite n_ξ in terms of a purely exponential rate in order to compare this behavior to the perturbations associated with dead-time, which will be discussed in Sec. A.2. In fact, the *event rate* as seen by the front end of a detector can be written as

$$m_\xi(t) = m_0(t)\left[1 + \beta m_0(t)\right]\ , \tag{A.13}$$

where $\beta \equiv 2\xi/m_0(0)$, and $m_0(t)$ represents an exponential decay rate with decay constant λ_0. It is apparent from Eq. (A.13) that the fractional change in the count rate $(m_\xi - m_0)/m_0$ shares the same time–dependence as $m_0(t)$. It is *also* true that rate-related perturbations associated with dead-time losses are proportional to the count rate. Therefore, we turn now to investigate the effects of dead-time on detector event rates and compare these effects the SID rates discussed above.

A.2 Dead-time behavior

We proceed in this section to a discussion of dead-time behavior with the aim of exhibiting the similarity between dead-time effects and those arising from the SID behavior. Rate-related losses due to dead-time may arise from any part of the counting system, and the magnitude of these losses is directly proportional to the counting rate itself. Many procedures exist to correct for rate-related losses. Typically these procedures are validated under conditions far more severe than those found in routine metrology, and thus are considered well-motivated. The subject of this section is to study a few simple dead-time models in an effort to elucidate their effects on time-dependent event rates. To this end, we consider the somewhat idealized behaviors of *extending* and *non-extending* dead-time.

A.2.1 Extending dead-time

Pileup in the amplifier (also called random summing) is a classic case of extending dead-time. When counting rates are relatively high, the random spacing of radiation pulses may result in interfering effects between pulses. *Peak pileup* occurs if two pulses are sufficiently coincident in time that they are treated as a single pulse in the counting system. The effect of peak pileup of two events is to essentially shift both from their proper position in the energy spectrum. *Tail pileup*, which can occur significantly even at relatively low count rates, involves the superposition of two slightly overlapping pulses. The main effect of tail pileup on the measurement is to worsen and distort the spectrum resolution.

The counting losses which result from pileup can be modeled as those events which occur within a time spacing less than a particular time following a previous event. Let α denote the minimum time by which two events must be spaced in order for each event to be resolved properly, I represent the instantaneous event rate of the decay within the detector, and I' represent the measured event rate out of the amplifier. The fraction of events which are spaced by a time interval between T and $T + dT$

is given by $IdT\exp(-IT)$, which can be interpreted as the probability of all nuclei surviving for a time T followed by a decay in a time dT. Therefore, the fraction of events which are *not* piled up, f, is given by

$$f = \int_{\alpha}^{\infty} e^{-IT} IdT = e^{-\alpha I} \ . \tag{A.14}$$

Consequently, if only those events free from pileup contribute to the measured rate, then the measured rate I' can be expressed as

$$I' = Ie^{-\alpha I}, \tag{A.15}$$

where the extending dead-time (pileup) parameter α can be determined in successive counting experiments through a least-squares type fit. Pileup *correction factors* f_P, by which each datum is adjusted, take the form

$$f_P \equiv \frac{I}{I'} = e^{\alpha I}. \tag{A.16}$$

Another representation of these correction factors is obtained by using the macroscopic dead-time (DT) to approximate the counting rate, yielding

$$\frac{I}{I'} = e^{P\,(DT/LT)} \ , \tag{A.17}$$

where LT denotes the detector livetime for the counting period. The unknown pileup constant P along with I are determined from a least-squares fit of $\ln I' = \ln I - P\,(DT/LT)$. It is worth noting that in either case, the constants P and α are usually not measured directly. Rather, they are best-fit determinations of a least-square or χ^2 type minimization procedure.

It is a curious observation that a SID–related deviation from an exponentially decaying event rate resembles the effect of pileup in the amplifier. In fact, expanding Eq. (A.15) in powers of α, we obtain

$$I'(t) = I(t)\,[1 - \alpha I\,(t)] + \mathcal{O}(\alpha^2), \tag{A.18}$$

which bears the same form as Eq. (A.13) for an exponentially decaying source. Although α is strictly positive to represent losses from pileup, ξ can be positive or

negative depending on the particular mechanism – appearing as "rate-related gains" ($\xi > 0$) or rate-related losses ($\xi < 0$).

The similarity of Eqs. (A.13) and (A.18) raises the question of what the effect from pileup would be on a SID–perturbed count rate, $m_\xi(t)$. As outlined above, the general form of Eq. (A.15) is obtained by considering the probability for two incoming events to occur within a particular time interval. Furthermore, these events are assumed to be governed by a Poisson process, or equivalently, presumed to occur randomly in time and independent from one another. While the condition for randomness may remain valid when considering a SID process, the condition for *independence* falls under scrutiny. Namely, each induced decay is the result of prior events and therefore cannot be considered to occur independently. In fact, it is likely that each SID event would essentially occur almost simultaneously with the event which induced it, and therefore a disproportionately large number of events would be subjected to peak pileup.

The derivation of an exact expression analogous to Eq. (A.15) for a SID process would require a rigorous development of the distribution of time intervals for this process. An approximation suitable when ξ is sufficiently small can be obtained by estimating an atom's survival probability for a time T to be $N(T)/N_0$, where $N(T)$ is given by Eq. (A.9). Additionally, the probability for an atom to decay is necessarily time–dependent, as underscored in the modified form for $\lambda(t)$. To lowest order in ξ, the effect from pileup on a SID event rate m_ξ, given in Eq. (A.13), can be represented as

$$I'(t) = m_0(t)e^{-\alpha' m_0(t)}. \tag{A.19}$$

where $\alpha' \equiv \alpha - \beta = \alpha - 2\xi/m_0(0)$ can be considered the "effective" pileup parameter, and $\mathcal{O}(\alpha \cdot \xi)$ terms are considered to be of higher order. Since m_0 represents a pure exponential decay rate, the result obtained in Eq. (A.19) demonstrates that a SID–modified input signal can be mistaken for an exponential decay rate (with the same decay constant λ_0) after subject to pileup. Therefore, procedures which correct each

datum for pulse pileup could remove a SID perturbation almost entirely with an incorrect determination of the pileup parameter, α, or P.

A standard hardware solution to pileup is accomplished through the use of a pulser to estimate the correction factor as the ratio of pulser frequency with and without a source. Suppose a periodic pulse generator with frequency I_P is used to add an artificial peak to the spectrum being studied. Since the true input rate of the pulser is known, a measurement of the counts in the artificial peak allows for a determination of the fraction of events free from pileup. Once again, this fraction is given by Eq. (A.14) for a Poisson governed decay rate, and therefore the output rate from the pulser, I'_P, can be expressed as

$$I'_P = I_P e^{-\alpha I}, \tag{A.20}$$

where I once again represents the true event rate due to the decay. On the other hand for a SID event rate, Eq. (A.20) is unaffected to first order in ξ. This can be explained by the fact that the fraction of events which are free from pileup, f, is unaffected to lowest order in ξ. The perturbation to the output signal arises solely from the increase in the event rate. Since the pulser input rate is independent of the decay rate, the pulser method of correcting for pileup losses is immune from the removal of first-order SID effects.

A.2.2 Non-extending dead-time

Non-extending dead-time is perhaps the simplest model for a detector's response to an input signal I. For this model, the counting systems is "busy" (i.e. unable to receive any additional pulses) for a fixed time τ after each registered event. As a result, the measured counting rate, I', will be an underestimate of the true event rate according to:

$$I' = \frac{I}{1 + \tau I}. \tag{A.21}$$

The total amount of time for which the detector is "dead" during a counting interval, called the macroscopic dead-time DT, is given simply as the total accumulation

of these small intervals τ for the total number of registered events. That is to say, if M is the total number of registered counts in a time CT, then the detector is unable to register events for a time given by $DT = M\tau$. The effective livetime (LT) counting interval, therefore, is the time $LT = CT - DT$.

When the true event rate into a detector is small (that is when the time between events $\sim 1/I$ is significant in comparison to the detector response time τ), the non-extending dead-time behavior given by Eq. (A.21) will agree with the *extending* dead-time model in Eq. (A.15). We can see this from expanding Eq. (A.21) in powers of τI:

$$I' = \frac{I}{1+\tau I} = I\left(1 - \tau I + \mathcal{O}\left(\tau^2 I^2\right)\right) \ . \tag{A.22}$$

Although the two models agree for low event rates, the behaviors diverge significantly for high rates, and for the non-paralyzable model described by Eq. (A.21), the observed count rate will asymptote to a value of $1/\tau$ for large, true event rates.

It is common practice in nuclear spectrometry to perform successive counting measurements by fixing the livetime clock, since the dead-time DT is expected to change during each measurement when the decaying source has a lifetime comparable to the total time through which the experiment is conducted. If, on the other hand, the clock time CT is fixed, the true counting intervals will differ for different measurements. This issue can be addressed either by manual correction of the livetime or by automatically fixing the livetime clock in the multi-channel analyzer (MCA). There are various "livetime clocks" built into the systems widely used in research and industry. The Gedcke-Hale livetime clock is an example of one of the more well-proven, reliable livetime clocks.

Bias can be introduced in a counting measurement by inaccuracy in the livetime clock. The degree of this bias appears small in general, and over-correction by the MCA livetime clock appears most common in practice. One test of the livetime clock performance would be to insert a pulser into the counting system and compare the measured rate with the rate measured directly with a precision frequency counter. As a simple model, the effect of overcorrection (or bias) in the livetime clock can be

thought of as an error $\delta\tau$ in Eq. (A.21) associated with each registered pulse. Then, the perturbation from this dead-time overcorrection can be estimated as:

$$\delta I = \left(\frac{\partial I}{\partial \tau}\right)\delta\tau \tag{A.23}$$

$$= \left(\frac{I'}{1-\tau I'}\right)^2 \delta\tau = I^2\delta\tau \ . \tag{A.24}$$

We thus see that the effect of this bias is to overestimate the counting rate in a manner once again similar to the SID perturbation given by Eq. (A.13),

$$I + \delta I = I\left(1 + \delta\tau I\right) \ . \tag{A.25}$$

In fact, systematic over or under-correction in the livetime clock may lead to an observable behavior identical to the SID behavior.

LIST OF REFERENCES

LIST OF REFERENCES

[1] D.E. Alburger et al. Half-life of ^{32}Si. *Earth and Planetary Science Letters*, 78:168–176, 1986.

[2] E.D. Falkenberg. Radioactive decay caused by neutrinos? *Aperion*, 8:32–45, 2001.

[3] S.E. Schnoll et al. Realization of discrete states during fluctuations in macroscopic processes. *Physics Uspekhi*, 41:1025–1035, 1998.

[4] D.P. Veprev and V.I. Muromtsev. Evidence of solar influence on the tritium decay rate. *Astroparticle Physics*, 36(1):26 – 30, 2012.

[5] V.M Lobashev, V.N Aseev, A.I Belesev, A.I Berlev, E.V Geraskin, A.A Golubev, O.V Kazachenko, Yu.E Kuznetsov, R.P Ostroumov, L.A Rivkis, B.E Stern, N.A Titov, S.V Zadorozhny, and Yu.I Zakharov. Direct search for mass of neutrino and anomaly in the tritium beta-spectrum. *Physics Letters B*, 460(12):227 – 235, 1999.

[6] D. OKeefe, B.L. Morreale, R.H. Lee, JohnB. Buncher, J.H. Jenkins, Ephraim Fischbach, T. Gruenwald, II Javorsek, D., and P.A. Sturrock. Spectral content of 22na/44ti decay data: implications for a solar influence. *Astrophysics and Space Science*, 344(2):297–303, 2013.

[7] Jere H. Jenkins, Ephraim Fischbach, John B. Buncher, John T. Gruenwald, Dennis E. Krause, and Joshua J. Mattes. Evidence for Correlations Between Nuclear Decay Rates and Earth-Sun Distance. *Astropart. Phys.*, 32:42–46, 2009.

[8] P. A. Sturrock, J. B. Buncher, E. Fischbach, J. T. Gruenwald, D. Javorsek, II, J. H. Jenkins, R. H. Lee, J. J. Mattes, and J. R. Newport. Power Spectrum Analysis of BNL Decay-Rate Data. *Astropart. Phys.*, 34:121–127, 2010.

[9] P.A. Sturrock, E. Fischbach, and J.H. Jenkins. Further evidence suggestive of a solar influence on nuclear decay rates. *Solar Physics*, 272(1):1–10, 2011.

[10] Jere H. Jenkins, Kevin R. Herminghuysen, Thomas E. Blue, Ephraim Fischbach, Daniel Javorsek, Andrew C. Kauffman, Daniel W. Mundy, Peter A. Sturrock, and Joseph W. Talnagi. Additional experimental evidence for a solar influence on nuclear decay rates. *Astropart. Phys.*, 37:81–88, 2012.

[11] Jere H. Jenkins and Ephraim Fischbach. Perturbation of nuclear decay rates during the solar flare of 2006 december 13. *Astroparticle Physics*, 31(6):407 – 411, 2009.

[12] *Analysis of Experiments Exhibiting Time-Varying Nuclear Decay Rates: Systematic Effects or New Physics? in XLVIIth Rencontres de Moriond and GPhyS Colloquium, Gravitational Waves and Experimental Gravity.* Gioi Publishers, 2011.

[13] Kenneth J Ellis. The effective half-life of a broad beam ^{238}PuBe total body neutron irradiator. *Physics in Medicine and Biology*, 35:1079–1088, 1990.

[14] A. G. Parkhomov. Researches of alpha and beta radioactivity at long-term observations. 2010.

[15] A.G. Parkhomov. Periods detected during analysis of radioactivity measurements data. *arXiv:1012.4174 (December 2010)*, preprint.

[16] Y.A. Baurov et al. Experimental investigation of changes in β-decay count rate of radioactive elements. *Physics of Atomic Nuclei*, 70:1825–1835, 2007.

[17] H. Schrader. Half-life measurements of long-lived radionuclidesnew data analysis and systematic effects. *Applied Radiation and Isotopes*, 68(78):1583 – 1590, 2010. Proceedings of the 17th International Conference on Radionuclide Metrology and its Applications (ICRM 2009).

[18] Peter A. Sturrock, Alexander G. Parkhomov, Ephraim Fischbach, and Jere H. Jenkins. Power Spectrum Analysis of LMSU (Lomonosov Moscow State University) Nuclear Decay-Rate Data: Further Indication of r-Mode Oscillations in an Inner Solar Tachocline. *Astropart. Phys.*, 35:755–758, 2012.

[19] J. H. Jenkins, E. Fischbach, D. Javorsek II, and P. A. Sturrock. *Nucl. Instrum. Meth. A*, 74:50, 2013.

[20] Helmut Siegert, Heinrich Schrader, and Ulrich Schtzig. Half-life measurements of europium radionuclides and the long-term stability of detectors. *Applied Radiation and Isotopes*, 49(911):1397 – 1401, 1998.

[21] G. Steinitz, O. Piatibratova, and P. Kotlarsky. Possible effect of solar tides on radon signals. *Journal of Environmental Radioactivity*, 102(8):749 – 765, 2011.

[22] Peter A. Sturrock, Gideon Steinitz, Ephraim Fischbach, Daniel Javorsek, and Jere H. Jenkins. Analysis of Gamma Radiation from a Radon Source: Indications of a Solar Influence. *Astropart. Phys.*, 36:18–25, 2012.

[23] P.A. Sturrock, J.B. Buncher, E. Fischbach, J.T. Gruenwald, II Javorsek, D., J.H. Jenkins, R.H. Lee, J.J. Mattes, and J.R. Newport. Power spectrum analysis of physikalisch-technische bundesanstalt decay-rate data: Evidence for solar rotational modulation. *Solar Physics*, 267(2):251–265, 2010.

[24] T. Mohsinally, S. Fancher, M. Czerny, E. Fischbach, J.T. Gruenwald, J. Heim, J.H. Jenkins, J. Nistor, and D. OKeefe. Evidence for correlations between fluctuations in 54mn decay rates and solar storms. *Astroparticle Physics*, pages –, 2015.

[25] Abraham Pais. *Inward Bound*. Oxford University Press, 1986.

[26] Sir Edmund Whittaker. *A History of the Theories of Aether and Electricity*. Thomas Nelson and Sons Ltd, 1961.

[27] C. Ellis E. Rutherford, J. Chadwick. *Radiations from Radioactive Substances*. Cambridge University Press, 1951.

[28] E. Rutherford. A radioactive substance emitted from thorium compunds. *Philosophical Magazine*, ser. 5, xlix:1–14, 1900.

[29] Ernest Rutherford. *Radioactive Substances and Their Radiations*. Cambridge University Press, 1913.

[30] G.T. Emery. Perturbation of nuclear decay rates. *Annual Review of Nuclear Science*, 22:165–202, 1972.

[31] S.A. Moszkowski C.S. Wu. *Beta Decay*. Interscience Publishers, 1966.

[32] E. Fischbach J. Jenkins, D. Mundy. Analysis of environmental influences in nuclear half-life measurements exhibiting time-dependent decay rates. *Nucl. Instr. and Meth.*, 620:332342, 2010.

[33] A. Bussolotti et al. R. Bernabei, P. Belli. The dama/libra apparatus. *ROM2F*, 03, 2008.

[34] R. Bernabei et al. First results from dama/libra and the combined results with dama/nai. *arXiv:0804.2741v1*, 2008.

[35] R. Bernabei, P. Belli, F. Cappella, R. Cerulli, C. J. Dai, A. D'Angelo, H. L. He, A. Incicchitti, X. H. Ma, F. Montecchia, F. Nozzoli, D. Prosperi, X. D. Sheng, R. G. Wang, and Z. P. Ye. Particle Dark Matter and DAMA/LIBRA. In C. Cecchi, S. Ciprini, P. Lubrano, and G. Tosti, editors, *American Institute of Physics Conference Series*, volume 1223 of *American Institute of Physics Conference Series*, pages 50–59, March 2010.

[36] R. Bernabei et al. Particle dark matter in dama/libra. *arXiv:1007.0595v1*, 2010.

[37] R. Bernabei et al. New results from dama/libra. *arXiv:1002.1028v1*, 2010.

[38] R. Bernabei et al. No role for muons in the dama annual modulation results. *arXiv:1202.4179v2*, 2012.

[39] V. A. Kudryavtsev, M. Robinson, and N. J. C. Spooner. The expected background spectrum in NaI dark matter detectors and the DAMA result. *Astropart. Phys.*, 33:91–96, 2010.

[40] R. R. Kinsley et al. The nudat/pcnudat program for nuclear data. data extracted from the nudat database, 2.6 (02/24/12), john a. cameron and balraj singh, nuclear data sheets 102, 293 (2004)., February 2012.

[41] P. A. Sturrock, J. B. Buncher, E. Fischbach, D. Javorsek ii, J. H. Jenkins, and J. J. Mattes. Concerning the phases of the annual variations of nuclear decay rates. *The Astrophysical Journal*, 737(2):65, 2011.

[42] M.S. Thomsen, J. Heinemeier, P. Hornshj, H.L. Nielsen, and N. Rud. Half-life of 32si measured via accelerator mass spectrometry. *Nuclear Physics A*, 534(2):327 – 338, 1991.

[43] H. B. Clausen. Dating of polar ice by 32Si. *Journal of Glaciology*, 12:411–416, 1973.

[44] D. J. Demaster. The half life of ^{32}Si determined from a varved Gulf of California sediment core. *Earth and Planetary Science Letters*, 48:209–217, June 1980.

[45] J.B. Cumming. Assay of 32Si by liquid scintillation counting. *Radiochemical and Radioanalytical Letters*, 58:297–305, October 1983.

[46] W Kutschera and M Paul. Accelerator mass spectrometry in nuclear physics and astrophysics. *Annual Review of Nuclear and Particle Science*, 40(1):411–438, 1990.

[47] D. Elmore, N. Anantaraman, H. W. Fulbright, H. E. Gove, H. S. Hans, K. Nishizumi, M. T. Murrell, and M. Honda. Half-life of ^{32}Si from tandem-accelerator mass spectrometry. *Phys. Rev. Lett.*, 45:589–592, Aug 1980.

[48] Y. Chen, E. Kashy, D. Bazin, W. Benenson, D. J. Morrissey, N. A. Orr, B. M. Sherrill, J. A. Winger, B. Young, and J. Yurkon. Half-life of ^{32}Si. *Phys. Rev. C*, 47:1462–1465, Apr 1993.

[49] H.J. Hofmann, G. Bonani, M. Suter, W. Wlfli, D. Zimmermann, and H.R. von Gunten. A new determination of the half-life of 32si. *Nuclear Instruments and Methods in Physics Research Section B: Beam Interactions with Materials and Atoms*, 52(34):544 – 551, 1990.

[50] J. M. Nistor, J. M. Heim, E. Fischbach, J. H. Jenkins, and P. A. Sturrock. Phenomenology of Rate-Related Nonlinear Effects in Nuclear Spectroscopy. 2014.

[51] Jere H. Jenkins, Ephraim Fischbach, John B. Buncher, John T. Gruenwald, Dennis E. Krause, and Joshua J. Mattes. Evidence of correlations between nuclear decay rates and earthsun distance. *Astroparticle Physics*, 32(1):42 – 46, 2009.

[52] E. Fischbach, J.B. Buncher, J.T. Gruenwald, J.H. Jenkins, D.E. Krause, J.J. Mattes, and J.R. Newport. Time-dependent nuclear decay parameters: New evidence for new forces? *Space Science Reviews*, 145(3-4):285–335, 2009.

[53] R.M. Lindstrom, E. Fischbach, J.B. Buncher, G.L. Greene, J.H. Jenkins, D.E. Krause, J.J. Mattes, and A. Yue. Study of the dependence of 198au half-life on source geometry. *Nuclear Instruments and Methods in Physics Research Section A: Accelerators, Spectrometers, Detectors and Associated Equipment*, 622(1):93 – 96, 2010.

[54] Richard M. Lindstrom, Ephraim Fischbach, John B. Buncher, Jere H. Jenkins, and Andrew Yue. Absence of a self-induced decay effect in 198au. *Nuclear Instruments and Methods in Physics Research Section A: Accelerators, Spectrometers, Detectors and Associated Equipment*, 659(1):269 – 271, 2011.

VITA

VITA

Jordan Heim was born on January 11, 1984 in Evansville, IN. He received a Bachelor of Science degree in honors physics from Purdue University in May 2007 and entered their doctoral program in physics that fall. During his academic career he taught graduate and undergraduate courses extensively, as both a teaching assistant and instructor, receiving the AAPT and CETA teaching awards. He was also awarded a Purdue Research Foundation grant and received a Masters of Science degree in Physics in May 2012. He completed his Ph.D in physics at Purdue in December 2015.